

Design and dynamic analysis of soft pneumatic systems for wearable robots

Présentée le 15 octobre 2021

Faculté des sciences et techniques de l'ingénieur
Laboratoire de robotique reconfigurable
Programme doctoral en robotique, contrôle et systèmes intelligents

pour l'obtention du grade de Docteur ès Sciences

par

Sagar Dattatray JOSHI

Acceptée sur proposition du jury

Prof. A. Ijspeert, président du jury
Prof. J. Paik, directrice de thèse
Prof. K. Althoefer, rapporteur
Prof. M. Cianchetti, rapporteur
Prof. S. Sakar, rapporteur

Acknowledgements

After spending almost five years towards this degree, I fall short of words to express gratitude to all those who have changed my life. First and foremost I want to thank my supervisor, Prof. Jamie Paik for her continued support and guidance throughout this journey. I am grateful to my thesis committee, Professors Auke Ijspeert, Selman Sakar, Kaspar Althoefer and Matteo Cianchetti for evaluating my work and providing their valuable insights. Having their names on my thesis is equivalent to a degree in itself. The successful completion of any PhD involves countless administrative tasks. For handling these complicated duties, I would like to thank all the past and present administrative assistants at the Reconfigurable Robotics Lab, namely Anouk, Monica, Julia, Carole, and Joanna, as well as Corinne, our doctoral school secretary.

PhD is dark and full of terrors, and I have many people to thank for providing the light in this journey. Firstly, I want to thank each and every member of the Reconfigurable Robotics Lab: Harshal, Fred, Chris, Jian-Lin, Mete, Kevin, Fabio, Matt, Zhenishbhek, Sukho, Alice, Mohssen, Andres, Peter, and many others for being one of the most fun and caring lab that I have ever seen. Next I would like to express my heartfelt gratitude to my dear friends - Salil, Prakhar, Harshit, Anjali, Saurabh, Tejal, Mahendra, Shravan, Mohit, Pranit, Akshay, and countless others with whom I relished fun and crazy moments that I will remember for life. In difficult times, music was my moment of peace. Through music, I could be a part of many cultural events and met many people who became a part of my extended family - Sonal, Sameer, Teju, Rishikesh, Snehal, Arati, Shreyas, Megha, Navdeep, Yash, and many others. All the credit for developing my musical journey in me goes to my music gurus, Pt. Suresh Bapat, Pt. Ravi Chary, Joglekar kaka, and Yudhamanyu Gadre, for their invaluable knowledge and the kindness with which they taught me music.

Most importantly I want to thank my parents, Dattatray and Neeti Joshi, and my grandparents, Vishnu and Laxmi Chiplunkar, for believing in me, supporting me, and making me the person I am today. Lastly, I want to thank my brother, Rohit Joshi for being my pillar of support during difficult times and being the most caring brother anyone can have.

Lausanne, October 15, 2021

Sagar Joshi

Abstract

Robots have permeated many aspects of modern life, from industrial manufacturing to surgery, space exploration, and animatronics. Among these is the field of wearable robotics, with robots directly attached to the human body for assisting or augmenting a task or experience. Wearable robots can be implemented for a range of applications, including physical assistance, rehabilitation, haptics, kinaesthetic feedback, sports training, and virtual and augmented reality. Conventional robots made with rigid materials and mechanisms have limited scope in this domain due to limitations such as kinematic incompatibility with biological joints, bulky form-factors, and the lack of compliance required for safe robot-human interaction. The upcoming area of soft robotics, with unique characteristics such as material compliance, conformability, and high design versatility, could help bridge this gap. It could lead to the development of fully untethered wearable soft robotic systems that resemble any other garment and interact with the wearer. However, being a relatively recent area of research, there still remains a significant gap in the core understanding of how these new type of robots function and affect the wearer.

A critical requirement for any robot is in understanding its mechanical performance. Existing studies quantify the general mechanical performance of soft robots using experimental testing or analytical and numerical models. However, these methods fail to capture the application-specific mechanical behaviour, which changes with the environment due to the compliance and conformability of soft robots. This leads to differences between expected and observed values. Another challenge in soft robotics is the limited understanding of their dynamic behaviour, especially in the case of soft pneumatic actuators (SPAs), which are powered by pneumatic supply systems (PSSs). Although SPAs have been widely used in wearable and non-wearable applications, researchers have resorted to data-driven methods to model the dynamic response. Since the direct relationship between dynamic performance and SPA and PSS properties is not well quantified, it is currently not possible to optimize these robots to meet the requirements of performance and portability. This leads to sub-optimal performance and bulky PSSs, which directly affect the overall acceptance of wearable soft robots. In addition to their stand-alone performance in laboratory environments, a crucial element in wearable robots is to evaluate how they affect the user. While several studies report measured muscle activity or metabolic costs, it does not give the complete picture of the beneficial or detrimental effects of a given wearable robot or control strategy. This is especially important when such wearable robots exert large forces or act on sensitive locations on the body, such as the torso. A better understanding of the effectiveness of wearable robots would not only allow us to

predict their performance accurately but would also help to iterate, compare and optimize their design and control.

This thesis investigates solutions that answer some of these fundamental challenges to enable portable wearable soft robots with optimized peripheral systems for powering and controlling them. I first focussed on quantifying the application-specific mechanical behaviour of soft robots. I developed a novel characterization protocol and platform that physically recreates the environment around the soft robot and enables a systematic, repeatable, and accurate measurement of their mechanical performance. This will allow us to adapt soft robot design and control customized for the intended application. Next, I took up the challenge to understand the dynamic behaviour of SPAs. I modelled the pressure and flow dynamics of SPAs from first principles and studied the impact of several SPA and PSS properties on the SPA dynamic performance and portability. Based on this study, it is now possible to optimize PSS design and control to meet desired dynamic behaviour, portability, and other user-defined constraints. In addition, based on the improved understanding of SPA dynamics, I introduced and explored a previously unknown property of SPAs, self-sensing, which models the SPA itself as a pneumatic sensor. By monitoring its dynamic behaviour, we can now transduce information about the SPA mechanical outputs without any embedded sensors. Lastly, I developed a soft exosuit for the human torso, powered using multiple SPAs, which can be reconfigured to apply forces at different locations on the wearer. To quantify its effectiveness, I modelled the measured exosuit forces in a musculoskeletal model and calculated biomechanical quantities, including muscle forces, spinal loads, and joint moments. This enables an in-depth evaluation, comparison and optimization of soft robot design towards wearable applications. The main contributions of this thesis are:

- Systematic, repeatable and accurate characterization of soft actuator mechanical performance.
- Modelling dynamic behaviour of non-linear pneumatic actuators.
- Design, optimization and biomechanical evaluation of wearable soft robots.

This thesis unites several perspectives for investigating soft robot behaviour; to create a broader understanding of how soft robot performance can be measured, modelled, and optimized, for a user. The knowledge gained in this work applies to not only wearable robots but also other soft robotic applications such as manipulators or mobile robots and will lead to improved design and control of soft robots and their supporting systems.

Résumé

Les robots ont imprégné de nombreux aspects de la vie moderne, de la fabrication industrielle à la chirurgie, en passant par l'exploration spatiale et l'animatronique. Parmi ceux-ci se trouve le domaine de la robotique portable, avec des robots directement attachés au corps humain pour assister ou augmenter une tâche ou une expérience. Les robots portables peuvent être mis en œuvre pour une gamme d'applications, notamment l'assistance physique, la rééducation, l'haptique, le retour kinesthésique, l'entraînement sportif et la réalité virtuelle et augmentée. Les robots conventionnels fabriqués avec des matériaux et des mécanismes rigides ont une portée limitée dans ce domaine en raison de limitations telles que l'incompatibilité cinématique avec les articulations biologiques, les facteurs de forme volumineux et le manque de conformité requis pour une interaction robot-humain sûre. Le domaine à venir de la robotique douce, avec des caractéristiques uniques telles que la conformité des matériaux, la conformabilité et une grande polyvalence de conception, pourrait aider à combler cet écart. Cela pourrait conduire au développement de systèmes robotiques souples entièrement non attachés qui ressemblent à n'importe quel autre vêtement et interagissent avec le porteur. Cependant, étant un domaine de recherche relativement récent, il reste encore une lacune importante dans la compréhension fondamentale de la façon dont ces nouveaux types de robots fonctionnent et affectent le porteur.

Une exigence critique pour tout robot est de comprendre ses performances mécaniques. Les études existantes quantifient les performances mécaniques générales des robots mous à l'aide de tests expérimentaux ou de modèles analytiques et numériques. Cependant, ces méthodes ne parviennent pas à capturer le comportement mécanique spécifique à l'application, qui change avec l'environnement en raison de la conformité et de la conformabilité des robots mous. Cela conduit à des différences entre les valeurs attendues et observées. Un autre défi de la robotique douce est la compréhension limitée de leur comportement dynamique, en particulier dans le cas des actionneurs pneumatiques souples (SPA), qui sont alimentés par des systèmes d'alimentation pneumatique (PSS). Bien que les SPA aient été largement utilisés dans les applications portables et non portables, les chercheurs ont eu recours à des méthodes basées sur les données pour modéliser la réponse dynamique. La relation directe entre les performances dynamiques et les propriétés SPA et PSS n'étant pas bien quantifiée, il n'est actuellement pas possible d'optimiser ces robots pour répondre aux exigences de performances et de portabilité. Cela conduit à des performances sous-optimales et à des PSS volumineux, qui affectent directement l'acceptation globale des robots souples portables. En plus de leurs performances autonomes dans les environnements de laboratoire, un élément crucial des

robots portables est d'évaluer comment ils affectent l'utilisateur. Bien que plusieurs études rapportent une activité musculaire mesurée ou des coûts métaboliques, elles ne donnent pas une image complète des effets bénéfiques ou néfastes d'un robot portable ou d'une stratégie de contrôle donnés. Ceci est particulièrement important lorsque de tels robots portables exercent des forces importantes ou agissent sur des endroits sensibles du corps, tels que le torse. Une meilleure compréhension de l'efficacité des robots portables nous permettrait non seulement de prédire avec précision leurs performances, mais aiderait également à itérer, comparer et optimiser leur conception et leur contrôle.

Cette thèse étudie des solutions qui répondent à certains de ces défis fondamentaux pour permettre aux robots souples portables avec des systèmes périphériques optimisés pour les alimenter et les contrôler. Je me suis d'abord concentré sur la quantification du comportement mécanique spécifique à l'application des robots mous. J'ai développé un nouveau protocole et une plate-forme de caractérisation qui recrée physiquement l'environnement autour du robot mou et permet une mesure systématique, reproductible et précise de ses performances mécaniques. Cela nous permettra d'adapter la conception et le contrôle du robot souple à l'application prévue. Ensuite, j'ai relevé le défi de comprendre le comportement dynamique des SPAs. J'ai modélisé la dynamique de pression et d'écoulement des SPA à partir des premiers principes et étudié l'impact de plusieurs propriétés de SPA et PSS sur les performances dynamiques et la portabilité du SPA. Sur la base de cette étude, il est désormais possible d'optimiser la conception et le contrôle du PSS pour répondre au comportement dynamique souhaité, à la portabilité et à d'autres contraintes définies par l'utilisateur. De plus, sur la base d'une meilleure compréhension de la dynamique du SPA, j'ai introduit et exploré une propriété jusqu'alors inconnue des SPA, l'auto-détection, qui modélise le SPA lui-même comme un capteur pneumatique. En surveillant son comportement dynamique, nous pouvons maintenant transduire des informations sur les sorties mécaniques du SPA sans aucun capteur intégré. Enfin, j'ai développé une exosquelette souple pour le torse humain, alimentée à l'aide de plusieurs SPA, qui peut être reconfigurée pour appliquer des forces à différents endroits sur le porteur. Pour quantifier son efficacité, j'ai modélisé les forces de l'exosquelette mesurées dans un modèle musculo-squelettique et calculé les quantités biomécaniques, y compris les forces musculaires, les charges vertébrales et les moments articulaires. Cela permet une évaluation, une comparaison et une optimisation approfondies de la conception de robots souples vers des applications portables. Les principaux apports de cette thèse sont :

- Caractérisation systématique, reproductible et précise des performances mécaniques des actionneurs souples.
- Modélisation du comportement dynamique d'actionneurs pneumatiques non linéaires.
- Conception, optimisation et évaluation biomécanique de robots portables souples.

Cette thèse réunit plusieurs perspectives pour étudier le comportement des robots mous; pour créer une compréhension plus large de la façon dont les performances des robots logiciels peuvent être mesurées, modélisées, optimisées et quantifiées sur un utilisateur. Les connaissances acquises dans ce travail s'appliquent non seulement aux robots portables,

mais également à d'autres applications robotiques souples telles que les manipulateurs ou les robots mobiles et conduiront à une conception et un contrôle améliorés des robots souples et de leurs systèmes de support.

Contents

Acknowledgements	i
Abstract (English/Français)	iii
Introduction	1
1 Multi-DoF characterization of soft actuators	13
1.1 Introduction	13
1.2 Interaction forces of soft actuators	15
1.3 Experimental setup and protocol	16
1.3.1 Experimental setup	16
1.3.2 Pulling force	18
1.3.3 Tip loading	19
1.3.4 Symmetric three-point bending	21
1.4 Results and discussion	23
1.4.1 Pulling force	23
1.4.2 Tip loading	23
1.4.3 Three-point bending	25
1.5 Characterization of a meso-scale fingertip haptic device	26
1.5.1 <i>Haptigami</i> : the origami-inspired fingertip haptic device	27
1.5.2 Experimental setup and protocol	28
1.5.3 Results	30
1.6 Discussion	31
2 Modelling and parametric study of pneumatic supply systems	33
2.1 Introduction	33
2.2 Modelling pressure and flow dynamics	35
2.2.1 Modelling pressure dynamics of PSSs	36
2.2.2 Modelling soft actuator pressure dynamics	38
2.2.3 Normalization	38
2.3 Simulation study	39
2.3.1 Methods	40
2.3.2 Results	41
2.3.3 Validation	45

Contents

2.4	Practical considerations in PSS modelling and design	46
2.4.1	Defining parameter range and simulating pressure dynamics	47
2.4.2	Experimental testing	49
2.4.3	Results	50
2.5	Discussion	53
3	Implementation towards PSS optimization	55
3.1	Introduction	55
3.2	Defining the optimization problem	57
3.3	Simulation study	58
3.4	Implementation to PSS design	59
3.4.1	Design requirements	60
3.4.2	Comparison with experimental testing	62
3.5	Discussion	63
4	Sensorless force and displacement estimation in soft pneumatic actuators	65
4.1	Introduction	65
4.2	Defining pneumatic inputs and mechanical outputs for sensorless estimation .	68
4.2.1	Modelling pressure and flow dynamics	68
4.2.2	Defining SPA force and displacement	69
4.3	Experimental characterization of SPA-pack	70
4.3.1	Experimental setup	70
4.3.2	Experimental protocol and data collection	71
4.4	Neural network design, training and validation	73
4.4.1	Defining input features and neural net architectures	74
4.4.2	Training the neural networks	75
4.5	Results and discussion	76
4.5.1	Effect of estimation strategy	76
4.5.2	Effect of number of hidden neurons	77
4.5.3	Effect of loading conditions	78
4.6	Discussion	79
5	Design and biomechanical analysis of soft exosuit for the human torso	81
5.1	Introduction	81
5.2	Design and evaluation strategies for soft reconfigurable exosuit	83
5.2.1	Soft exosuit design	83
5.2.2	Evaluation methods	89
5.3	Biomechanical modelling of the exosuit	90
5.3.1	Torso musculoskeletal model	90
5.3.2	Exosuit model	90
5.4	Testing the exosuit in forward bending support	92
5.4.1	Experimental protocol	92
5.4.2	Modelling forces in OpenSim	93

5.5 Results	94
5.6 Discussion	96
6 Conclusions and future outlook	101
6.1 Conclusions	101
6.2 Current limitations of the thesis and future research directions	103
6.3 Broad impact	105
Appendices	107
A1 Kinematics of the Haptigami	107
A2 Modelling pressure dynamics of PSS	110
A3 Modelling soft actuator pressure dynamics	112
A4 Defining valve duty cycle	114
A5 Expressions for air and energy consumed	115
A6 Validating PSS simulation results via testing with pneunet	116
A7 Selected components for optimal PSS design	117
A8 Calculating ground-truth values for displacement in Three-point bending . . .	118
A9 Characterization of pouch-type SPAs and contact pressure sensor	120
 Bibliography	 121
Curriculum Vitae	137

Introduction

The word "robots" makes us think of marvels of engineering that combine motors, sensors, electronics, and computers to form precise, fast, and powerful machines capable of performing arduous tasks. Robots are being used for nearly everything under the sun, including manufacturing, transport, surgery, space exploration, and even cyborgs that look and behave like humans. One such area is wearable robotics, where a robot is directly attached to a human in order to assist or augment the human body. Wearable robots have been implemented for numerous applications such as assistance in activities of daily living, rehabilitation, haptics, sports training, and virtual and augmented reality.

Based on their structural design, these robots can be categorized as rigid exoskeletons and soft exosuits [165]. Rigid exoskeletons (Fig. 1A-D) have well defined motions supported on a robust load-bearing structure, high power capacity, and they benefit from the extensive knowledge base from conventional robotics. However, the rotational joints of these devices do not align

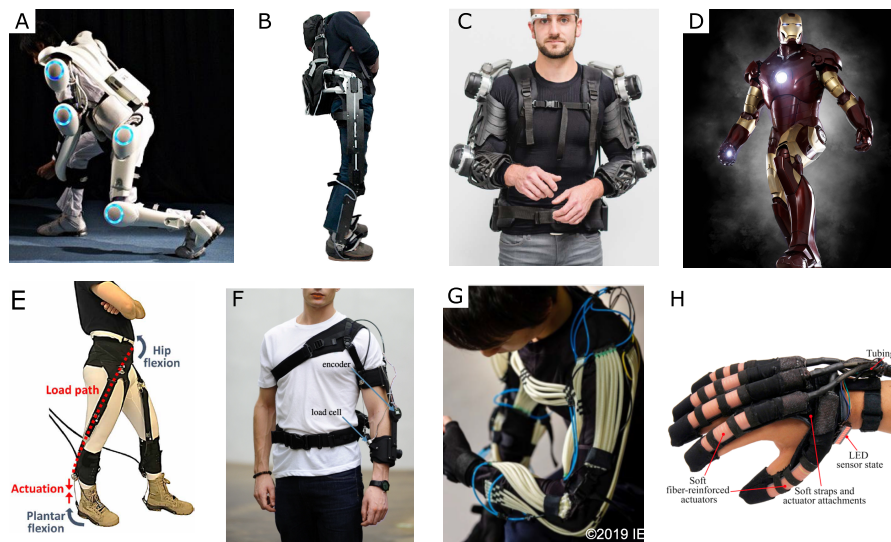


Figure 1: State of the art in wearable robots: (A) Hybrid-assistive-limb for full body assistance [1], (B) TWICE exoskeleton for assisting patients with spinal-cord injuries [2], (C) Stuttgart exo-jacket for upper limb support [3] (D) IronMan, a fictional high-tech prosthesis, (E) Soft exosuit for gait assistance [4], (F) Soft exosuit for elbow assistance [5], (G) Soft exosuit for arm support using thin soft pneumatic actuators [6], (H) Soft robotic glove for hand assistance [7].

Introduction

well with the biological joints causing kinematic incompatibility, which can lead to increased interaction forces, discomfort, and even pain. Some devices incorporate additional linkages and mechanisms to address kinematic incompatibility, but this increases design complexity and hinders practical implementation [8]. Furthermore, such rigid wearable robots tend to be bulky and heavy, which affects their user acceptance.

Soft exosuits (Fig. 1E-H) are functional garments that attach to and apply forces on the body, while using the wearer's body for structural support [165]. They fall under the umbrella of soft robotics, which consist of devices made with compliant materials such as fabric, silicone, and soft plastics [18; 19]. With their unique mechanical properties such as compliance, durability, hyperelasticity, low weight, and ease of fabrication, soft robots have gained increasing attention in wearable and non-wearable applications alike. Soft robots are especially attractive for wearable applications because their compliance enables them to conform to their contact surfaces, adapt to misalignments, and apply well-distributed forces. The compliance of these robots can be achieved through different approaches such as use of soft hyperelastic materials, flexibility through materials or design, or hyper-redundant kinematics [19]. Similarly, actuation can be achieved through bowden cables, fluidic power, or electric charge [19]. Among these different actuation mechanisms in soft robots, pneumatically powered **soft pneumatic actuators (SPAs)**, depicted in Fig. 2A, are widely used because of their high force capacity, limitless customizability, and capability to produce complex motions using the relatively simple input of pressure control [18]. Other than the soft materials of these actuators, the compressibility of air adds to the overall compliance making the device back-drivable and

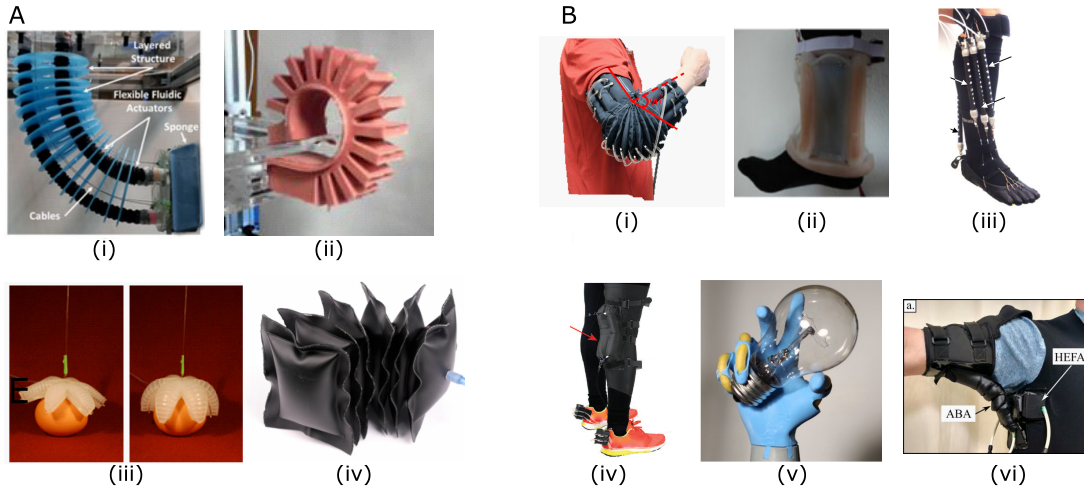


Figure 2: State of the art technologies in soft pneumatic actuators: **Soft pneumatic actuators or SPAs** present an attractive choice in robotics due to their compliance, conformability, and design versatility. Their soft material properties coupled with the compressibility of air make them especially useful for wearable robots. (A) State of the art SPAs: (i) A modular 3 DoF SPA [9], (ii) High speed pneumatic actuator [10], (iii) SPA gripper manipulating delicate objects, (iv) Pouch-type bending SPA [11], (B) Wearable robots using SPAs: (i) Soft exosuit for elbow assistance [12], (ii) Variable stiffness module for ankle support [13], (iii) Soft orthosis for ankle support [16], (iv) Exosuit for knee support [15], (v) Soft prosthetic hand [17], (vi) Exosuit for shoulder assistance [14].

inherently safe for human interaction. Fig. 1G-H and Fig. 2B show some state of the art exosuits made using SPAs for assisting the hand [17; 20; 7], ankle [16], knee [15], elbow [12], hip [21; 22; 13], and shoulder [1; 14]. Despite these advantages, there are many challenges in the development of this class of robots due to the non-linearities of the materials used, non-linear pneumatic flow, complex non-standard designs, and high compliance that leads to loading-specific mechanical behaviour. As a result, there is still a significant gap towards understanding these robots, as compared to standard well-known actuators such as motors, rigid pneumatic actuators, or voice-coils.

Some fundamental challenges in soft and wearable robots

The inherent compliance of SPAs imparts them with virtually infinite degrees of freedom (DoF) of motion, and challenges accurate prediction of their mechanical outputs, i.e. displacement and interaction forces. Therefore, an SPA used in different applications will not have the same force and displacement characteristics. While existing studies have used experimental, analytical, and numerical methods for quantifying SPA mechanical behaviour, they have not taken into account the application-specific loading conditions that govern the mechanical behaviour. This leads to discrepancies between expected and observed values and limit our understanding of these actuators. This challenge is not limited to SPAs alone, and is characteristic to soft material robots in general.

Another significant challenge is in our limited understanding of SPA dynamic behaviour. While there are numerous studies on soft actuator kinematics, deformation and force interactions using analytical modelling [24; 25; 26; 27], rigid-kinematic approximations [28; 29; 30], or FEA [31; 32], the SPA dynamic response is relatively less explored. SPAs are powered and controlled by **pneumatic supply systems (PSSs)** consisting of components such as compressors, valves, tubing and reservoirs. Regardless of the choice of actuator, the PSS critically affects overall performance of soft robots because it governs the SPA pressure dynamics and thereby, the general dynamic behaviour. Previous studies, however, have not investigated the effects of PSSs on SPAs, and instead have relied on data-driven methods to model the dynamic response. The relation between various PSS components and their properties on the SPA dynamic behaviour is therefore unknown, and it is difficult to predict how a given combination of SPA and PSS will perform. This knowledge gap hinders the modelling and control of SPAs as well as the design of PSSs, forcing researchers to resort to heuristic design approaches. In addition to meeting desired performance, soft robots have other requirements in terms of size, weight, and portability. Current methods of PSS design are insufficient to address these multiple objectives and lead to bulky sub-optimal PSS designs which affect dynamic performance, wearability, and portability of SPA-powered robots.

Lastly, beyond the actuation capabilities, an important aspect of wearable robots is their effect on the wearer. As opposed to rigid exoskeletons, which have solid frames to bear some of the forces produced, soft exosuits use the wearer's body as the structure to transfer loads. This can

potentially lead to high forces on the skin or across the wearer's joints. Understanding these effects is critical especially when the device applies large forces or acts on sensitive locations such as the spine. Wearable robots can be evaluated via subjective user surveys, measurement of biomechanical quantities such as muscle activity, and biomechanical predictions via device-human models. All three methods validate and complement each other to give an in-depth understanding of how the device affects its user. While the first two evaluation methods have been implemented for soft wearable robots, developing device-human models is challenging because soft robots conform to the body and apply well-distributed loads on large surfaces. Thus, despite the development of several wearable soft robots, existing evaluation methods are unable to comprehensively assess the biomechanical effect.

Combined together, the above challenges represent significant gaps in our core knowledge and understanding of how SPAs and soft robots, in general, function and affect the wearer. These limitations affect the design and implementation of soft robots not only in wearable devices, but also in other applications such as mobile robots or manipulators.

Problem statement

The limitations in our current knowledge of soft robots restrict their implementation in both wearable and non-wearable applications. These limitations include the core understanding of the mechanical output of soft actuators, dynamic response of pneumatically powered SPAs, and the biomechanical effect of soft wearable robots. This thesis aims to fill this gap by formulating three research questions as follows:

1. *How can we quantify mechanical performance of soft robots in a consistent, repeatable, and accurate way?*

The SPA mechanical behaviour is governed by soft robot design properties such as materials and geometry, its actuation input, as well as the interactions with the surroundings. This research question aims to develop an effective approach to investigate the effect of these parameters and create a better understanding of the application-specific mechanical outputs of soft robots.

2. *How do pneumatic systems and loading conditions affect the dynamic behaviour of soft actuators?*

PSSs strongly govern the SPA dynamic behaviour as they generate and control the pressurized air. In addition, SPA properties such as design geometry and materials, as well as the SPA interactions with its surroundings influence the dynamics. This research question aims to create a deeper understanding of these dependencies and quantify their effect on the SPA dynamic performance.

3. *How can we evaluate the effect of wearable soft robots on the biomechanics of the user?*

As soft wearable robots use the wearer's body for bearing loads, it is critical to accurately

Contributions towards the development of soft robotic technologies

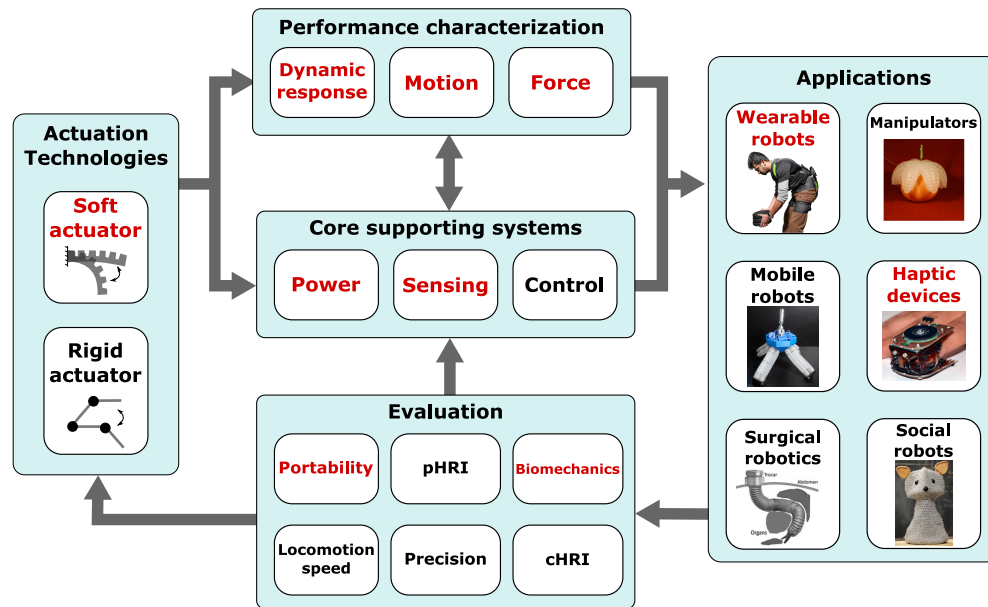


Figure 3: Contributions of this thesis towards the development of robotic technologies: The broad scope of this work spans across different aspects depicted in the blocks related to actuation technologies, core supporting systems, performance characterization, applications and evaluation. The text highlighted in red represent the different aspects directly addressed in the course of this thesis, while the remaining represent additional work that can be addressed in future studies. By investigating and consolidating these different areas of research, this thesis creates a broad system-wide understanding that would facilitate the next generation of optimized soft robots in both wearable and non-wearable applications.

investigate how they affect the wearer. This research question aims to develop evaluation methods to better understand the biomechanical effect of wearable soft robots.

Through these research questions, this thesis addresses important challenges in soft and wearable robots in order to bridge the gaps in our understanding. Fig. 3 depicts the broad scope of this thesis in the field of soft robots. The text highlighted in red corresponds to the different research areas directly addressed in the course of this thesis, while the remaining represent other facets of the corresponding blocks for the *Actuation technologies*, *Core supporting systems*, *Performance characterization*, *Applications* and *Evaluation*. Although this thesis focuses on wearable robots, we develop fundamental understanding that is applicable to other applications such as manipulators or mobile robots. The different aspects addressed in the course of this thesis include design optimization, biomechanics, pneumatic systems, and mechanical performance characterization. By investigating and consolidating these different fields of research, this thesis creates a system-wide understanding of soft technologies that would facilitate the next generation of robots for wearable as well as non-wearable applications.

Thesis structure and contributions

This thesis aims to develop a comprehensive system-wide understanding of soft wearable robots through investigation and quantification of their soft actuator mechanical outputs, dynamic performance, and biomechanical effects. Towards this goal, we explore methods for accurate and consistent experimental characterization, modelling of SPA pressure and flow dynamics, and musculoskeletal modelling and analysis of soft wearable robots. First, we present a novel experimental protocol and setup for recreating application-specific loading conditions, in order to accurately capture the mechanical behaviour of soft robots. This concept is based on emulating the physical constraints acting on the soft robot at its contact points, and measuring the mechanical outputs. Then, we analyse the pressure dynamics of SPAs and its dependency on the PSS and loading conditions. Via simulations and experimental testing, we map a direct relationship between properties of the PSS and SPA, and dynamic performance metrics. Using these relations, we present design optimization of PSSs for simultaneously meeting requirements of performance, portability and additional user-defined metrics such as mass or volume. By further investigating the effect of loading conditions on SPA pressure dynamics, we introduce a previously unknown property of SPAs, self-sensing, that allows estimation of force and displacement without dedicated sensors. Finally, we investigate the biomechanical effect of soft wearable devices via the design and modelling of a soft exosuit for the human torso. The research in this thesis can be broadly categorized into three sections: quantifying mechanical behaviour of soft robots, modelling pressure dynamics of soft pneumatic actuators, and evaluating biomechanical effect of soft exosuits, as shown in Fig. 4. We address these different research areas in six chapters as described below:

Chapter 1: Multi-DoF characterization of soft actuators

Soft actuators provide highly adaptable actuator options for applications in wearable devices, grippers and mobile robots due to their inherent compliance. However, this compliance causes soft actuators to have virtually infinite degrees of freedom (DoF) of motion, and challenges accurate prediction of their displacement and interaction forces. While several studies have characterized soft actuators either in blocked condition or in a specific range of motion, the testing conditions often do not match actual loading conditions, which leads to discrepancies between expected and observed mechanical behaviour. In this chapter, we propose a novel multi-DoF experimental protocol for characterizing soft actuator interaction forces by considering three critical aspects: *anchoring conditions*, *displacement boundary conditions* and *actuation power*. In order to conduct this multi-DoF characterization, we designed a novel reconfigurable robotic test platform for enforcing *anchoring conditions* and planar *displacement boundary conditions*, and measuring forces at multiple contact locations. We demonstrate our experimental protocol by testing a bending actuator in three loading conditions: pulling force, tip loading and three-point bending. Our results show that the three loading conditions produce distinct mechanical behaviours, thereby validating the importance of loading conditions on soft actuator performance. Lastly, we demonstrate

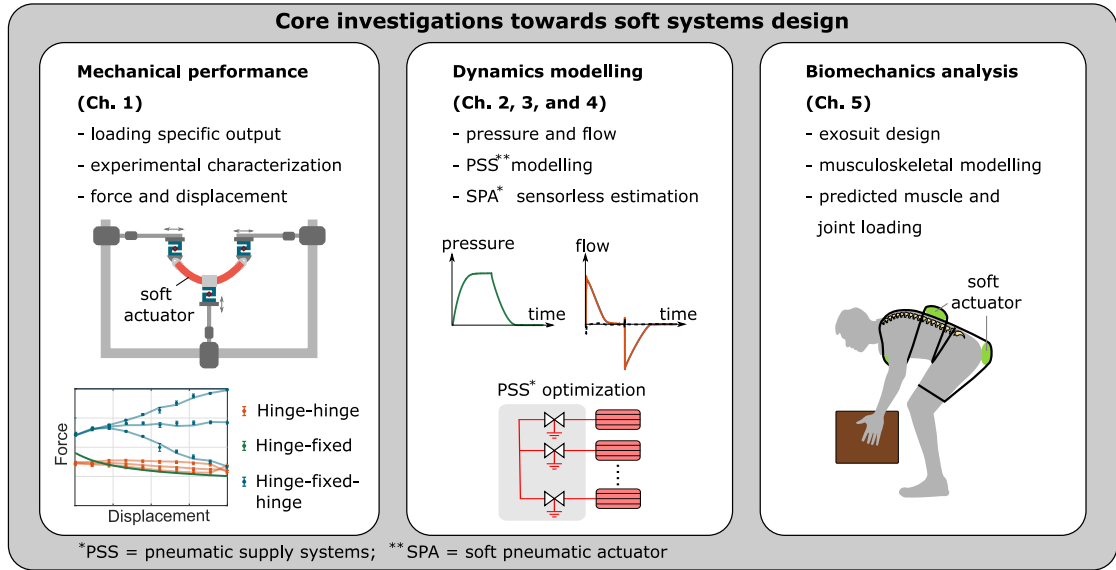


Figure 4: Core investigations conducted in this thesis towards soft systems design: This thesis can be broadly divided into three parts related to: mechanical performance characterization, dynamics modelling, and analysis of wearable robots on biomechanics of the user. In Chapter 1, we present a method to quantify loading-specific mechanical output of soft robots. In Chapters 2, 3, and 4, we model the effect of PSS, SPA and loading conditions on the SPA dynamic response. Lastly, in Chapter 5, we present the design and biomechanical analysis of a soft exosuit for supporting the torso.

another example of the proposed experimental protocol via the characterization of a meso-scale fingertip haptic device. Our protocol helps to quantify the mechanical outputs of the device in its three actuation modes and complete range of motion. This leads to a significant improvement over studies with existing fingertip haptic devices that only conduct user surveys, or characterize in a limited range of motion. The main contributions of this chapter are:

- A novel multi-DoF experimental protocol for examining and characterizing soft actuators, based on physically simulating *anchoring conditions*, *displacement boundary conditions*, and *actuation power*.
- Design of a novel robotic platform for force and displacement characterization of soft actuators at multiple contact points.
- Validation of effectiveness of the experimental protocol and the platform by testing a bending soft actuator in three distinct loading conditions, and a meso-scale haptic device in three actuation modes.

The material presented in this chapter has been adapted from the following publications:
 [36] **Joshi, S., & Paik, J.** (2019). Multi-DoF force characterization of soft actuators. *IEEE Robotics and Automation Letters*, 4(4), 3679-3686. DOI: 10.1109/LRA.2019.2927936.

[61] Giraud F, **Joshi S.** and Paik J. (2021). Haptigami: A fingertip haptic interface with vibrotactile and 3-DoF cutaneous force feedback. IEEE Transactions on Haptics (Early access). DOI: 10.1109/TOH.2021.3104216

Chapter 2: Modelling and parametric study of pneumatic supply systems for SPA dynamic performance

SPAs are powered and controlled by pneumatic supply systems (PSSs) consisting of components such as compressors, valves, tubing and reservoirs. Regardless of the choice of actuator, the PSS critically affects overall performance of soft robots because it governs the soft actuator pressure dynamics and thereby, the general dynamic behaviour. Currently, there is no comprehensive understanding on how PSS components affect the SPA dynamic behaviour due to limited understanding of soft actuator pressure dynamics, large solution space for PSSs, and variability in soft actuators. This represents a significant knowledge gap in our understanding of SPAs, and challenges customized design of PSSs to meet desired performance specifications. In this chapter, we address these limitations by modelling the SPA pressure dynamics and analysing the effect of over twelve model parameters on the SPA dynamic performance in no-load conditions. These parameters include properties and control values of PSS components such as source pressure, source flow capacity, valve flow capacity, and tubing size, as well as SPA properties such as internal volume and operating pressure. We first carry out a simulation study to create a mapping between these parameters, followed by extensive experimental validation in over 168 parameter combinations. While doing so, we address practical considerations such as valve delay compensation and characterizing flow through components. The results highlight interesting trends of how different components and their properties affect the dynamic performance, as well as the physical limits of performance achievable by a given combination of PSS and SPA. The main contributions of this chapter are:

- A pressure dynamics model considering over twelve critical parameters of pneumatic supply systems and soft pneumatic actuators.
- Simulation study to investigate the impact of PSS parameters and soft actuator design parameters on SPA dynamic performance in terms of rise time, fall time and maximum actuation frequency.
- Exhaustive experimental characterization to investigate the effect of five critical parameters, *SPA size*, *tubing length*, *tubing diameter*, *source pressure*, and *valve flow capacity*, on actuation frequency.

The material presented in this chapter has been adapted from the following publications:

[76] **Joshi, S.,** & Paik, J. (2021). Pneumatic supply system parameter optimization for soft actuators. Soft Robotics, 8(2), 152-163. DOI: 10.1089/soro.2019.0134.

[77] **Joshi, S.**, Sonar H. & Paik, J. (2021). Flow path optimization for soft pneumatic actuators - Towards optimal performance and portability. *IEEE Robotics and Automation Letters*. IEEE Robotics and Automation Letters, 6(4), 7949-7956. DOI: 10.1109/LRA.2021.3100626.

Chapter 3: Implementation towards PSS optimization

Although their functionality is well-known, the direct relationship between PSS and SPA dynamic behaviour was not well-quantified until recently. By using the results from the previous chapter, it would be possible to tailor the design, selection, and control of PSS components to meet the desired SPA dynamic performance. In addition to performance however, there are many other requirements for PSS design such as its mass, volume and duration of operation that must also be considered. These different specifications have conflicting requirements such that a PSS providing high performance and portability leads to a bulkier design, which is generally undesirable. In this chapter, we address this challenge and present the design optimization of PSSs towards simultaneously meeting the requirements of performance, portability, and user-defined constraints such as mass and size. After formulating the optimization problem, we demonstrate this approach using two examples. First, we investigate the optimal selection of valve, tubing diameter and source pressure to meet the desired actuation frequency, while minimizing the air and energy consumption during actuation. In the second example, we optimize the selection and control of PSS components to meet desired performance metrics for a wearable and portable exosuit, while minimizing mass of selected components. The measured pressure response with this prototype agrees well with simulations, with root mean square errors under 5.2%. By enabling PSS design optimization, this work aims to further the scope of soft robotics. The main contributions of this chapter are:

- PSS design optimization via selection and control of PSS components towards metrics of SPA dynamic performance, portability, and user-defined specifications such as mass and size.
- Validation of PSS optimization via design and testing of wearable PSS for soft exosuit

The material presented in this chapter has been adapted from the following publications:

[76] **Joshi, S.**, & Paik, J. (2021). Pneumatic supply system parameter optimization for soft actuators. *Soft Robotics*, 8(2), 152-163. DOI: 10.1089/soro.2019.0134.

[77] **Joshi, S.**, Sonar H. & Paik, J. (2021). Flow path optimization for soft pneumatic actuators - Towards optimal performance and portability. *IEEE Robotics and Automation Letters*. IEEE Robotics and Automation Letters, 6(4), 7949-7956. DOI: 10.1109/LRA.2021.3100626.

Chapter 4: Sensorless force and displacement estimation in soft pneumatic actuators

The non-linear mechanical behaviour of soft pneumatic actuators (SPAs), often coupled with strong dependence on loading conditions necessitates sensing and feedback control. Despite advances in dedicated force and displacement sensors, sensing in SPAs is an active area of research and faces challenges such as difficult manufacturing processes, weak actuator-sensor interfaces, hysteresis and drift. In this chapter, we introduce a novel method that entirely eliminates the need for dedicated displacement and force sensors by modelling the SPA itself as a sensor. The main principle here is that the SPA pressure, flow, volume and air mass change while interacting with the environment, which when monitored using readily available pressure sensors, can be used to reconstruct the force and displacement. After modelling the pressure and flow dynamics, we test a bending SPA in a wide range of anchoring conditions, displacement and actuation sequences to ensure the robustness of this method to loading conditions. Using the measured data, we train a time-delay neural network to model the non-linear and time dependent relation between pneumatic quantities and the SPA output force and displacement. Using only pressure measurements as input, the neural nets showed errors under 10% and 20% for force and displacement estimation respectively, even with previously unseen test conditions. Although an embedded flex sensor in the SPA showed higher estimation accuracy than sensorless estimation, combining the two via sensor fusion showed highest accuracy due to sensing redundancy. By modelling the actuator as a pneumatic sensor, the proposed method is a first step towards self-sensing in SPAs and pneumatic systems in general. The main contributions of this chapter are:

- A novel sensing concept to simultaneously predict pneumatic actuator force and displacement without dedicated sensors
- A new experimental protocol for characterizing soft sensors for improved robustness to loading conditions, by controlling anchoring conditions, displacement, and actuation sequences
- A comparative analysis of the estimation accuracy of the sensing methods (sensorless vs. flex sensor vs. sensor fusion), the loading conditions, and the number of neurons using time-delay neural nets.

The material presented in this chapter has been adapted from the following publications:

Joshi, S. & Paik, J. (2021). Sensorless force and displacement estimation in soft pneumatic actuators. IEEE/ASME Transactions on Mechatronics (under review).

Chapter 5: Design and biomechanical analysis of soft exosuit for the human torso

Wearable torso assistive devices are a potential solution to work-related musculoskeletal disorders in physically demanding professions such as construction or industrial assembly

lines. Previous studies with such devices have reported reduced metabolic costs and measured excitation of the superficial torso muscles. However, the effect of assistive devices on other metrics such as loading on the deeper torso muscles or distribution of compressive and shear forces throughout the spine is yet to be determined. This becomes even more critical for soft exosuits that use the wearer's body for bearing the generated forces and therefore could lead to increased loading on the spine. In this chapter, we present the design, in-depth biomechanical modelling, and analysis of a reconfigurable soft exosuit for the human torso. The exosuit consists of pouch-type soft pneumatic actuators (SPAs) and overlapping fabric straps that can be configured for forward, lateral or posture assistance. We test the exosuit in static forward bending at seven angles with two subjects and measure the SPA forces. We resolve the SPA forces into tension in different sections of the exosuit and apply these forces on a musculoskeletal model of the torso. Using this exosuit-torso model, we quantify how the exosuit affects torso muscles and loading on the thoracic and lumbar spine in terms of compressive and shear forces, and joint moment. Results predict similar or higher reduction in lumbo-sacral joint moment and muscle activity of the main back extensor, compared to previous studies. At the same time they also show for the first time that, loading on the torso muscles and spine gets redistributed while using the exosuit. This work enables an in-depth understanding of the biomechanical effect of torso assistive devices and can be implemented for their design iteration, validation, control and comparison. The main contributions of this chapter are:

- A novel reconfigurable soft exosuit for torso assistance.
- A biomechanical model for fabric-based exosuits considering musculoskeletal structure of the torso and tension forces in the exosuit webbing.
- Testing and in-depth biomechanical evaluation of the soft exosuit with two subjects via predicted muscle and spinal loading.

Chapter 6: Conclusions and future outlook

In the concluding part of this thesis, we summarize the methods and results of the previous three parts. We also inspect whether the research questions posed in the beginning were satisfactorily answered, what is the scope where the presented methods will or will not work, and what efforts can be undertaken in the future for building up on the presented findings. As depicted in Fig. 3, the models, methods, and results of this thesis are applicable to soft robots, wearable robots, and pneumatic systems in general, and would aid in the development of the next generation of improved, more impactful robotic technologies.

The supplementary videos for this thesis have been uploaded to the following YouTube playlist: [Supplementary videos](#).

List of publications

The research undertaken in this thesis led to the following published and unpublished works:

1. **Joshi, S.,** & Paik, J. (2019). Multi-DoF force characterization of soft actuators. IEEE Robotics and Automation Letters, 4(4), 3679-3686. DOI: 10.1109/LRA.2019.2927936 [36].
2. Giraud F, **Joshi S.** and Paik J. (2021). Haptigami: A fingertip haptic interface with vibrotactile and 3-DoF cutaneous force feedback. IEEE Transactions on Haptics (Early access). DOI: 10.1109/TOH.2021.3104216 [61].
3. **Joshi, S.,** & Paik, J. (2021). Pneumatic supply system parameter optimization for soft actuators. Soft Robotics, 8(2), 152-163. DOI: 10.1089/soro.2019.0134 [76].
4. **Joshi, S.,** Sonar H. & Paik, J. (2021). Flow path optimization for soft pneumatic actuators - Towards optimal performance and portability. IEEE Robotics and Automation Letters. IEEE Robotics and Automation Letters, 6(4), 7949-7956. DOI: 10.1109/LRA.2021.3100626 [77].
5. Song, S., **Joshi, S.,** & Paik, J. (2021) "CMOS-Inspired Complementary Fluidic Circuits for Soft Robots." Advanced Science: 2100924. DOI: 10.1002/adv.202100924 [175].
6. **Joshi, S.** & Paik, J. (2021). Sensorless force and displacement estimation in soft pneumatic actuators. IEEE/ASME Transactions on Mechatronics (**under review**).

1 Multi-DoF characterization of soft actuators

The inherent compliance of soft actuators allows them to adapt to their surroundings and perform complex motions and tasks using relatively simple inputs. These properties also make them especially attractive for wearable robots, because they can conform to the user's body and apply well-distributed forces, without constraining the natural range of motion of the user. At the same time, however, this implies a strong dependency on the loading conditions, which makes it difficult to accurately quantify the mechanical behaviour of soft actuators. This problem is a characteristic of soft actuators and soft robots in general, and therefore also observed in non-wearable applications such as mobile robots or manipulators. In this chapter, we tackle this challenge via a novel experimental protocol to consistently and accurately characterize the mechanical output of soft robots and soft actuators. We demonstrate this approach by testing a bending soft actuator in three loading conditions, and a fingertip haptic device in three actuation modes.

1.1 Introduction

Soft actuators present unique solutions in robotics because of characteristics such as compliance, conformability and versatility [19; 18; 37]. They are being used increasingly in applications including wearable devices [18; 16; 38; 39; 40; 22; 20; 41], locomotion [42; 43; 44; 45; 26; 46] and grasping [47; 48; 49]. The overall performance of these actuators is defined by their mechanical behaviour while interacting with their environments. For instance, actuator displacement along with magnitude and direction of interaction forces governs the grasping

The material presented in this chapter has been adapted from the following publications:

[36] **Joshi, S.**, & Paik, J. (2019). Multi-DoF force characterization of soft actuators. *IEEE Robotics and Automation Letters*, 4(4), 3679-3686. DOI: 10.1109/LRA.2019.2927936

[61] Giraud F, **Joshi S.** and Paik J. (2021). Haptigami: A fingertip haptic interface with vibrotactile and 3-DoF cutaneous force feedback. *IEEE Transactions on Haptics* (Early access). DOI: 10.1109/TOH.2021.3104216

F. Giraud designed and fabricated the *Haptigami*, derived kinematics models, conducted experiments, wrote the manuscript, and developed the initial concept and direction of experiments and scientific objectives. S. Joshi designed the characterization platform, custom script for running the hardware, and contributed to the manuscript writing. J. Paik supervised the research objectives of the work.

ability for a gripper [48] or the step length for a walking robot [42]. Similarly for a wearable robot, the distribution of forces at the contact locations impacts overall effectiveness. In order to further the scope of soft robotics, an understanding of soft actuator mechanical behaviour is necessary.

There are numerous studies investigating soft actuator displacement and interaction forces using analytical [26; 27; 28; 24; 50; 25; 29; 30], numerical [31; 18; 51; 32] or experimental methods [16; 38; 10; 45; 26; 39; 52; 53; 54; 40]. One study uses a quasi-static analytical model to predict tip force interactions of fibre reinforced soft pneumatic actuators (SPAs) in bending [55]. Trivedi et al. have used Cosserat rod theory to model the planar force and displacement of a 9 degree of freedom (DoF) soft pneumatic manipulator [24]. Another recent study uses equivalent rigid-body dynamics to model dynamic motion and force interactions of a SPA [30]. While these models are able to predict the displacement and interaction forces, they are limited to the specific actuators with simple conditions such as tip loading or assumptions such as constant curvatures. It is difficult to apply these models for non-standard actuator designs and loading conditions. A different approach to studying and predicting interaction forces uses finite elemental method (FEM). An open source physics simulator, Simulation Open Framework Architecture (SOFA), uses FEM for real-time modelling and control of soft deformable robots [51; 31]. Another tool, the SPA-tool kit, uses FEM to optimize SPA design parameters for meeting specifications of desired force and displacement [32]. Many other studies use FEM to predict free displacement and force output of soft actuators [18; 55]. While such numerical methods can address a larger range of actuator designs and loading conditions, in practice, aspects such as friction, hysteresis, manufacturing inconsistencies and boundary conditions uncertainty affect the accuracy and applicability of these methods. Therefore, several studies resort to experimental characterization as it is a direct measurement of the interaction forces [16; 38; 10; 45; 26; 39; 52; 53; 54; 40]. Moreover, experimental testing is necessary for validating results from analytical or numerical methods.

Several studies characterizing soft actuators measure only the blocking force, by constraining actuator movement [39; 20; 56]. While this gives the peak force capacity, it gives no information about how the force evolves with actuator displacement. In some other studies, interaction forces are measured as the actuator moves through a specific range of motion [57; 10; 53]. However, the enforced displacement, parametrized by a single variable such as distance or curvature, forms only a small subset of possible displacement as soft actuators have virtually infinite degrees of freedom. Furthermore, these studies do not consider how the actuator is constrained to its surroundings, which influences its displacement as well as interaction forces. For example, the nature of contact between the actuator and its surroundings for an inchworm robot [58; 59; 46] is significantly different than that in a gripper [48; 47] or an assistive glove [20; 40], even though the same actuator can potentially be used for all three applications. As a result, existing methods for characterization do not consider true loading conditions of the target application, and the characterization results do not represent the expected actuator behaviour. Additionally, these studies are unable to convey information about the magnitude and direction of the resultant force, or about force distribution; as the force is measured at a

single location, and in a single axis.

In this chapter, we introduce a novel multi-DoF experimental protocol for characterizing soft actuator mechanical performance. This protocol addresses three critical factors that govern soft actuator behaviour: *anchoring conditions*, *displacement boundary conditions* and *actuation power*. In order to conduct such multi-DoF characterization, we designed, prototyped and tested a novel robotic platform. This modular and reconfigurable platform is capable of extensively characterizing soft actuators in diverse loading conditions, irrespective of soft actuator design and materials. We demonstrate this approach by characterizing a bending soft actuator in three loading conditions. We observed independent and distinct force and displacement behaviour for the same actuator which highlights the significance of loading conditions. This approach represents a step forward towards accurate and repeatable characterization beyond just “blocked forces” that are often measured by previous studies [39; 20; 56], thereby leading to an improved understanding of soft actuator mechanical behaviour.

1.2 Interaction forces of soft actuators

In addition to actuator design properties, i.e. geometrical shape and material properties, the following aspects critically affect soft actuator displacement and interaction forces:

- *Anchoring conditions*: These correspond to the location and nature of contact between the soft actuator and its surroundings, representing the physical interface between the two.
- *Displacement boundary conditions*: These correspond to the actuator displacement at the contact locations.
- *Actuation power*: These represent the input to the actuator. It corresponds to air pressure for pneumatically powered robots, voltage or current for electrically powered robots, and so on.

In order to recreate true loading conditions, we propose to physically simulate the above and measure interaction forces, such that the characterization data will reflect the expected actuator behaviour accurately. However, due to the large set of possible loading scenarios and virtually infinite degrees of freedom of soft actuators, it is evident that testing in all possible configurations with such an approach is not practically achievable. Therefore, in this study, we restrict to only two *anchoring conditions*, hinge and cantilever constraints, and focus on a bending actuator [60] in three commonly observed application scenarios [58; 59; 46; 47; 48; 49; 42; 43; 20; 40]:

- **Pulling force** using double hinged constraints: Both ends of the actuator are constrained to hinge joints that allow free rotation, but prevent translational motion (Fig. 1.2A). An

example of such a condition is observed in inchworm robots [58; 59; 46], or for producing motion to pull an object towards itself.

- **Tip loading** using cantilever-hinge constraints: One end of the actuator is fixed while the other end has a hinge constraint (Fig. 1.4A). Such a condition is observed in grippers [47; 48; 49] or in the legs of a walking robot [42; 43], in which one end is fixed to the robot body while the other is in contact with the ground.
- **Three-point bending** using hinge-cantilever-hinge constraint: The two ends of the actuator are constrained to hinge joints, and the middle section is fixed (Fig. 1.6A). Such a condition is seen in wearable robots, which typically have multiple contact locations. For instance, a glove in which one end is strapped to the fingertip, the other end to the back of the hand, and the middle section is strapped to the knuckles [20; 40].

1.3 Experimental setup and protocol

Here we characterize a bending soft actuator [60] in the three loading conditions defined previously: pulling force, tip loading and three-point bending.

1.3.1 Experimental setup

We designed a novel robotic platform (Fig. 1.1) for conducting multi-DoF characterization of soft actuators. By virtue of its modular and reconfigurable design, this device can be used to characterize soft actuators of different sizes and actuation mechanisms, namely extension, contraction and bending. It has three main components:

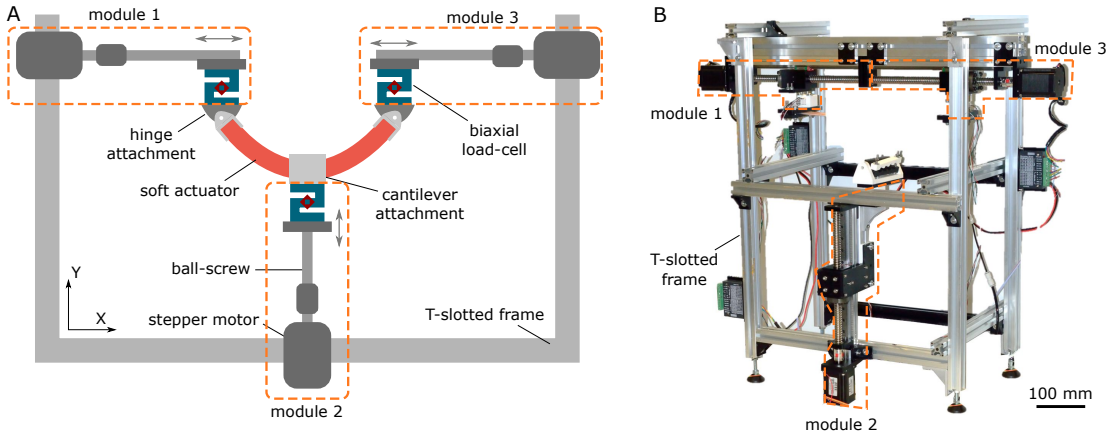


Figure 1.1: Experimental setup: A novel robotic platform for characterization of soft actuators. The reconfigurable device consists of a rigid *frame* for structural support, *attachments* for enforcing *anchoring conditions*, and *modules* with motors and biaxial load-cells for enforcing *displacement boundary conditions* and for measuring interaction forces respectively. (A) Schematic showing the different components, and (B) The fabricated prototype.

- *Modules*: These are used for enforcing *displacement boundary conditions*, and for measuring interaction forces at the contact locations. Each *module* has a linear motor (Fuyu Motion) consisting of stepper motor and ball-screw, with a total span of 0.2m and resolution of 50 μm . For measuring interaction forces, each *module* has a beam-type biaxial load-cell (Sensor and Control Co., Ltd.), which can measure 160 N in X and 80 N in Y directions, with an accuracy of 0.08 N and 0.04 N respectively. By using one *module* per contact point, this modular platform enables the study of force distribution for a multi-contact loading condition. In this study, we use three *modules*, marked as 1 to 3 in Fig. 1.1. *Modules* 1 and 3 are arranged horizontally, co-axial with each other while *module* 2 is arranged vertically as shown in the figure. Each *module* consists of a mounting plate for affixing the *attachments*.
- *Attachments*: These are actuator-specific, anchoring-specific custom designed components that enforce the desired *anchoring conditions*. They are then affixed to the *modules* using the mounting plates, and then clamped to the actuator at the desired contact locations. In this work, we designed two types of *attachments*, one each for enforcing hinge and cantilever constraint. We fabricated them by 3D printing, followed by manual assembly.
- *Frame*: The *frame*, fabricated using T-slotted aluminium profiles, provides structural support and allows to reconfigure the location of the *modules*. In the current prototype, we can characterize actuators of different sizes, with a maximum span of 0.4m x 0.2m x 0.3m in the XYZ space.

For characterization, we affix the soft actuator to the appropriate *attachments* to enforce the desired anchoring conditions, and then use the *modules* to enforce the desired displacement. While doing so, we measure the interaction forces using the load-cells on the *modules*. The position control of the *modules* is carried out open-loop, using TB660 stepper motor drivers. Load-cell outputs are amplified using a 24-bit ADC, Hx711. The amplified and digitized sensor readings are processed by reading a 6-sample set, ignoring the highest and lowest reading, and then using a moving average filter for the remaining 4 samples. The load-cell data is read at an average of 7.75 Hz, limited due to the use of HX711 amplifiers. Here, as we characterize in quasi-static loading conditions, a high sampling rate is not required. The stepper motor consumes current up to 2A, which can potentially induce electromagnetic noise in the load-cell signal. On investigation, however, we did not observe any such effects in our setup.

Prior to testing, the three load-cells were calibrated. Standard brass weights in increments of 50 grams were placed on each load-cell and their output was recorded and averaged for 10s to get the six calibration factors (X and Y directions for each load-cell). Before the start of each test, the initial reading from each load-cell was noted. All readings during the test were measured with respect to this initial value, thus, corresponding to the differential force.

1.3.2 Pulling force

We clamped the two ends of the actuator with the hinged *attachments*, one each on *module* 1 and 3 as shown in Fig. 1.2A.

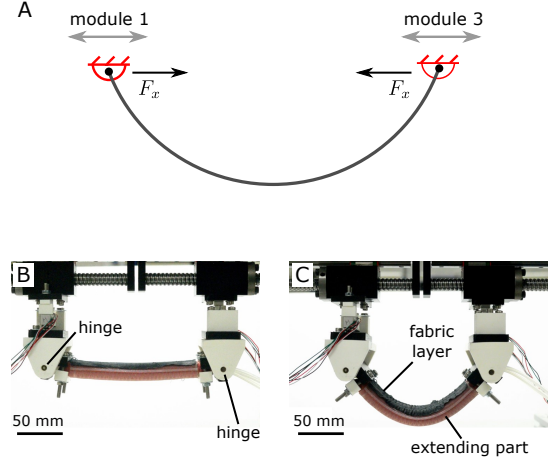


Figure 1.2: Pulling force characterization of the soft bending actuator. (A) Anchoring conditions and measured forces: we used hinged *attachments* to anchor the two ends of the actuator on *modules* 1 and 3. F_x is the mean horizontal force measured from the two *modules*. We took F_x as positive when the forces applied by the actuator on the *modules* were in the direction of the arrows. (B) The actuator held flat between the *modules*, and (C) The actuator in bent configuration. When pressurized, actuator extension is prevented on one side by a fabric layer, thereby generating a bending motion.

Displacement boundary conditions

Actuator displacement in this condition depends only on the distance between the hinges due to free rotation at the ends. Therefore, we enforce linear displacement on the hinges to move the actuator from flat (Fig. 1.2B) to bent shape (Fig. 1.2C) and then back to the initial position. We took the linear displacement as 0mm when the hinges were furthest from each other. The maximum enforced linear displacement was 80mm when the hinges were closest to each other.

Control and data measurement

We controlled *modules* 1 and 3 in opposite directions to enforce linear displacement to the tips of the actuator. For quasi-static conditions, the speed of the *modules* was maintained at 1.5 mm/s. We characterized the actuator pulling force for nine pressures from 0 kPa to 200 kPa, in steps of 25 kPa, repeated thrice for each. The pressure was generated using an off-board compressor and controlled using a digital pressure regulator (SMC). The measured parameters were the horizontal and vertical forces from *modules* 1 and 3, pressure, and positions of the *modules*. While this includes four measurements from the load-cells, we expect the horizontal

forces to be equal and opposite, while both vertical forces will be zero. We take this force, F_x , as the average horizontal force from *modules* 1 and 3, with the arrows in Fig. 1.2A depicting sign conventions.

1.3.3 Tip loading

We clamped one end of the actuator on *module* 1 with a cantilever attachment, and the other end with a hinge *attachment* on the *module* 2, as shown in Fig. 1.4A.

Coordinate system

We define a new coordinate system to express the planar space around the actuator tip, as shown in Fig. 1.3.

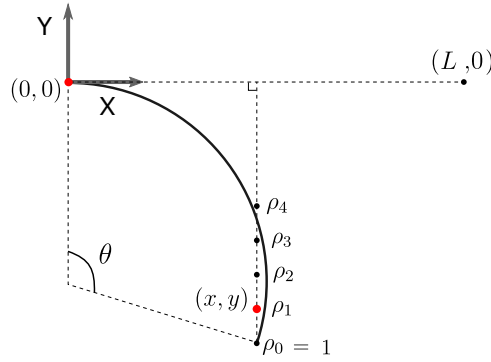


Figure 1.3: Coordinate system for tip loading. L is the arc length equal to actuator length, and θ is the arc curvature. ρ scales the Y coordinate of the arc endpoint. Using θ and ρ , we define the new coordinate system to express the planar space around the actuator tip. The two red points correspond to the locations of the actuator tips. One tip is at the origin, while the other is at (x, y) , which is given by Eq. 1.1.

Consider an arc with one endpoint at the origin, curvature θ and arc length L equal to length of the actuator. The second arc endpoint fixes the X -coordinate for a given value of θ . We then define ρ , which determines the Y -coordinate, as shown in Fig. 1.3. Using this, we get a direct mapping from the θ - ρ space to the X - Y space as follows:

$$x = \frac{L \sin \theta}{\theta}, \quad y = \frac{L(\cos \theta - 1)\rho}{\theta} \quad (1.1)$$

Using θ and ρ , we define a region, shaded in Fig. 1.4B, around the tip of the actuator, given by the fixed intervals: $\theta = [0, \pi/2]$ and $\rho = [0.6, 1]$.

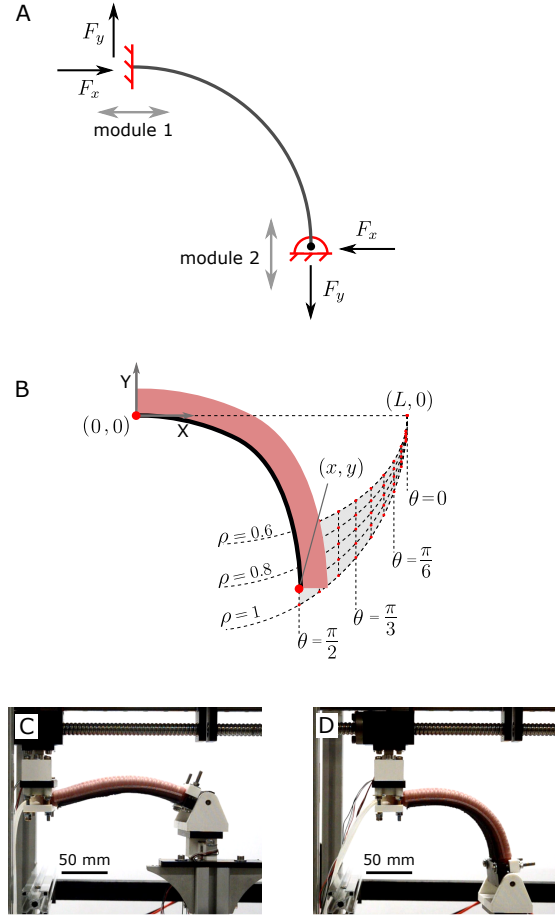


Figure 1.4: Tip loading characterization of the actuator. (A) Anchoring conditions and measured forces: we constrained one end of the actuator in a cantilever *attachment*, and the other in a hinge *attachment*. F_x and F_y are the mean horizontal and vertical forces measured at *modules* 1 and 2. We took them as positive when the forces applied by the actuator were in the direction of the arrows, (B) Displacement boundary conditions: we moved the endpoint of the actuator to each grid point, marked red in the shaded region. The X-Y coordinates of these grid points are calculated using Eq. 1.1 for ten values of $\theta : 0, \pi/18, 2\pi/18, \dots, \pi/2$; and five values of $\rho : 0.6, 0.7, 0.8, 0.9, 1$, (C) The actuator held flat between the *modules*, represented by $\theta = 0$, and (D) The actuator in bent configuration, represented by $\theta > 0$.

Displacement boundary conditions

We define a grid of points, using ten values of $\theta : 0, \pi/18, 2\pi/18, \dots, \pi/2$; and five values of $\rho : 0.6, 0.7, 0.8, 0.9, 1$. These are highlighted in red in Fig. 1.4B. We then plan a trajectory to move and hold the hinged end of the actuator at each of these grid points sequentially. Starting from $\theta = 0$ and $\rho = 0.6$, we increase ρ in steps of 0.1, with a time interval of 10s. Once ρ reaches 1, θ is incremented by $\pi/20$, and ρ is reset to 0.6. The entire trajectory consists of increasing θ from 0 to $\pi/2$ and then decreasing it back to 0. With a total of 20 steps for θ , each having 5 steps of ρ , a total of 100 steps are taken. While enforcing these *displacement boundary conditions*, the θ - ρ coordinate system does not represent actuator shape, rather it corresponds to the

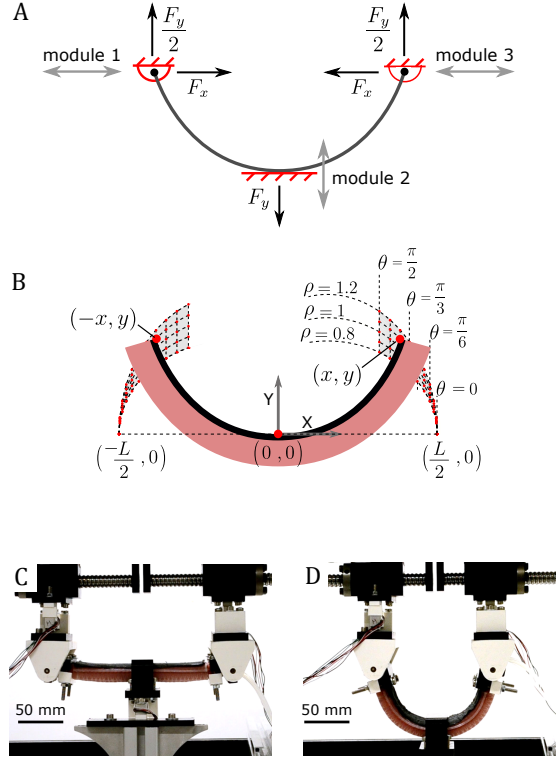


Figure 1.6: Three-point bending characterization of the actuator. (A) Anchoring conditions and measured forces: we constrained the two ends of the actuator in hinge *attachments* and the middle section in a cantilever *attachment*. F_x and F_y are the mean horizontal and vertical forces from the *modules*. We took them as positive when the forces applied by the actuator were in the direction of the arrows. (B) Displacement boundary conditions: we symmetrically moved the two endpoints of the actuator to the grid points, marked red in the shaded region. The X-Y coordinates of these grid points are calculated using Eq. 1.2 for ten values of $\theta : 0, \pi/18, 2\pi/18, \dots, \pi/2$; and five values of $\rho : 0.8, 0.9, 1, 1.1, 1.2$, (C) The actuator held flat between the *modules*, represented by $\theta = 0$, and (D) The actuator in bent configuration, represented by $\theta > 0$.

$$x = \frac{L \sin \theta}{2\theta}, \quad y = \frac{L(1 - \cos \theta)\rho}{2\theta} \quad (1.2)$$

Using θ and ρ , we define a region, shaded in Fig. 1.6B, around the tips of the actuator, given by the fixed intervals: $\theta = [0, \pi/2]$ and $\rho = [0.8, 1.2]$.

Displacement boundary conditions

We created a grid of points using ten values of $\theta : 0, \pi/18, 2\pi/18, \dots, \pi/2$ and five values of $\rho : 0.8, 0.9, 1, 1.1, 1.2$. These grid points are highlighted in red in Fig. 1.6B. The ends of the actuator were symmetrically moved to each of these grid points sequentially, starting from $\theta = 0, \rho = 0.8$ to $\theta = \pi/2, \rho = 1.2$, and back. While enforcing these *displacement boundary conditions*, the θ - ρ coordinate system does not represent actuator shape, rather it corresponds to the location of the actuator tip.

Control and data measurement

To enforce the ends of the actuator to the grid points, *modules* 1 and 3 followed the trajectory of $-x$ and x respectively, and *module* 2 followed a trajectory of $-y$. The actuator was held in each point in the grid and the interaction forces at the three locations were measured. This was carried out for nine inflation pressures from 0 kPa to 200 kPa in steps of 25 kPa, and repeated thrice for each inflation pressure, to give a total of 27 runs, and a total time of 27,000s (7.5 hours).

In ideal conditions with perfect symmetry, we expect the horizontal force on *module* 2 to be zero. In practice, however, a residual force was observed as the actuator buckled to one of the sides. However, as it was almost an order of magnitude lower than the other forces, we only consider the vertical force component at *module* 2. For *modules* 1 and 3, we expect the horizontal forces to be equal and opposite due to symmetry. Furthermore, the vertical forces on *modules* 1 and 3 will be equal, and their sum will be equal to the vertical force on *module* 2. Thus, there are again two independent forces. We took F_x as the mean horizontal force from *modules* 1 and 3, and F_y as the mean vertical force from *modules* 1, 2 and 3, as shown in Fig. 1.6A, with the arrows depicting sign conventions.

1.4 Results and discussion

Here, we analyze how the measured interaction forces were affected by the *anchoring conditions*, *displacement boundary conditions* and *actuation power*.

1.4.1 Pulling force

Fig. 1.7 shows the actuator pulling force at four pressures. The pulling force increases with pressure and decreases with displacement. We also observe that the force vs. displacement behaviour of the actuator shows a similar trend for the different pressures, with changing X-intercepts. These results are consistent with those from conventional studies characterizing SPA pulling force [57; 20; 54].

1.4.2 Tip loading

Fig. 1.8 shows the evolution of the tip horizontal force, F_x , at varying pressures, θ and ρ . We observe that for a given value of ρ , F_x shows a similar trend with θ for different pressures. However, this trend changes significantly when ρ is varied. Based on how we defined the θ - ρ coordinate system, we expected F_x to always reduce with increasing θ . However, from Fig. 1.8 we see that the opposite trend is observed for some values of θ , ρ and pressure. Our experimental protocol with planar *displacement boundary conditions* helps to capture this behaviour, which is otherwise not observable with conventional methods.

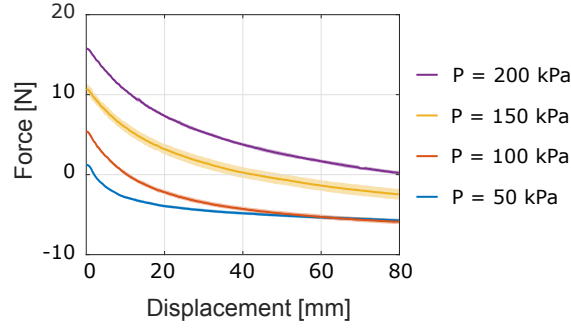


Figure 1.7: Mean pulling force, F_x , of the actuator vs. displacement, x . The pulling force increases with pressure and decreases with x . The shaded region corresponds to one standard deviation of the measured data.

Table 1.1: RMS errors between measured values and the regressed model for interaction forces during tip loading

Force	Peak Force	RMS error
F_x	12.63 N	0.57 N
F_y	5.78 N	0.58 N

We used linear regression to fit a second-order model to the measured data as:

$$F_{x,y} = f_{x,y}(P, x, y, \theta, \rho) \quad (1.3)$$

where $f_{x,y}$ are second order models, $F_{x,y}$ are the measured forces, P is the internal air pressure, x and y are the X and Y coordinates of the tip, and θ and ρ represent the tip location using the coordinate system in Fig. 1.3.

Table 1.1 shows the root mean square (RMS) errors between the fitted model and measured values. Additionally, the error bars in Fig. 1.8 also signify the RMS errors between the model and measured values. Despite rigorous testing of over 7 hours, the model is able to capture the soft

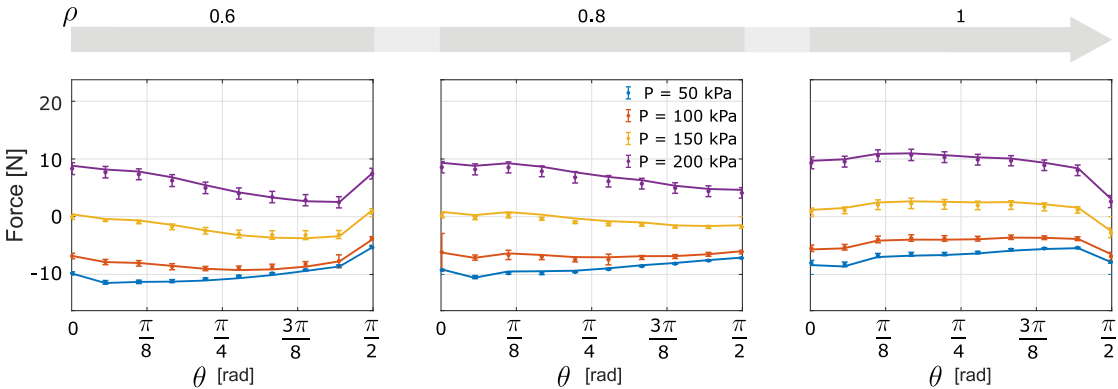


Figure 1.8: Mean horizontal force, F_x , of the actuator during tip loading, measured at varying pressures, θ and ρ . The data markers correspond to measured values and the lines correspond to the fitted model. The error bars signify the RMS errors between the model and measured data.

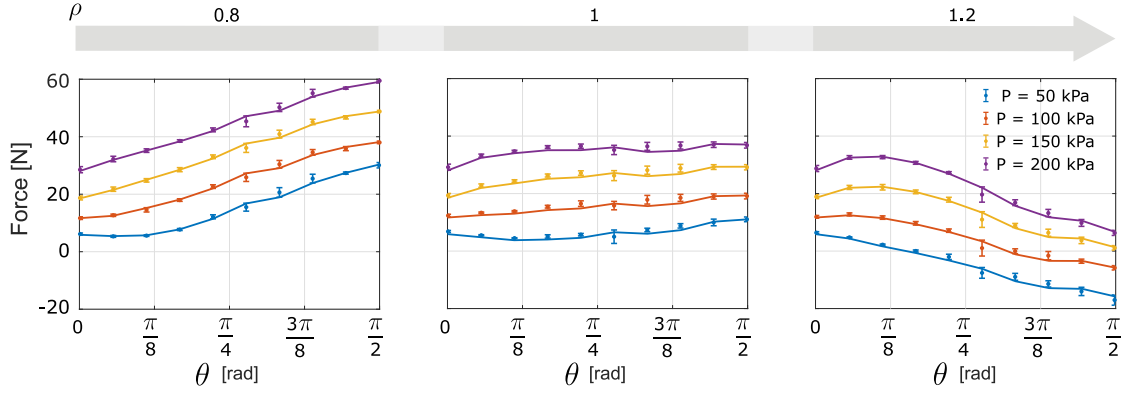


Figure 1.9: Mean vertical force, F_y , of the actuator during three-point bending measured at varying pressures, θ and ρ . The data markers correspond to measured values, and the lines correspond to the fitted model. The error bars signify the RMS errors between the model and measured data.

Table 1.2: RMS errors between measured values and the regressed model for interaction forces during three-point bending

Force	Peak Force	RMS error
F_x	40.15 N	1.10 N
F_y	56.27 N	1.48 N

actuator mechanical behaviour well, thus highlighting the repeatability of our experimental protocol.

1.4.3 Three-point bending

Fig. 1.9 shows the evolution of the vertical force, F_y , with varying pressures, θ and ρ . Similar to tip loading, the behaviour of force vs. θ , shows a similar trend for a given ρ , at different pressures. With varying ρ , however, we observe markedly different behaviour. Additionally, we see that the force magnitude in three-point bending is in general, higher than both tip loading and pulling. This is because in the other two cases, the actuator is constrained only at the ends, and its remaining body is free to bend in the unconstrained sections. In case of three-point bending, an additional constraint acts at the central portion of the actuator, preventing its motion, thereby leading to higher interaction forces.

Similar to tip loading, we used regression to fit a second order model to the measured data. The RMS errors are given in Table 1.2. While the magnitudes of RMS errors are higher than those during tip loading, the relative errors are lower. Additionally, the error bars in Fig. 1.9 also signify the RMS errors between the model and measured values. As can be seen from the table and figure, the regressed model is able to capture the actuator mechanical behaviour closely.

Using the fitted model, we calculated the magnitude of the resultant force vector ($F_x, F_y/2$) acting on the tip of the actuator, for a range of θ and ρ . This is shown in Fig. 1.10 for an

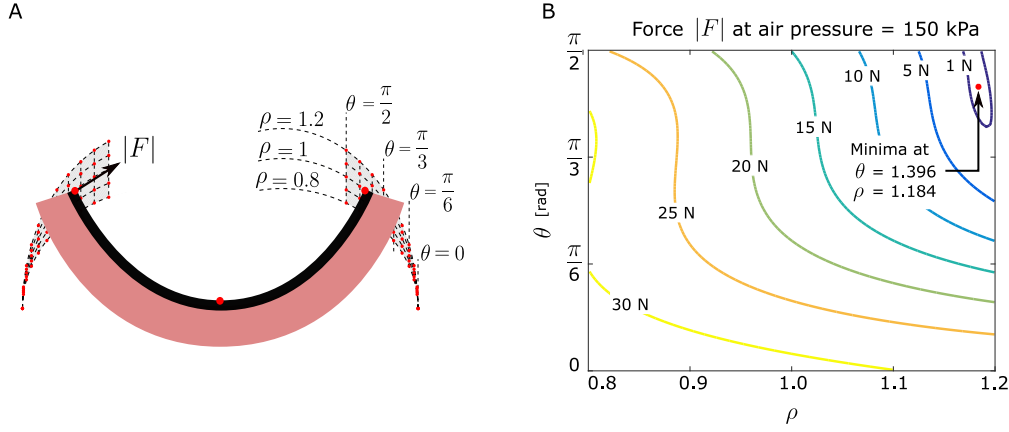


Figure 1.10: Predicted resultant force, $|F|$, at the left tip of the actuator in three-point bending; at an air pressure of 150 kPa. (A) Figure depicting planar displacement showing a grid of θ and ρ , and the resultant tip force with magnitude $|F|$, and (B) Magnitude of resultant force at varying θ and ρ . The point of minimum force ($|F| = 0.244$ N) is marked in red.

actuation pressure of 150 kPa. This contour plot represents the stiffness of the actuator in the planar space. Furthermore, the minima, marked in red, corresponds to the neutral position of the actuator when pressurized to 150 kPa, as it has the minimum resultant tip force ($|F| = 0.244$ N). Comparing with the measured data, the displacement with minimum resultant force corresponds to $\theta = 1.396$ and $\rho = 1.2$, which is close to that predicted by the fitted model. As the magnitude of the force is almost zero, these values of θ and ρ represent the actuator displacement in free or unconstrained conditions at an inflation pressure of 150 kPa.

1.5 Characterization of a meso-scale fingertip haptic device

The experimental characterization protocol presented in this chapter enables us to physically recreate true loading conditions around soft robots, in order to measure their application-specific mechanical behaviour. In this section, we implement the presented methodology for the characterization of meso-scale haptic robots.

The field of haptics aims at better understanding different types of feedback such as compliance, texture, pressure, movement and temperature, in order to artificially reproduce these sensations to the user. Recently, there has been a flourishing interest in haptic devices for the fingertips, due to their high sensitivity and importance in manipulation. Many fingertip haptic devices have been developed to provide motions such as compression, roll, pitch and vibrations [67; 68; 69; 70; 71; 72; 73]. Assessing the mechanical behaviour of such devices is important in order to generate a realistic sensation on the wearer's fingertips. However, due to the compact meso-scale (1 to 10 cm) and multiple DoF of these devices, evaluation of mechanical outputs is challenging. Accordingly, most studies with fingertip haptic devices assess the performance using user surveys or via characterization in a small range of motion [33]. Therefore, although actuation levels are controllable, it is difficult to surmise how much forces are actually being applied.

1.5. Characterization of a meso-scale fingertip haptic device

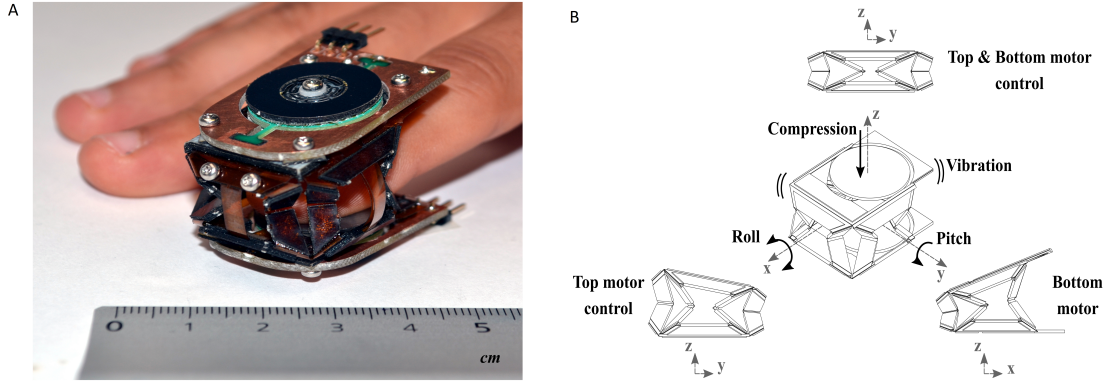


Figure 1.11: Haptigami presentation: (A) pictured on the user's fingertip; overall dimensions: 36 x 25 x 26 mm and 13 g. (B) Haptigami renders vibrotactile and 3-DoF cutaneous feedback.

Here we implement our multi-DoF experimental protocol for characterizing a meso-scale haptic device, which would enable us to establish the link between the force characteristics of the device and the psychophysical sensations felt by the user. We reconfigure the multi-DoF characterization setup into a 5-DoF robotic platform and characterize the force output of a fingertip haptic device in its full range of motion. Contrary to the commonly used user-surveys, this method allows to objectively measure mechanical performance and can be readily implemented with most other fingertip haptic devices as well as meso-scale systems. By comparing different such devices along with user surveys, we would be able to link and quantify the relation between multidimensional force output and perceived sensation by the user.

1.5.1 *Haptigami*: the origami-inspired fingertip haptic device

The *Haptigami* (Fig. 1.11) is a novel, compact fingertip haptic device capable of delivering vibrotactile and 3-DoF cutaneous feedback. It consists of two low-profile, high-force density piezo-motors that power four low-profile slider-crank mechanisms, all integrated in an Origami-inspired 3D base structure. When powered, the piezo-motors drive the slider-crank mechanisms that pull kapton tendons, which makes the *Haptigami* move. The different kinds of motion and the corresponding actuation inputs are detailed in Fig. 1.11B and Table 1.3. Measuring 36x 25 x 26 mm and 13 g, the *Haptigami* is the smallest and most lightweight fingertip haptic device, as compared to devices providing similar types of haptic feedback. More details of the design and fabrication of *Haptigami* are described in Giraud et al. [61].

Chapter 1. Multi-DoF characterization of soft actuators

Table 1.3: Haptigami motion achieved through motors direction of rotation, clockwise (cw) or counter-clockwise (ccw)

Top motor direction	Bottom motor direction	Haptigami motion
ccw	-	roll(+)
cw	-	roll (-)
-	cw	pitch (+)
ccw	ccw	compression

1.5.2 Experimental setup and protocol

We affix the top and bottom sides of the *Haptigami* using custom 3D printed attachments, enforce the displacement boundary conditions in the full range of motion of the device, and measure its interaction forces in its three actuation modes: compression, roll and pitch, and vibrotactile feedback.

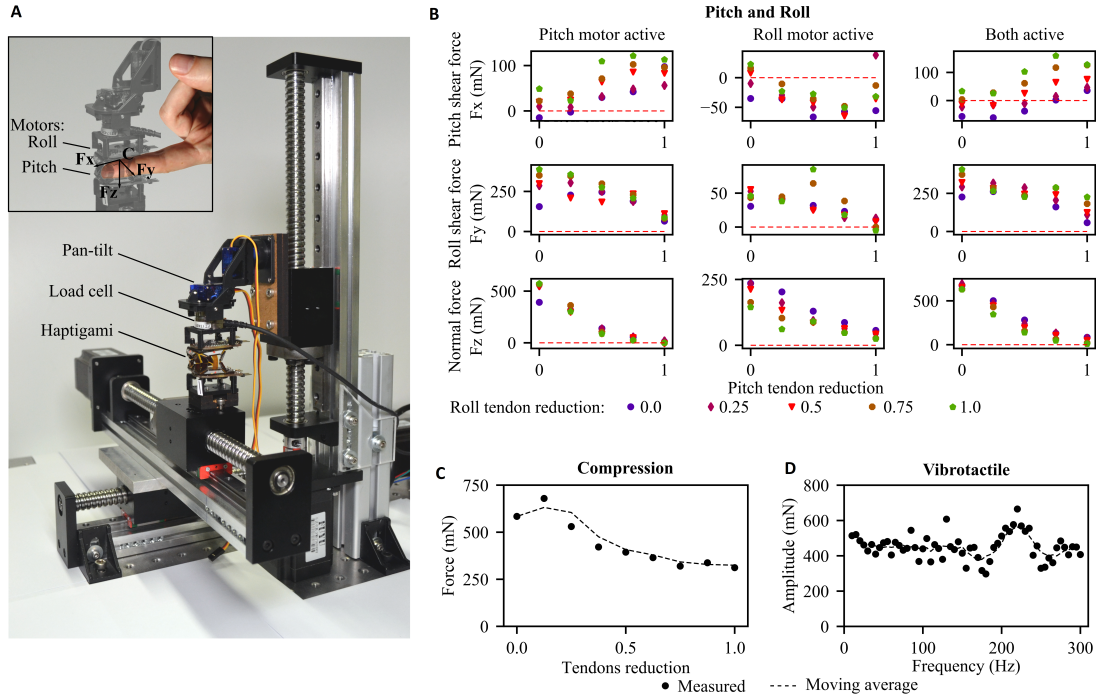


Figure 1.12: Force characterization setup and results: (A) Force characterization setup simulating the platform on a finger; we fixed the Haptigami to the 5-DoF platform in direct contact with the 6-DoF load cell. (B) For every orientation of its workspace, we measured the force along XYZ axis depending on the actuated motors. The configuration is defined from the normalized tendon length reduction that corresponds to how much the tendon has been pulled by the slider-crank. (C) Compression experiment, we attached Haptigami to the platform with a null angle. For different heights, we actuated the roll motors and measured the compression force. (D) Vibration experiment, we attached Haptigami to the platform with a null angle and control the top motor to move back and forth at different frequencies and measure the amplitude of the resulting signal.

Experimental setup

We adapt the experimental setup in Fig. 1.1 into a 5-DoF robotic platform as shown in Fig. 1.12A. It consists of three linear motors or stages, to enforce linear displacement in X, Y and Z axis and a pan-tilt mechanism consisting of two servomotors for roll and pitch motions. We affixed the bottom face of Haptigami to the X-Y stages, and the top plate to the pan-tilt mechanism which in turn is fixed on the Z stage as seen in Fig. 1.12A. By controlling these linear motors and pan-tilt mechanism of the characterization platform, we can displace the top plate of the Haptigami in XYZ and roll-pitch directions respectively. While enforcing the displacement, we measure the blocked force of Haptigami using a *Nano17* 6-axis force sensor from *ATI Industrial Automation* (force resolution = 12.5 mN), attached between the top face of the Haptigami and the pan-tilt mechanism as seen in Fig. 1.12A. With this setup, we moved Haptigami to different configurations in its range of motion and characterized it in three scenarios: (i) compression motion (ii) roll and pitch motions (iii) vibrotactile feedback. For all these conditions, we define the *Haptigami* displacement using its input space defined via its tendon length reduction defined as:

$$\text{normalized tendon reduction} = \frac{L_0 - L}{L_0}$$

where L is the current tendon length and L_0 is maximal tendon length, in mm.

Compression

We controlled the characterization platform to only move its Z stage, and displaced Haptigami from an initial height of 20 mm to a final height of 16 mm in steps of 0.5 mm. We activated both motors according to Table 1.3 and measured the maximum compression force at each step, held for 2 s.

Pitch and roll

We approximate the fingertip as a sphere and assume that the bottom side of the *Haptigami* rolls without sliding. This assumption is valid for our analysis because the *Haptigami* pitches only in the forward direction and therefore does not interact with the proximal side of the finger. The derivation of the *Haptigami* kinematic model with this assumption is described in Section A1, which relates the spatial configuration of the *Haptigami* (x, y, z, δ, ψ) to the input control, which is the normalized tendon length.

We displaced the Haptigami in a set of points defined by a grid of 5 x 5, where each grid point corresponds to the front and side tendon lengths, with a maximum value of 2 mm on each side. This motion corresponds to a total pitch of +10° and roll of +12°, assuming a sphere of 14 mm diameter placed inside. We calculated the spatial orientation (x, y, z, δ, ψ) of Haptigami at the grid points using the kinematic model described in Section A1. Using these values

and appropriate rotational and translational transformation matrices, we converted these displacements to those required by the 5-DoF robotic platform. For every grid point, we used the following protocol: 1. Move Haptigami to a new position, 2. Activate pitch motor, 3. Activate roll motor, 4. Activate both motors. We programmed each motor activation to last two seconds and then come back to the initial position.

Vibrotactile feedback

Haptigami can generate a vibrotactile feedback by alternating its motors rotations at high speed. We powered the top motor at a range of frequencies between 10 and 300 Hz, which correspond to the maximum human perception frequency [74]. We then measured the force amplitude generated, while holding the *Haptigami* in its zero displacement position.

1.5.3 Results

The measured forces vs. displacement for the different actuation modes are detailed in Fig. 1.12 and Table 1.4. Fig. 1.12C shows the measured force vs. displacement during compression. We see that the compression force slightly reduces with increasing displacement, with a maximum value of 678 mN. This can be attributed to the passive stiffness of the *Haptigami*, which resists some of the forces of the tendons.

Fig. 1.12B shows the measured forces vs. normalized tendon length reduction of Haptigami during pitch and roll. The Y axis represents the measured forces, while the X axis and different markers represent displacements in the pitch and roll directions respectively, expressed in normalized tendon lengths. These forces are generated by the front and side tendons pulled by the pitch and roll piezo-motors respectively. Therefore they depend on the relative orientation of the tendon force with respect to the top face, as well as its magnitude, which depends on the torque of the piezo-motor and orientation and design of the slider-crank mechanism. With increasing pitch, the component of the tendon force in the X axis increases. This leads to a positive correlation in force vs. displacement for the X direction and a negative one for the Y and Z directions, as seen in the first column of Fig. 1.12B. A similar pattern is expected for the roll direction, but the measured data does not completely follow this, as seen in the second column of Fig. 1.12B. This deviation could be attributed to mechanical interference in the compliant transmissions due to the fact that both motors contribute to the roll motion. The third column of Fig. 1.12B corresponds to both motors active, pulling in roll and pitch directions. Therefore, the plots are somewhat equal to the sum of the first two columns, which we found was especially true for F_z . Another observation is that the forces are generally higher for pitch motor active, as compared roll motor active. This is because the crank radius for the slider-crank mechanism is smaller for the former as compared to the latter, as detailed in [61]. Lastly, due to the underactuated and coupled design of the Haptigami, we see from the third row of Fig. 1.12B that shear forces are always accompanied by compression forces. The maximum forces are 690 mN in normal force, 407 mN in shear roll and 159 mN in shear pitch.

Fig. 1.12D shows the measured peak-to-peak force difference for vibrotactile actuation at the various tested frequencies. Other than the small peak at around 220 Hz, the force characteristics seem constant across the frequency range, with a mean value of 451 mN and a standard deviation of 73 mN. While we tested only the top motor here, we believe that using both motors will increase the force amplitude.

Table 1.4: Table summarizing the maximum normal, shear and vibrotactile force capacity of our device.

	Force (mN)		
	Pitch shear	Roll shear	Normal
Pitch motor	121	387	572
Roll motor	38	85	235
Two motors	159	407	693

Compression: 679 mN; Vibration amplitude peak: 664 mN (single motor)

1.6 Discussion

In this chapter, we presented a novel experimental protocol for characterizing soft actuator interaction forces by actively controlling *displacement boundary conditions*, *anchoring conditions* and *actuation power*. To implement such a multi-DoF protocol, we designed a novel modular robotic test platform, which can extensively characterize soft actuators in a diverse set of loading conditions. Using this platform, we tested a bending soft actuator in three loading conditions and observed distinct mechanical performance in the three cases. This systematic protocol helps to closely recreate true loading conditions, which leads to accurate and repeatable prediction of soft actuator performance. The methodology presented in this work is a step towards better understanding the impact of loading conditions on actuator mechanical behaviour. This can contribute towards optimization of soft actuator design and control, thereby enhancing their scope of application.

In addition to the bending SPA-pack, we used this method to characterize a meso-scale fingertip haptic device. The results helped to affirm that the *Haptigami* can generate forces (ranging from 150 to 690 mN in different actuation modes) well above the human skin perception threshold of around 41 mN as described by [75]. While analytical methods for modelling forces at the meso-scale are challenged by non-linearities such as friction or backlash, experimental results using this method can be used to develop data-driven models for the *Haptigami* as well as meso-scale devices in general. By comparing different devices and by additionally conducting user studies, we would be able to link and quantify the relation between mechanical output of a meso-scale haptic device to the psychophysical sensations felt by the user. This represents a direct measurement and characterization of the physical human-robot interface, and can help us in future studies to better understand how such haptic, cutaneous or kinaesthetic sensations affect the user.

Some possible future directions include testing in dynamic conditions and in more anchoring

conditions opposed to the quasi-static testing in two anchoring conditions of the present study. Such additional anchoring conditions could include multiple contact points, impedance at the contact point, or surface contact rather than point contact. By testing a given actuator in such diverse loading, we could develop a general understanding of how loading conditions affect mechanical performance. At the same time, however, it must be acknowledged that this method represents an approximation of the true loading conditions. Furthermore, such experimental characterization would not be sufficient in applications which involve varying loading conditions, for instance, a mobile robot crawling in changing terrain. Lastly, it would be challenging to recreate some type of loading such as contact with granular medium such as sand or soil, stick-slip phenomenon on wet/viscous surfaces, or deformable surface contact. For such conditions, employing analytical or numerical methods in addition to our presented method would be more suitable. Despite these limitations, however, the presented experimental protocol for characterizing soft actuators still represents a step towards better understanding the mechanical behaviour of soft robots while complementing and reinforcing the results from analytical or numerical methods.

2 Modelling and parametric study of pneumatic supply systems

In addition to the static mechanical output of soft robots, studied in Chapter 1, their dynamic behaviour is also a critical performance metric as seen in Fig. 3. Despite its importance, for the case of the widely used SPAs the dynamic response is still not fully understood. This knowledge gap negatively affects the overall performance, and also makes it difficult to tailor the design of pneumatic supply systems (PSSs) for the target application. In this chapter, we address this limitation and investigate the effect of PSSs on the SPA dynamic response via modelling and experimental validation.

2.1 Introduction

A significant number of soft robots generate motion via SPAs (Fig. 2.1B) powered by pneumatic supply systems (PSSs) [16; 38; 39; 40; 22; 20; 42; 43; 44; 45; 60; 78; 79; 80; 81]. PSSs (Fig. 2.1A) typically consist of three main components: *source* for generating pressurized air, *pneumatic line* for connection, and *valves* for controlling flow direction [82]. By virtue of the pneumatic flow, PSSs govern the soft actuator pressure dynamics, and thus the overall soft robot dynamic behaviour [19; 48; 82]. In order to meet dynamic performance specifications such as rise time, fall time or actuation frequency, PSSs have to be tailored, i.e. the PSS components and their control parameters such as *source* pressure, valve duty cycle and compressor duty cycle must be selected carefully. Regardless of the soft actuator used, improper selection or control of PSS components can lead to either too slow or too fast dynamic response, or can even damage the soft actuator.

The material presented in this chapter has been adapted from the following publications:

[76] **Joshi, S., & Paik, J.** (2021). Pneumatic supply system parameter optimization for soft actuators. *Soft Robotics*, 8(2), 152-163. DOI: 10.1089/soro.2019.0134

[77] **Joshi, S., Sonar H. & Paik, J.** (2021). Flow path optimization for soft pneumatic actuators - Towards optimal performance and portability. *IEEE Robotics and Automation Letters*. *IEEE Robotics and Automation Letters*, 6(4), 7949-7956. DOI: 10.1109/LRA.2021.3100626.

S. Joshi conducted experiments, designed the hardware architecture, wrote the manuscript, and contributed to the initial concept and direction of experiments and scientific objectives. H. Sonar designed the custom script for running the hardware, and contributed to the initial concept and manuscript writing. J. Paik supervised the research objectives of the work.

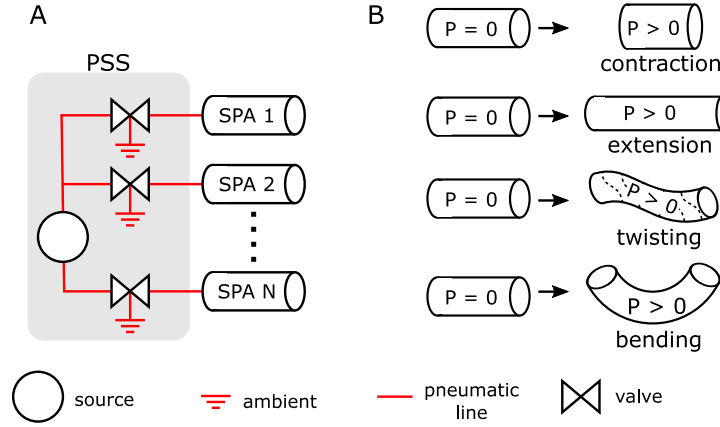


Figure 2.1: A pneumatic supply system (PSS) powering SPAs. (A) Schematic of a PSS showing the main components, (B) Different actuation patterns achieved by soft actuators when pressurized ($P > 0$).

Accordingly, researchers have studied some aspects of PSSs for soft robotic applications. Wehner et al. [82] compared portability and relative merits and demerits of different choices for the pneumatic *source* such as battery powered compressors, liquid CO_2 , and peroxide decomposition. However, this study does not include the role of *valve*, *pneumatic lines* and soft actuator design parameters such as internal volume, operating pressure and maximum expansion. Additionally, it does not investigate soft actuator dynamic behaviour. In another study [10], researchers heuristically tuned *source* pressure and valve duty cycle to increase maximum actuation frequency from 2 Hz to 4 Hz. While effective for tuning PSS control parameters, such a heuristic approach is insufficient for PSS component selection. Furthermore, it cannot predict how dynamic behaviour will be affected if the soft actuator or a PSS component is changed. By employing finite elemental analysis (FEA), Marchese et al. [45] calculated the *source* pressure required to achieve high speed inflation response in a soft robotic fish. However, their results were limited to the specific application and do not lead to a general understanding of PSSs' influence on the soft actuator dynamic behaviour. As of yet, the relationship between PSS components, soft actuator design parameters and dynamic performance is not well-quantified.

While there are numerous studies on soft actuator kinematics, deformation and force interactions using analytical modelling [24; 25; 26; 27], rigid-kinematic approximations[28; 29; 30], or FEA [31; 32], soft actuator pressure dynamics are relatively less explored. The major reasons limiting study of soft actuator pressure dynamics are: (i) non-linear nature of pneumatic flow, (ii) large variability in PSSs with respect to components and their control parameters, (iii) non-linear nature of soft actuator behaviour due to material properties, design geometry and large deformations, and (iv) large variability in soft actuator design with respect to design, materials, and operating pressures [19; 54]. As a result, soft actuator dynamic response is most commonly modelled by fitting the experimentally measured response to first or second order linear systems [39; 44; 45; 52; 83; 30; 26]. Such models do not relay information about the underlying flow mechanics, and are insufficient for customizing PSSs to meet performance requirements.

In this chapter, we address this limitation to develop a more in-depth understanding of SPA dynamic behaviour. Based on ideal gas laws and the ISO 6358 standards [84; 85], we propose a comprehensive model for pressure and flow dynamics of soft actuators. This non-linear model is applicable to a wide range of PSSs with respect to *source*, *valve* and *pneumatic line*, as well as to soft actuators with varying sizes, operating pressures and amount of deformation. Using simulations, we first investigate the effect of ten critical parameters of PSSs and soft actuators on dynamic performance, in terms of the rise time, fall time and actuation frequency. Then, we conduct an exhaustive experimental study in 162 testing conditions spanning distinct combinations of actuators, tubing sizes, source pressures and valves. While doing so, we address practical considerations such as characterizing the pressure-flow relationship for a single PSS component or the entire flow path, and compensating for valve delays. Measured values match well with the simulations and highlight interesting trends among the different parameters. One such example is the existence of an optimal tubing diameter, which maximizes actuation frequency and is unique for the set of SPA, valve, and tubing length. Our findings also highlighted two case scenarios where the model predictions did not match measured values due to SPA inertial dynamics or valve delays. These results provide practically useful insights on how PSS components and SPAs affect dynamic behaviour. In addition to improving the understanding soft actuator pressure dynamics, this work will enable design customization through selection and control of PSS components to meet the desired SPA performance.

2.2 Modelling pressure and flow dynamics

The *source* of the PSS generates the air pressure, which drives the flow through the *valve* and *pneumatic line* to the soft actuator. Based on the pressure generation mechanism, PSSs in academia and industry can be largely categorized in two configurations as shown in Fig. 2.2.

- **Configuration A:** PSSs with a pressure regulator at the outlet of either large off-board compressors, high pressure gas cylinders (20 or 30 MPaG) or liquid CO_2 cylinders (5.5 MPaG) as the *source* (Fig. 2.2A) [45; 48; 10]. Assuming perfect regulation, we model these as ***constant pressure PSSs***.
- **Configuration B:** PSSs consisting of an on-board compressor and a reservoir as the *source* (Fig. 2.2B) [7; 47; 42]. We model these as ***constant flow PSSs***.

In order to study pressure dynamics of soft actuators systematically, we use existing established models for air flow through PSS [86; 87; 88; 89; 85; 90]. In addition, we propose a new quasi-static pressure-volume relationship for modelling soft actuator expansion. The commonly used assumptions in pneumatic studies [86; 87; 88; 89; 85; 90] are as follows: (i) there is no air leakage; (ii) air follows ideal gas equations; (iii) the ambient is at standard pressure and temperature, $P_0 = 0.1 \text{ MPaA}$, $T_0 = 293.15 \text{ K}$; (iv) air compression and expansion occurs under

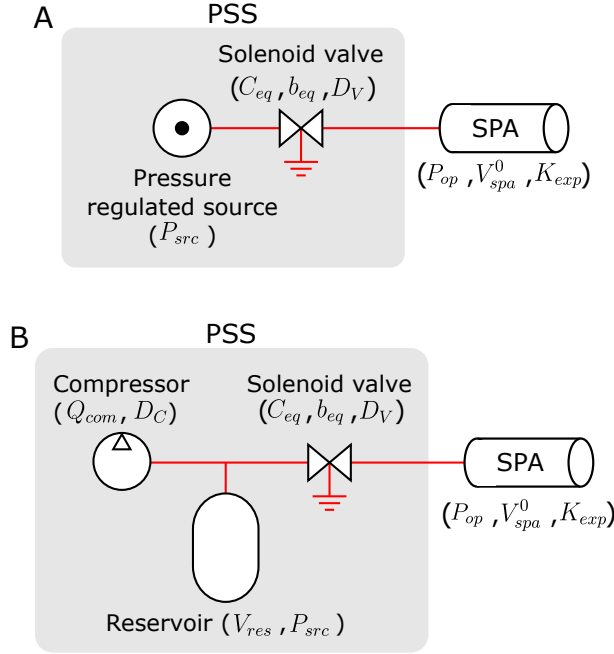


Figure 2.2: The two PSS configurations: (A) *Constant pressure PSSs*: PSS with pressure regulator at the source [45; 48; 10], (B) *Constant flow PSSs*: Compressor-powered PSS without pressure regulator [7; 47; 42].

isothermal conditions at T_0 ; (v) internal pressure for pressurized volumes at any instant is uniform, i.e. a lumped model. We apply the above assumptions in our study.

2.2.1 Modelling pressure dynamics of PSSs

For *constant pressure PSSs* (Fig. 2.2A), we have

$$\dot{P}_{src} = 0 \quad (2.1)$$

For *constant flow PSSs* (Fig. 2.2B), P_{src} is affected by inflow from the compressor and outflow to the soft actuator, Q_{spa} , where spa stands for soft pneumatic actuator. We apply ideal gas equations to derive the pressure dynamics of the reservoir as detailed in Section A2. The final expression for the pressure dynamics are then given by:

$$\dot{P}_{src} = \frac{P_0}{V_{res}} (Q_{com} - pos(Q_{spa})) \quad (2.2)$$

where P_{src} is the instantaneous reservoir pressure; V_{res} is the reservoir volume including dead volume of tubing and fittings between compressor and valve; Q_{com} is the instantaneous mass flow output of the compressor expressed in standard L/s. $pos(Q_{spa})$ is the positive part of mass flow to soft actuator, i.e. from reservoir to soft actuator.

During soft actuator inflation and deflation, air flows through the valve, tubing and fittings. We

model this flow using ISO 6358 standard [85; 84], which calculates the flow through a component using the upstream and downstream pressures, and two parameters, sonic conductance C and critical ratio b , ($0 < b < 1$), as shown below:

$$Q = C\Psi P_{High} \quad (2.3)$$

$$\Psi = \begin{cases} \sqrt{1 - \left(\frac{\frac{P_{Low}}{P_{High}} - b}{1 - b} \right)^2}, & \frac{P_{Low}}{P_{High}} \geq b \\ 1, & \frac{P_{Low}}{P_{High}} < b \end{cases} \quad (2.4)$$

where P_{High} and P_{Low} are the absolute pressures at the upstream and downstream sides respectively; C and b are the sonic conductance and critical ratio respectively, and Ψ is the flow function defined in Eq. 2.4. When the pressure ratio is below the critical value, b , the flow is choked, and only depends on source pressure. When the pressure ratio is above the critical value, the flow follows an elliptical relationship with the pressure ratio; and becomes zero at a pressure ratio of 1.

This model, an approximation of flow through an orifice, is applicable to a wide range of commercial components and has been used previously in PSSs with positive pressure [91; 92; 93; 85; 90] as well as vacuum [94; 95; 96]. It can be used with a single component, as well as the entire flow path consisting of several components connected in series or parallel networks [85]. Once the C and b for each component is known, we can calculate the equivalent parameters, C_{eq} and b_{eq} , for the entire flow path using appropriate expressions for series and parallel connections as given in Eq. A17 to A21 [85] or via online tools [97]. For *tubing*, C and b is calculated as given in Eq. A22 [85; 98]. For the *valve* and *fittings*, C and b can typically be found in the technical manual. If other specifications such as "flow coefficient" or "nominal flow rate" are reported in the technical datasheet, the ISO 6358 parameters can be roughly calculated using simple expressions in [85] or online tools such as [99]. If neither is available, they can also be experimentally characterized as described in Section 2.4.2 and Fig. 2.8. For components connected in series, C_{eq} is always lesser than the smallest sonic conductance in the component set. Therefore, each and every component in the flow path must be selected carefully to avoid bottlenecks. For example, while selecting fittings, push-in type and straight-type fittings may be selected over barbed-type and bent-type fittings respectively, as the former options have larger C [85].

2.2.2 Modelling soft actuator pressure dynamics

We model the soft actuator as a chamber with variable internal volume, V_{spa} . Similar to Eq. 2.2, we can express its pressure dynamics as (Section A2):

$$\dot{P}_{spa} = \frac{P_0}{V_{spa}} (Q_{spa}) - \frac{P_{spa} \dot{V}_{spa}}{V_{spa}} \quad (2.5)$$

where P_{spa} is the instantaneous soft actuator pressure; V_{spa} is the soft actuator internal volume including dead volume of tubing and fittings between valve and soft actuator; and Q_{spa} is the mass flow to the soft actuator expressed in standard L/s.

V_{spa} is governed by P_{spa} , soft actuator design, external forces and inertial forces. Neglecting effect of the external and inertial forces, we express the freely expanding/contracting soft actuator volume quasi-statically as a function of its pressure. The general case for a non-linear relation, $V_{spa} = f(P_{spa})$ is discussed in Section A3. For this study, however, we model a linear relationship based on the findings of [10; 53; 45; 54; 28] that reported linear pressure-volume relationships:

$$V_{spa} = V_{spa}^0 (1 + K_{exp}(P_{spa} - P_0)) \quad (2.6)$$

where we define the expansion ratio, K_{exp} , as a constant relating P_{spa} to V_{spa} ; and V_{spa}^0 is the volume of actuator at $P_{spa} = P_0$.

The soft actuator pressure dynamics, while implicitly considering internal volume dynamics, are then described by:

$$\dot{P}_{spa} = \frac{P_0 Q_{spa}}{V_{spa}^0 (1 + K_{exp}(2P_{spa} - P_0))} \quad (2.7)$$

For fully blocked conditions, we can assume that the SPA is prevented from expanding, in which case we can assume $K_{exp} = 0$. The general case with the SPA interacting with its environment is discussed in Chapter 4. In both these cases, the SPA internal volume is less than or equal to that in free expansion. Therefore, it is observed that the pressure response will be the slowest for free expansion and fastest for fully blocked conditions.

2.2.3 Normalization

We normalize soft actuator and PSS pressure dynamics with soft actuator internal volume and the equivalent sonic conductance. We first define normalized sonic conductance as:

$$\bar{C} = \frac{C_{eq}}{V_{spa}^0} \quad (2.8)$$

For *constant flow* PSSs, we additionally define normalized reservoir volume, \bar{V} , and compressor

output flow, \bar{Q} :

$$\bar{V} = \frac{V_{res}}{V_{spa}^0}, \quad \bar{Q} = \frac{Q_{com}}{V_{spa}^0} \quad (2.9)$$

Next, we normalize soft actuator pressure dynamics by \bar{c} as:

$$\dot{P}_{spa}|_{Infl} = \left(\frac{P_0 \Psi_{Inf} P_{src}}{1 + K_{exp}(2P_{spa} - P_0)} \right) \bar{c} \quad (2.10)$$

$$\dot{P}_{spa}|_{Defl} = \left(\frac{-P_0 \Psi_{Def} P_{spa}}{1 + K_{exp}(2P_{spa} - P_0)} \right) \bar{c} \quad (2.11)$$

where Ψ_{Inf} and Ψ_{Def} correspond to the flow function, Ψ , during inflation and deflation respectively.

For *constant pressure PSSs*,

$$\dot{P}_{src} = 0 \quad (2.12)$$

And for *constant flow PSSs*, the normalized *source* pressure dynamics are given by:

$$\dot{P}_{src} = \left(\frac{P_0}{\bar{V}} (\bar{Q}/\bar{c} - \Psi_{Inf} P_{src}) \right) \bar{c} \quad (2.13)$$

Using the above, the normalized soft actuator pressure dynamics are given by Eq. 2.3, 2.4, 2.10, 2.11, 2.12, and 2.13. For *constant pressure PSSs*, the normalized dynamics depend on P_{src} , P_{spa} , K_{exp} and b_{eq} ; whereas for *constant flow PSSs*, they additionally depend on \bar{Q} and \bar{V} . The effect of V_{spa}^0 and \bar{c} is seen as scaling of the dynamics in magnitude and time respectively.

2.3 Simulation study

Here, we simulate the normalized soft actuator pressure dynamics and use the predicted pressure response to quantify the relationship between dynamic performance and different properties of the PSS and SPA. We then validate these simulation results by measuring the inflation and deflation response of a pneunet actuator [10] in different operating conditions.

We first identify critical parameters of these PSS components affecting pneumatic flow, and classify them into two types as follows:

- **flow parameters, f :** These include non-varying pneumatic parameters such as internal volumes of reservoir, tubing and fittings; and flow capacities of regulators, valves, compressors, tubing and fittings. These parameters form a discrete set of values.
- **control parameters, c :** These include actively controlled parameters such as *source*

Chapter 2. Modelling and parametric study of pneumatic supply systems

pressure, and duty cycles of compressor and valves; which can take continuously varying values.

Next, we identify the soft actuator design parameters affecting its pressure dynamics, and denote them as α : operating pressure, volume and extent of deformation. Table 2.1 lists the flow, control and soft actuator design parameters considered for this simulation study.

Table 2.1: Considered parameters of SPA and PSS

Classification	Symbol	Description
f	PSS flow parameters	C_{eq} Equivalent sonic conductance b_{eq} Equivalent critical ratio Q_{com} Compressor flow output * V_{res} Reservoir volume *
c	PSS control parameters	P_{src} Source Pressure D_V Valve duty cycle D_C Compressor duty cycle *
α	soft actuator design parameters	P_{op} Operating pressure V_{spa}^0 Internal volume K_{exp} Expansion ratio

*only applicable for configuration B

Lastly, we define soft actuator dynamic performance using the following metrics:

- T_{fall} : Time required for P_{spa} to drop from 98 - 2% of P_{op}^g
- T_{rise} : Time required for P_{spa} to rise from 2 - 98% of P_{op}^g
- f_{max} : Maximum frequency at which soft actuator can be cyclically inflated and deflated between 2% and 98% of P_{op}^g

where P_{op}^g is the soft actuator operating pressure, P_{op} , expressed in gauge ($P_{op}^g = P_{op} - P_0$); and $P_0 \leq P_{spa} \leq P_{op}$.

2.3.1 Methods

1. **Fall time and rise time:** We simulated soft actuator pressure response of inflation and deflation between 0 - 0.2 MPaG, through a flow path of $\bar{c} = 10 V_{spa}^0/s/MPa$. We carried out the simulations at a sampling rate of 10 kHz, for the following set of parameters:

- Source pressure, P_{src} : 0.2-0.6 MPaG, in steps of 0.025 MPa
- Expansion ratio, K_{exp} : 0-15 V_{spa}^0/MPa , in steps of 0.5 V_{spa}^0/MPa

- (c) Critical ratio, b_{eq} : 0.1-1, in steps of 0.1

For *constant flow* PSSs, we further carried out simulations for:

- d) Normalized compressor flow, \bar{Q}/\bar{C} : 0.025-0.25 MPa in steps of 0.025 MPa
e) Normalized reservoir volume, \bar{v} : In five values ranging from 0.1-24 V_{spa}^0 , as shown in Fig. 2.5. $\bar{v} = 0.1$ represents *constant flow* PSSs without a reservoir. We chose this small but non-zero value to account for internal dead volume of tubing and fittings.

By linear interpolation of the pressure response data, we calculated T_{fall} and T_{rise} for different operating pressures, P_{op} : 0.005-0.2 MPaG, in steps of 0.005 MPa.

2. Maximum actuation frequency: For *constant pressure* PSSs, we calculated f_{max} by using results from T_{fall} and T_{rise} . For *constant flow* PSSs, we used the principle of conservation of mass to calculate f_{max} .

2.3.2 Results

1. Fall time, T_{fall} : As air flows from the soft actuator to the ambient, soft actuator pressure dynamics do not depend on the type of *source*, i.e. they are unaffected by P_{src} , \bar{Q} , \bar{v} and D_C . T_{fall} for different P_{op} , K_{exp} and b_{eq} are shown in Fig. 2.3. The labels depict the fall time scaled by \bar{C} . As seen from the figure, *fall time* increases with increasing P_{op} and K_{exp} and decreases with b_{eq} and \bar{C} .

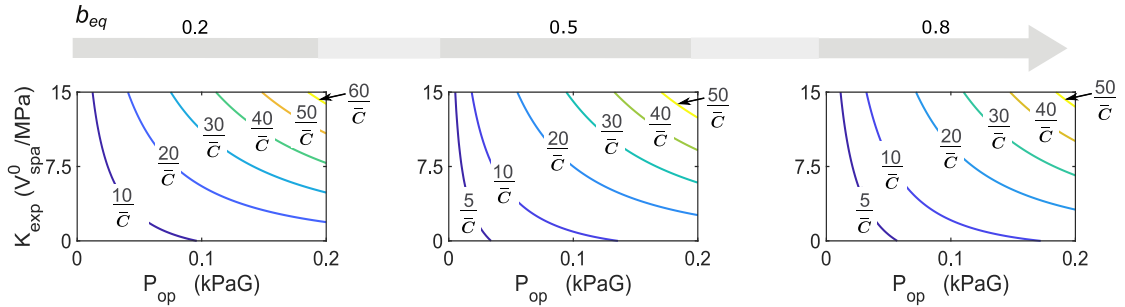


Figure 2.3: Fall time, T_{fall} at varying values of actuator operating pressure, P_{op} , expansion ratio, K_{exp} , and equivalent critical pressure ratio, b_{eq} . An axis of increasing b_{eq} is displayed showing the nature of K_{exp} vs. P_{op} vs. T_{fall} for three values of b_{eq} . The fall time in seconds is given by the labels on the contour lines, with \bar{C} expressed in $V_{spa}^0/s/MPa$. We observe that T_{fall} increases with P_{op} and K_{exp} and decreases with \bar{C} and b_{eq} .

2. Rise time, T_{rise} : As air flows from the *source* to the soft actuator, *constant pressure* PSSs and *constant flow* PSSs exhibit different behaviour.

- (a) **Constant pressure PSSs:** During inflation, a higher *source* pressure leads to higher flow in the PSS and therefore, a faster response. Fig. 2.4 shows rise time for different P_{src} , K_{exp} , b_{eq} and P_{op} . The labels on each curve depict the rise time scaled by \bar{C} . As seen from the

figures, T_{rise} increases with increasing operating pressure, P_{op} , expansion ratio, K_{exp} and decreases with source pressure, P_{src} , normalized conductance, \bar{c} and critical ratio, b_{eq} .

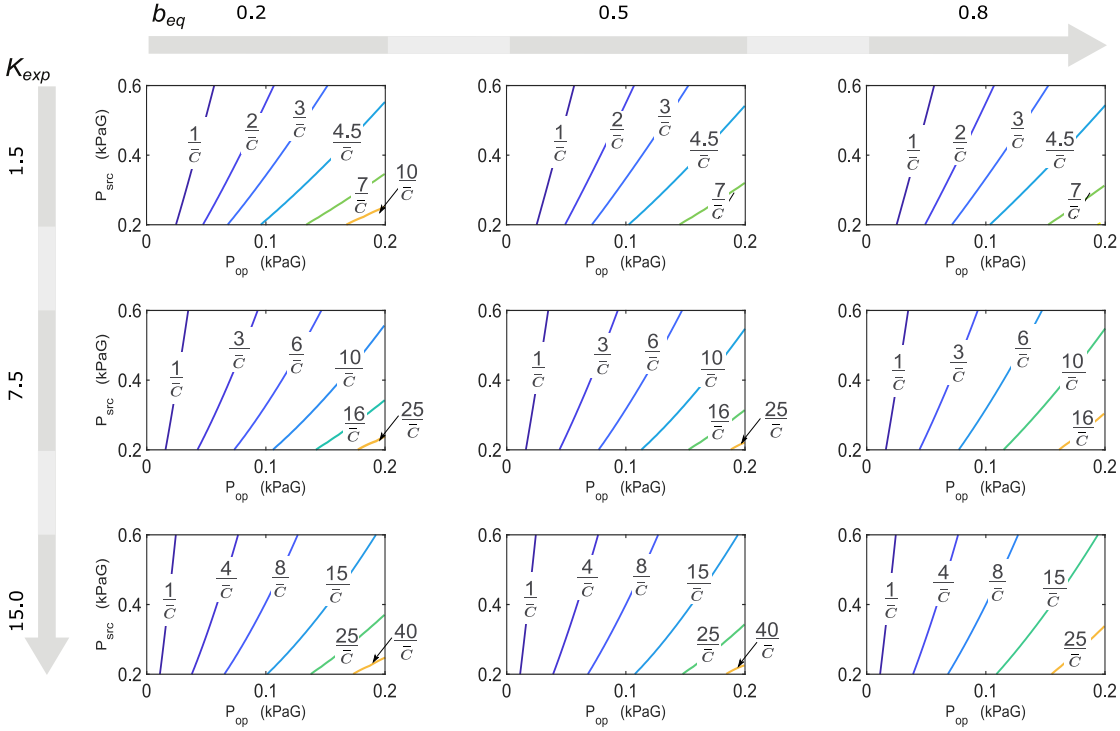


Figure 2.4: Rise time, T_{rise} for *constant pressure* PSSs at varying values of actuator operating pressure, P_{op} , source pressure, P_{src} , expansion ratio, K_{exp} and equivalent critical pressure ratio, b_{eq} . Two axes of increasing b_{eq} , and K_{exp} are displayed showing the nature of P_{src} vs. P_{op} vs. T_{rise} for three values each of b_{eq} , and K_{exp} . The rise time in seconds is given by the labels on the contour lines, with \bar{c} expressed in $V_{spa}^0/s/MPa$. We observe that T_{rise} increases with P_{op} and K_{exp} and decreases with P_{src} , \bar{c} and b_{eq} .

- (b) **Constant flow PSSs:** During inflation, air flows from the reservoir to the actuator, leading to a reduction in reservoir pressure, P_{src} . Here, the reservoir acts similar to a large capacitor. Therefore, for a large reservoir ($\bar{v} \gg 1$), the drop in P_{src} is small, leading to almost constant source pressure conditions. This can be seen in Fig. 2.5 where T_{rise} for *constant flow* PSSs is similar to that of *constant pressure* PSSs (dotted curve), for certain pressures and reservoir volumes. Thus, the reservoir permits rapid bursts of flow to the soft actuator, and can compensate for small compressors with low flow capacity \bar{Q} . However, this is valid only for intermittent operation, as the flow to the soft actuator has to be replenished by the compressor. We see this in Fig. 2.5, where at some values of P_{src} and \bar{v} , T_{rise} increases significantly. This occurs when P_{src} drops below P_{op} during inflation, and therefore, the compressor has to pressurize both reservoir and actuator. The point at which this occurs can be found using Fig. 2.5, or alternatively, by using conservation of mass, as described below.

Soft actuator pressure and normalized volume before inflation is P_0 and 1 respectively. After inflation, they become P_{op} and $1 + K_{exp}(P_{op} - P_0)$. For the reservoir with volume \bar{v} , let pressure before and after inflation be P_{src} and P'_{src} respectively. The air entering through

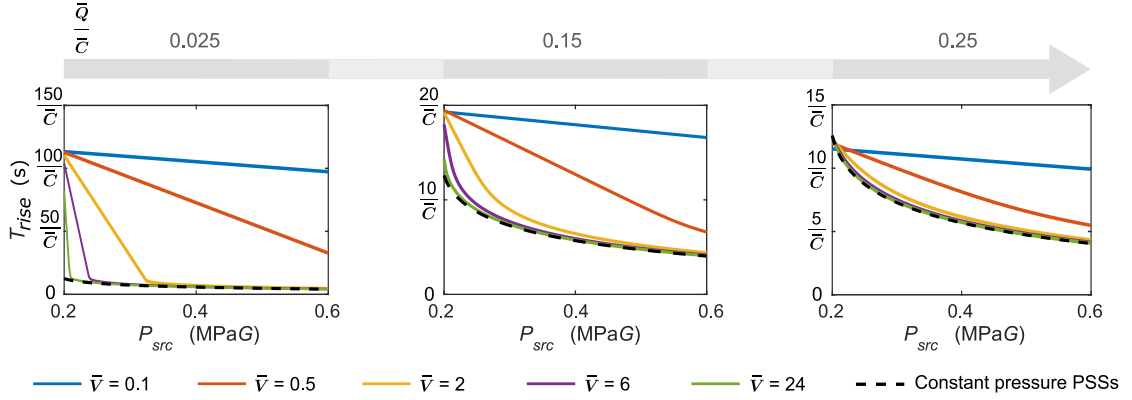


Figure 2.5: Rise time, T_{rise} , for *constant flow* PSSs at varying values of *source* pressure, P_{src} , compressor flow output, \bar{Q} and reservoir volumes, \bar{v} , for $P_{op} = 0.2 \text{ MPaG}$, $K_{exp} = 1.51 V_{spa}^0 / \text{MPa}$ and $b_{eq} = 0.49$. An axis of increasing \bar{Q}/\bar{C} is displayed showing the nature of P_{src} vs. T_{rise} for three values of \bar{Q}/\bar{C} . The rise time in seconds is given by the labels on the Y-axis, with \bar{C} expressed in $V_{spa}^0 / \text{s/MPa}$. We observe that T_{rise} for *constant flow* PSSs is very close to that of *constant pressure* PSSs (dashed curve), for certain values of P_{src} and \bar{v} . This is because the pressure in the reservoir does not vary much during inflation, leading to a quasi-constant pressure. However, at other values of P_{src} and \bar{v} , T_{rise} is substantially higher. This occurs when P_{src} drops below P_{spa} , and the compressor has to pressurize both, reservoir and soft actuator. The transition point at which this occurs can be found using the figure, or from Eq. 2.14.

the compressor is $P_0 \bar{Q} T_{rise}$. In the limiting condition, P_{src} drops to P_{op} , i.e., $P'_{src} = P_{op}$. Let T^* be the rise time for *constant pressure* PSSs at the same P_{src} . The condition that P_{src} in a *constant flow* PSS does not drop below P_{op} during inflation is then given by:

$$P_{src} \bar{v} + P_0 \bar{Q} T^* + P_0 > P_{op} (\bar{v} + 1 + K_{exp} (P_{op} - P_0)) \quad (2.14)$$

As the average P_{src} in *constant flow* PSSs is always lower than that in *constant pressure* PSSs, $T_{rise} > T^*$. Hence, if the above condition is satisfied, it is always ensured that P_{src} after inflation does not drop below P_{op} , and therefore, T_{rise} will be similar to that of *constant pressure* PSSs. However, if Eq. 2.14 is not satisfied, T_{rise} increases greatly.

3. Maximum actuation frequency, f_{max} :

- (a) **Constant Pressure PSSs:** We used T_{rise} and T_{fall} to calculate f_{max} for different sets of P_{src} , K_{exp} , b_{eq} and P_{op} . This frequency is given by,

$$f_{max} = \frac{1}{T_{rise} + T_{fall}} \text{ Hz} = \frac{1}{T_{cycle}} \text{ Hz} \quad (2.15)$$

From Eq. 2.15 and Figs. 2.3 and 2.4, we see that f_{max} increases with P_{src} , b_{eq} and \bar{C} and decreases with P_{op} and K_{exp} . In order to achieve cyclic actuation, the valve must be controlled in a repeating and alternating pattern to inflate and deflate the actuator. The ratio of ON time to the OFF time is the valve duty cycle D_V (more rigorous definition

described in Section A4). To achieve f_{max} given by 2.15, the D_V required is given by:

$$D_V = \frac{T_{rise}}{T_{Cycle}} \times 100\% \quad (2.16)$$

At any frequency higher than that in Eq. 2.15, the amplitude of pressure oscillation will reduce. Additionally, at f_{max} , duty cycles other than that in Eq. 2.16 will either lead to overpressure, or reduce the pressure amplitude.

- (b) **Constant Flow PSSs:** In *constant flow PSSs*, as the source pressure, P_{src} is not constant, f_{max} cannot be calculated directly from T_{fall} and T_{rise} . While fast inflation can be achieved in intermittent operation, continuous cyclic actuation may not be sustained at the same speed as the compressor may not be able to replenish the air consumed. As P_{src} drops, T_{rise} will increase and the actuation frequency will reduce. However, after a while, steady state will be reached such that T_{rise} does not increase further. At the steady state, f_{max} can be found by applying conservation of mass to the air entering (through the compressor) and leaving (from the soft actuator) the system.

Soft actuator pressure and normalized volume before inflation is P_0 and 1 respectively. After inflation, they increase to P_{op} and $(1 + K_{exp}(P_{op} - P_0))$ respectively. The amount of air entering the system during one actuation cycle is $P_0 \bar{Q} T_{Cycle} D_C$, where D_C is the compressor duty cycle. By mass conservation, we have,

$$P_0 + P_0 \bar{Q} D_C T_{Cycle} = P_{op}(1 + K_{exp}(P_{op} - P_0)) \quad (2.17)$$

Rearranging,

$$f_{max} = \frac{1}{T_{Cycle}} = \frac{P_0 \bar{Q} D_C}{(P_{op} - P_0)(1 + P_{op} K_{exp})} \quad (2.18)$$

If the system reaches steady state, Eq. 2.18 predicts the sustainable f_{max} for any compressor based PSS powering any soft actuator, with a simple arithmetic expression containing only 3 terms: normalized average compressor flow, soft actuator operating pressure, and expansion ratio; irrespective of the other variables. Using $D_C = 1$ gives the theoretically maximum sustainable f_{max} for a compressor-based PSS.

In order to achieve this f_{max} , \bar{c} should be sufficiently large to allow the desired flow rate, and D_V should be chosen appropriately to allow sufficient time for complete inflation and deflation. This condition is given by,

$$D_V \geq \frac{T^*}{T_{Cycle}} \times 100\%; \quad D_V \leq 1 - \frac{T_{fall}}{T_{Cycle}} \times 100\% \quad (2.19)$$

where T^* is the rise time for *constant pressure PSSs* at the same initial P_{src} .

If the normalized conductance, \bar{c} , is insufficient to provide the desired flow rate, either one or both conditions in the above equation will not be satisfied, giving an infeasible solution. In such a case, the steady state will not be reached, and the only solution to achieving the theoretically maximum f_{max} would be to increase \bar{c} .

For both types of PSSs, the air consumed per actuation cycle in standard L is given by (Section A5):

$$Air\ Consumed = (P_{op} - P_0) (1 + P_{op} K_{exp}) V_{spa}^0 \quad (2.20)$$

2.3.3 Validation

To validate the results from this simulation study, we powered a single pneunet actuator [10] with a pressure regulated PSS (Fig. 2.2A), and compared the T_{fall} , T_{rise} , f_{max} , and the inflation and deflation response with that predicted by the model. The PSS consisted of an external regulated pressure source, a solenoid valve (SMC VV100 series) and tubing (SMC OD: 4mm, ID: 2.5mm, length: 0.84m between source and valve, 0.46m between valve and pneunet). We measured the pressure response using a pressure sensor (MPX5500DP), and used two flow sensors (AWM5000 Series) to measure flow inlet and outlet to the pneunet. The inflation and deflation response at seven different source pressures (0.1 MPaG, 0.15 MPaG, ..., 0.4 MPaG) were measured, ten times each. We then simulated the pressure response in MATLAB to compare the results with our model by using the following parameters:

1. Actuator volume, $V_{spa}^0 = 0.0167L$, was calculated by adding the dead volume of tubing to the pneunet internal volume, obtained from CAD.
2. Operating pressure, $P_{op} = 0.1$ MPaG.
3. Expansion ratio, $K_{exp} = 8.25 V_{spa}^0 / \text{MPa}$, was calculated by measuring the amount of air consumed in one actuation cycle, and using Eq. 2.20.
4. Normalized conductance and critical ratio, $\bar{c} = 17.98 V_{spa}^0 / \text{s/MPa}$, $b_{eq} = 0.19$ for inflation and $\bar{c} = 26.04 V_{spa}^0 / \text{s/MPa}$, $b_{eq} = 0.29$ for deflation. These were found by using the sonic conductance and critical ratio of the valve from its datasheet, then calculating equivalent conductance of tubing and valve using Eq. A17 to A22, and finally normalizing with actuator volume V_{spa}^0 .
5. Source pressure, $P_{src} = 0.1, 0.15, \dots, 0.4$ MPaG.

Figure 2.6B, C show the pressure response and Table A1 shows the rms and peak errors between experiments and the model. Additionally, Table A2 compares the predicted vs. achieved fall time, rise time and maximum actuation frequencies. We see that the model closely captures the behaviour of the pneunet with less than 5.2% rms error for all conditions. We also see that with higher source pressures, the measured inflation response is faster than the one predicted by the model. This is because the inertia of the soft actuator limits the peak displacement at high actuation speeds, which leads to a smaller actuation volume and faster response.

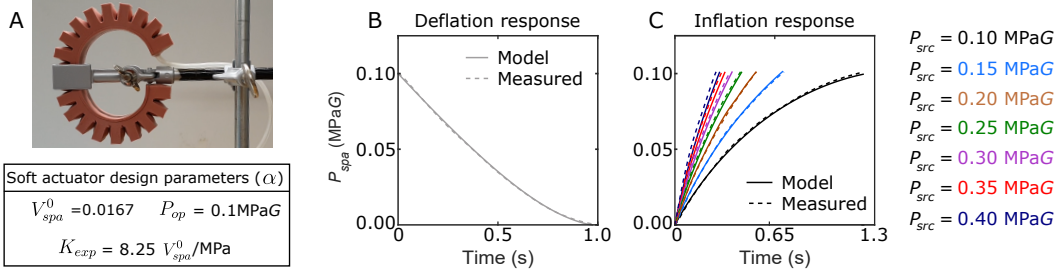


Figure 2.6: Validation of results from the PSS parameter study by testing the inflation and deflation response with a pneunet actuator (A) the pneunet used for testing. (B) comparison of simulations (continuous line) with mean measured pressure response (dotted line) in deflation. (C) comparison of simulations (continuous line) with mean measured pressure response (dotted line) in inflation. The different coloured lines correspond to different source pressures (P_{src}) during testing.

2.4 Practical considerations in PSS modelling and design

In the previous section, we modelled the pressure and flow dynamics of SPAs, studied the effect of ten model parameters. However, it largely consisted of numerical simulations of the model, with experimental validation with just a single pneunet-type actuator in a few test conditions. Also, the effect of *valve*, *tubing*, and *fittings* was lumped together and normalized with respect to SPA size. These results, therefore, do not give a tangible understanding of the effect of parameters such as *valve flow capacity*, *tubing size*, or type of *fittings* used. Furthermore, it was assumed that values of all component parameters are known, and that the valves perform perfectly without delays.

In this section, we conduct experimental validation of the presented model, and address some practical considerations such as valve delays and characterizing pressure-flow relationship for a given component. From the simulation results in the previous section, we saw that constant pressure and constant flow PSSs behave the same as long as the reservoir has sufficient volume and initial source pressure. With this knowledge, we choose to study the following five parameters, which we believe are the most critical in understanding SPA dependency on PSS: *SPA size*, *tubing length*, *tubing diameter*, *source pressure*, and *valve conductance*. The general effect of these parameters is shown in Table 2.2. The above relations are straightforward for most parameters: an increase in source pressure would increase f_{max} , or that increasing valve conductance would lead to higher flow and hence f_{max} , and so on. The relation for tubing diameter, however, is not so simple. As D increases, the flow resistance decreases, meaning that there would be more flow through the PSS, indicating a faster response. However, the amount of air required also increases, slowing down the overall response. As a result, it is difficult to predict just by looking at the values how changing D would affect f_{max} , which is why we denote its effect using a \uparrow sign. To better understand these effects and quantify them, we conduct additional numerical simulations and experimental testing in 162 test conditions spanning distinct parameter combinations to validate the simulation results over an extensive range of widely used PSS components and SPAs.

Table 2.2: Different parameters considered

Parameter	f_{max}
Source pressure, P_{src}	↑
Valve conductance, C_{valve}	↑
Tubing diameter, D	↑↓
Tubing length, L	↓
SPA volumes, V_0, V_{op}	↓

2.4.1 Defining parameter range and simulating pressure dynamics

We modelled Eq. 2.1 to 2.7 in MATLAB, and solved them to simulate SPA pressure response from P_0 to $P_{op} = 50$ kPaG. While we chose an operating pressure of 50 kPaG, the presented methods can be repeated for any other value. In order to study the effect of the different parameters, we carried out the simulations while varying the values of the parameters defined in Table 2.2. The different parameter values during simulations were selected to span across a wide range of commonly used components in soft robotics. Similarly, the three SPAs modelled were of three sizes, large, medium and small, so as to represent and encompass currently existing designs.

SPA size: We considered three SPAs of different sizes as shown in Fig. 2.7B and as described below:

1. *SPA-pack*, consists of four fibre-reinforced cylindrical extending SPAs, held together in a soft silicone matrix. Using its CAD models at deflated and inflated states, we calculated its internal volumes: $V_0 = 57$ mL at P_0 , and $V_{op} = 60$ mL at $P_{op} = 50$ kPaG.
2. *Pneunet*, is one of the widely used bending SPAs. Its internal volumes are $V_0 = 3.2$ mL at P_0 , and $V_{op} = 10.7$ mL when fully bent at $P_{op} = 50$ kPaG, as reported in Mosadegh et al. [10]. We also independently verified these values by injecting water into the pneunet with a syringe, and measuring the volume of water required to completely fill it up and inflate.
3. *SPA-skin*, is a low-profile SPA, used for vibrotactile feedback [39; 100]. It is constructed by introducing an air gap between two layers of silicone and forms an approximately hemispherical shape when inflated. Its internal volumes are $V_0 = 0.1$ mL, and $V_{op} = 0.5$ mL at $P_{op} = 50$ kPaG, which we calculated using CAD models at deflated and inflated states of the SPA-skin.

Tubing: We considered three values of tubing length $L = 1, 2$ and 5 m; and 25 linearly increasing values of tubing diameter from $D=2$ mm to 5 mm (resolution 0.125 mm). For connecting these different tubing to the SPAs and valves, there are two main type of fittings: barbed type and

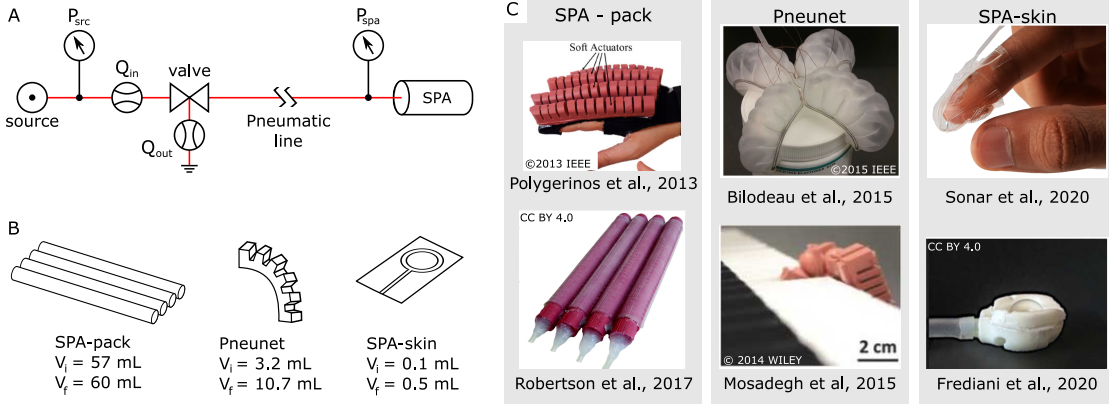


Figure 2.7: Flow-path optimization of SPAs. (A) Schematic of the experimental setup for powering the SPAs. We use an external regulated *source*, and standard commercial *valve* and *tubing*. We measure pressure at the *source* and SPA using pressure sensors, and the in-flow and out-flow using flow sensors. (B) Three generic SPAs: SPA-pack [60; 7], fast pneunet actuator [10; 101], and SPA-skin [100; 39; 102], with different volume ranges and application requirements to evaluate the optimization model. (C) Examples of SPAs in literature, comparable to those tested in this study. They are used in applications ranging from wearable haptic devices [39; 100; 102] to grippers [101] or manipulators [10; 103]

push-in type. The former connect from the inside of the tubing and have a smaller diameter than that of the tubing. The push-in type fittings on the other hand, connect from outside the tubing and have a larger diameter. From their technical manuals, we also found that the sonic conductances of these fittings were over an order of magnitude above that of the tubing used, therefore leading to a negligible effect on equivalent sonic conductance. For this reason, we used push-in type fittings in this study.

Source pressure: We considered three values of $P_{src} = 60, 80$ and 100 kPaG , and assume that these values stay constant during actuation. For the limiting case where the source cannot provide the necessary flow, f_{max} can be calculated using conservation of air mass as described in Eq. 2.18 .

Valve conductance: We considered the following two valves: SMC VZ100 series (Valve 1) and Festo MH3 series (Valve 2). We model their flow output using the ISO6358 standard in Eq. 2.4. The parameter values, C and b for these valves were calculated by experimental characterization, as explained in section 2.4.2 Fig. 2.8 and Table 2.3.

For each parameter combination above, we first calculated C_{eq} and b_{eq} using the C and b of each component, viz., *valve*, *tubing* and *fittings*, and simulated the inflation and deflation response between 0 and 50 kPaG using a standard numerical solver, *ode45*, in MATLAB. For the SPAs used here, the SPA volume almost linearly increases with pressure [10]. Therefore, we modelled the SPA volume using a simple linear relationship between $V_0 + V_{tube}$ at P_0 to $V_{op} + V_{tube}$ at P_{op} as described in Eq. 2.6. For modelling a general non-linear pressure-volume behaviour, the expressions described in Section A3 can be used. Using the simulated pressure response in inflation and deflation, we calculated the maximum actuation frequency as: $f_{max} = (T_{rise} + T_{fall})^{-1}$, where T_{rise} and T_{fall} are rise time and fall time of the SPA pres-

sure from 2% to 98% and 98% to 2% respectively, of P_{op} . Similarly, we calculated the air consumption, A , and energy consumption, E , using Eq. A29 and A30 respectively.

2.4.2 Experimental testing

We tested three SPAs described in Fig. 2.7B to validate our simulation results from the model. For all parameters except tubing diameter, we chose the same values as those for the simulations. For the diameter, we chose three sizes: 2.5, 3 and 4 mm, based on commonly used commercially available options. This led to a total of 162 testing conditions with 3 SPA types, 3 source pressures, 3 tubing lengths, 3 tubing diameters, and 2 valves. The experimental setup (Fig. 2.7A) consisted of an external regulated pressure source, a solenoid valve (Valve 1 or 2), the SPA (SPA-pack, pneunet or SPA-skin) and tubing ($L = 1, 2$ or 5 m; $D = 2.5, 3$ or 4 mm). We use two flow sensors (Honeywell Zephyr series) to measure the inflow and outflow, and pressure sensors (Honeywell HSC series) for measuring source pressure, and SPA pressure. We used a microcontroller (Teensy 4.1) to read all sensor values at 1 kHz and control the valves to inflate or deflate the SPA.

Prior to testing, we characterized the two valves used. This was necessary, as the C and b values for Valve 2 were not available in the technical datasheet, and those from Valve 1 did not match measured flow. We connected the valves to the source and measured the valve flow through the inflation (source to SPA) and deflation (SPA to ambient) paths, while varying the source pressure. While doing so, we placed pressure sensors right at the inlet and outlet of the valves to measure the pressure drop across only the valve. Using a non-linear least squares solver, 'lsqcurvefit' in MATLAB, we fit the measured pressure and flow data to ISO 6358 parameters C and b for the two valves in inflation and deflation. Fig. 2.8 shows the fitted model vs. measured flow through the valve and Table 2.3 shows the root mean squared errors ($RMSE$) between the two. This method can be readily applied to any other PSS component to characterize the flow vs. pressure relationship.

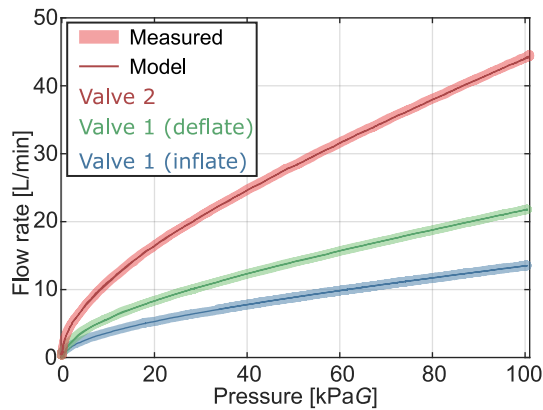


Figure 2.8: Experimental characterization of the valves used. We connected the valves to a source, varied the pressure, and measured the flow through their inflation and deflation paths. Using a non-linear solver, we fitted the measured flow to the ISO 6358 model [84; 85] shown in Eq. 2.4.

Table 2.3: ISO 6358 parameters and rmse for Valves 1 and 2

Valve path	C [lpm/kPaG]	b	$RMSE$ [lpm]
Valve 1 - Inflation	7.8×10^{-2}	0.197	0.1
Valve 1 - Deflation	12.4×10^{-2}	0.04	0.17
Valve 2 - Inflation/deflation	25.3×10^{-2}	0	0.30

We connected the various options of the SPA and PSS, and tested them in the 162 distinct combinations as described earlier. For every testing condition, lasting 10 s each, the micro-controller controlled the valve state to cyclically inflate and deflate the SPA between 1 and 49 kPaG. Initially, we used a simple control algorithm, that changes the valve state when the SPA pressure reaches one of its two limits. However, this led to over-pressure, especially for the SPA-skin reaching up to 80 kPaG when powered at $P_{src} = 100$ kPaG. This occurred because the response time of the valve introduced a delay in the system. In addition to reducing f_{max} and increasing A and E , over-pressure could cause failure via bursting of the SPA. To address this, we modified the control algorithm to compensate for the valve delay as follows:

$$\begin{aligned}
 & \text{if}(P_{spa} + \dot{P}_{spa} \cdot d > 49 \text{ kPaG} \& \text{input} == 1) \\
 & \quad \text{input} = 0; \\
 & \text{else if}(P_{spa} + \dot{P}_{spa} \cdot d < 1 \text{ kPaG} \& \text{input} == 0) \\
 & \quad \text{input} = 1;
 \end{aligned}$$

where, d is the delay due to valve response time. This modified control strategy uses the known value of valve delay, predicts when the SPA will reach its target, and pre-emptively switches the valve ON or OFF to prevent over-pressure. We calculated this value using the time-lag in the applied signal and measured pressure response, equal to 25 ms and 8 ms for Valve 1 in deflation and inflation respectively and 3 ms for Valve 2. Fig. 2.9 shows the effect of this delay compensation strategy for the SPA-skin. As seen from the figure, this led to a 60% increase in f_{max} from 6 Hz to 9.6 Hz.

2.4.3 Results

Here, we analyse the results from our simulations and experiments, and compare them to evaluate the accuracy of the model. Fig. 2.10A and B compare the measured f_{max} to that from simulations for a tubing length of 1 m and 5 m respectively. Our model accurately captures the behaviour of f_{max} for the different SPAs at varying tubing lengths, diameters, P_{src} and valves, with the exceptions of pneunet and SPA-skin (Valve 1 only) at 1m tubing length. For the SPA-skin with 1m tubing, the small pressurized volume led to small rise and fall times, which were lesser than the valve delay of Valve 1. This led to over-pressurization and therefore lower f_{max} than that predicted by simulations.

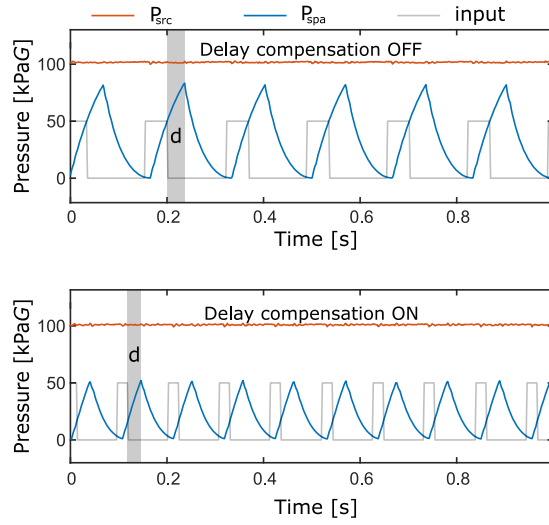


Figure 2.9: Comparison of SPA-skin pressure response with and without delay compensation. Without delay compensation, the SPA-skin is over-pressurized up to 80 kPaG which is not only slower, but also harmful for the SPA. With delay compensation, the valve is switched pre-emptively, predicting when the SPA will reach its target. This increased the SPA-skin f_{max} from 6 Hz to 9.6 Hz and reduced A from 6.2 mL to 3.8 mL.

For the pneunet, the discrepancy can be attributed to inertial and viscoelastic effects. In our study, we assumed a static relation between the SPA pressure (input) and its quasi-static displacement (output). In practice, however, the displacement of the SPA are also affected by dynamic effects including its viscoelastic and inertial properties. With increasing actuation frequency, the effects due to viscoelasticity and inertia increase with orders of 1 and 2 respectively, similar to a spring-mass-damper system. While the static pressure-displacement assumption holds well at low frequencies, the viscoelastic and inertial effects start to dominate the displacement dynamics at higher frequencies leading to discrepancies between the predicted and observed displacement. In case of the pneunet, the actuator underwent complete oscillations from a straight configuration to a bent configuration at low actuation frequencies (<4 Hz). At higher frequencies, however, as the inertial and viscoelastic effects began to dominate the dynamics, the pneunet could not completely bend as expected and started oscillating at a partially expanded/bent state between fully expanded and deflated states. This led to a mismatch between the modelled values of V_0 and V_{op} , and eventually the deviation from predicted response. These two oscillation modes can be seen in Supplementary video 3, where, for a tubing length of 2m, we see the transition between normal and abnormal oscillations.

These results suggest that at high frequencies, the inertial and viscoelastic dynamics or valve delays can play a major role in determining the overall SPA behaviour, and therefore must be considered in future studies to predict the SPA dynamics more accurately.

We can also see that the data matches the trends predicted in Table 2.2. As expected, f_{max}

increases with P_{src} and valve conductance, and decreases with SPA size and tubing length. The fastest response, with 44 Hz was observed for the following parameter combination: SPA-skin, Valve 2, tubing length and diameter of 1 m and 2.5 mm respectively and P_{src} of 100 kPaG. This is logical as a lesser amount of air is required for powering a smaller SPA. Conversely, we see a reduction in f_{max} with increase in tubing length, due to increased V_{spa} . The relative difference in f_{max} between 1 m and 5 m tubing is more substantial for the smaller SPA-skin, as a much larger proportion of V_{spa} is due to the tubing.

As opposed to other parameters, the tubing diameter shows an interesting trend as seen from Fig. 2.10. We see that there is a unique diameter for a given set of SPA, valve and tubing length, that gives the fastest response. This diameter, with largest f_{max} , increases with SPA size and

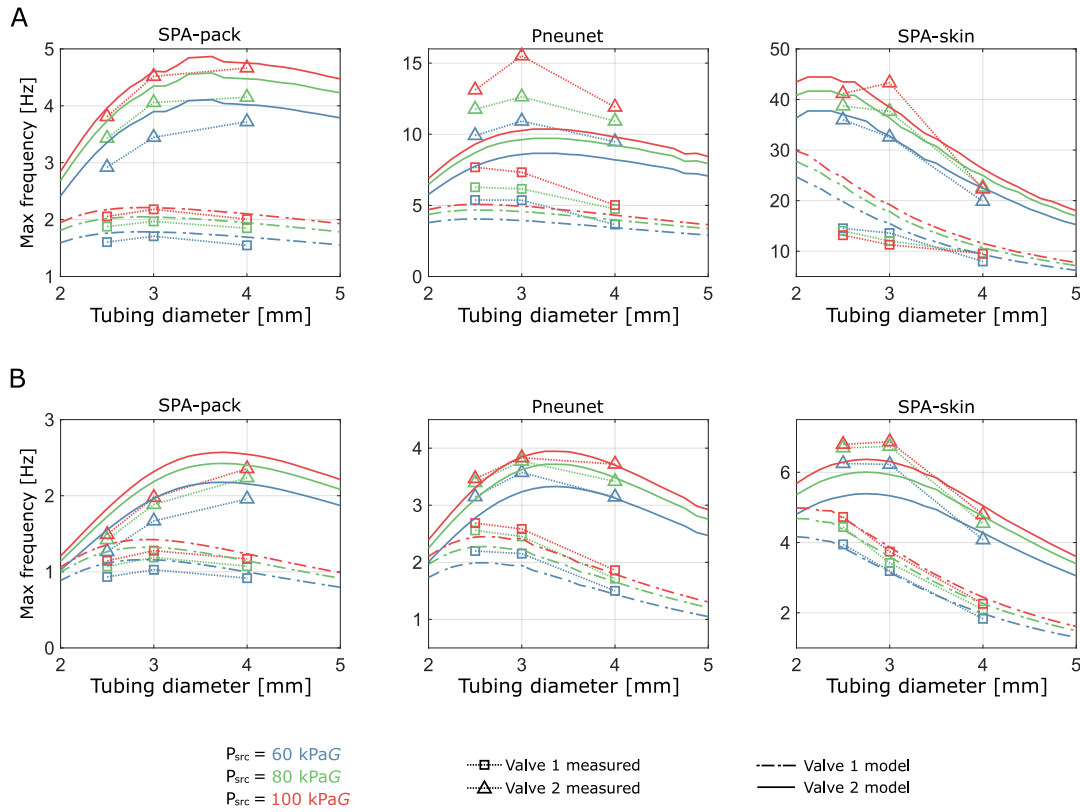


Figure 2.10: Comparison of predicted vs. measured values of the maximum actuation frequencies, f_{max} , for the SPA-pack, pneunet and SPA-skin, for (A) Tubing length = 1 m, and (B) Tubing length = 5 m. We observe that f_{max} increases with valve conductance and source pressure, and reduces with SPA size and tubing length. For the tubing diameter, interestingly, we find the existence of a value with the largest f_{max} , such that f_{max} reduces above or below this value of D . Furthermore, this diameter changes with the SPA size, valve conductance and tubing length. For instance, at tubing length of 1m, it is 3 and 4 mm for the SPA-pack, whereas it is 2.5 and 3 mm for the pneunet for valve 1 and 2 respectively. At tubing length of 5 m the optimal diameters are slightly higher. Another observation is that while f_{max} is expected to reduce with L , the reduction is significantly higher for the SPA-skin, followed by the pneunet and least for the SPA-pack. This occurs because of the relative size differences between the three SPAs.

valve conductance. For example, for the SPA-pack, this diameter is 3 mm for valve 1 and 4 mm for valve 2. Similarly, for the pneunet, it is 2.5 mm for valve 1 and 3 mm for valve 2. For SPA-skin, the tubing with 2.5 mm diameter has highest f_{max} for all conditions. This curious trend shows that to achieve the highest actuation frequency, the tubing diameter must be selected carefully depending on the valve used, tubing length and SPA size.

2.5 Discussion

To design any mechanical system, it is critical to understand the full system behaviour comprehensively from the power source to the end effector. While it is standard practice for many classical robotic systems, soft robotics has not seen a system-wide understanding or modelling of the impact of individual components on the soft actuator mechanical performance. In this chapter, we addressed this knowledge gap to create a direct relationship between properties of the SPA and PSS and dynamic performance metrics. We first introduced a comprehensive model for SPA pressure and flow dynamics that can be directly adopted to most existing systems. Using this model, we conducted a simulation study where we investigated and quantified the effect of ten parameters on soft actuator dynamic performance. This mapping creates an improved understanding of the role of *source*, *valve*, *pneumatic line* and soft actuator design parameters on dynamic performance. Next, we experimentally validated our model predictions in 162 unique testing conditions obtained through combinations of five critical parameters. While doing so, we addressed practical considerations such as valve delay compensation and PSS component flow characterization. The model predictions were able to capture the SPA behaviour accurately, predicting the relation of f_{max} with SPA and tubing size, valve conductance and source pressure. An interesting trend was found with the tubing diameter such that a unique optimal value exists, which maximizes f_{max} . These results provide meaningful insights about the dependency of SPA dynamic performance on PSS and SPA properties going beyond the scope of currently used fitted models. In addition, this study gives practically useful guidelines such as flow characterization and valve delay compensation, and identifies physical limits of achievable dynamic performance for a given PSS and SPA, that would help other researchers in the field to design and control soft robotic systems.

While many of the measured results matched the model predictions, there were some deviations, in two case scenarios in particular, where the inertial and viscoelastic dynamics or valve delays affected SPA dynamic behaviour. Future studies can be focussed towards investigating these factors in more detail. By combining existing models for soft actuator kinematics and deformation with the presented pressure dynamics model, we would be able to have a complete representation of the dynamic behaviour of soft robots. Additionally, we assumed isothermal conditions in our analysis. This would not hold true for large pressure changes, such as the use of CO_2 cartridges or high pressure (20-30 MPa) gas cylinders. Lastly, we only investigated the case for a linear pressure-volume relation. There are many SPAs that do not follow this trend, and more analysis will be required to better understand the effect of these non-linearities on the dynamic response. Despite these limitations, however, the presented

work acts as a foundation for future investigations and creates a deeper understanding of the dynamic behaviour of soft actuators.

3 Implementation towards PSS optimization

In the previous chapter, we quantified the direct relationship between soft actuator dynamic performance and various properties and control parameters of the actuator and PSS. These results can be used for customizing the PSS to meet the desired performance requirements. In addition to performance, however, there are many other requirements of the soft robotic system such as size, mass, and portability. These requirements are mutually contradicting such that increased performance or long duration of operation leads to a bulkier PSS. A poorly designed or sub-optimal PSS negatively affects the overall effectiveness of soft robots. In this chapter, we present the design optimization of PSSs in order to simultaneously meet these multiple objectives.

3.1 Introduction

The critical performance requirements to be considered in the design of any robotic system include the force/torque capabilities, kinematics, and actuation speed. In the case of SPA-based systems, the first two can be met by appropriately designing or selecting the SPA, and controlling its actuation pressure. Once these aspects (SPA design and pressure) are fixed, the actuation speed is determined by the pressure and flow dynamics of the PSS (Fig. 3.1A), consisting of the *source*, *valve*, *tubing* and *fittings*. Therefore, in this chapter, we focus on the selection and control of PSS components in order to meet the desired actuation speed. In addition to performance, however, applications often dictate specifications on the PSS in terms of its mass, size, and tubing length. For untethered applications, another important

The material presented in this chapter has been adapted from the following publications:

[76] **Joshi, S., & Paik, J.** (2021). Pneumatic supply system parameter optimization for soft actuators. *Soft Robotics*, 8(2), 152-163. DOI: 10.1089/soro.2019.0134

[77] **Joshi, S., Sonar H. & Paik, J.** (2021). Flow path optimization for soft pneumatic actuators - Towards optimal performance and portability. *IEEE Robotics and Automation Letters*. *IEEE Robotics and Automation Letters*, 6(4), 7949-7956. DOI: 10.1109/LRA.2021.3100626.

S. Joshi conducted experiments, designed the hardware architecture, wrote the manuscript, and contributed to the initial concept and direction of experiments and scientific objectives. H. Sonar designed the custom script for running the hardware, and contributed to the initial concept and manuscript writing. J. Paik supervised the research objectives of the work.

factor to be considered is portability, which can be defined in terms of the amount of air and energy consumed by the SPA. Even for tethered robots, air and energy consumed are important as they directly affect the economic costs; for instance, an SPA used for gripping and manipulating objects in an industrial workspace. However, as shown in Fig. 3.1C, an increase in the dynamic performance and portability of the soft pneumatic system is accompanied by increase in PSS mass and size, which is undesirable for most applications. This creates a trade-off between these conflicting requirements that must be addressed carefully during PSS design.

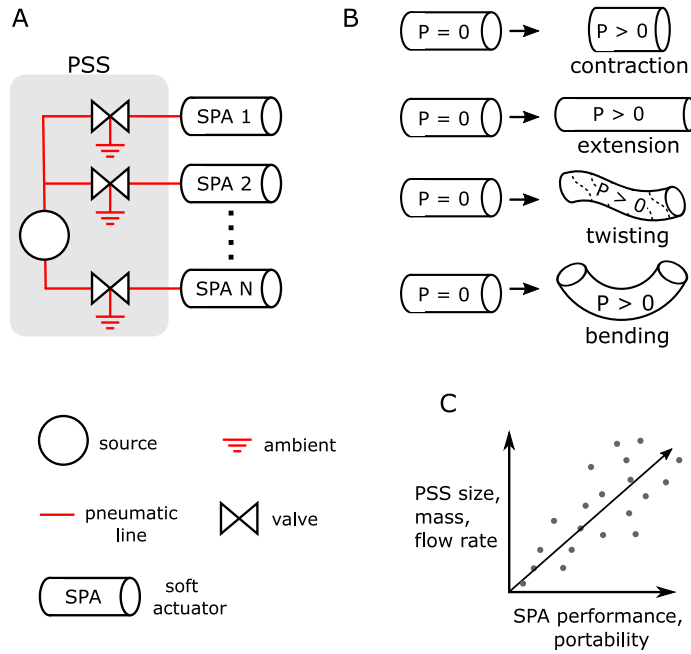


Figure 3.1: A pneumatic supply system (PSS) powering soft pneumatic actuators (SPAs) (A) Schematic of a PSS showing the main components, (B) Different actuation patterns achieved by soft actuators when pressurized ($P > 0$), (C) General trend depicting how improved dynamic performance and portability leads to bulkier PSSs.

Despite its importance, there has been limited work towards PSS design and optimization. Most existing studies rely on heuristic methods for selection and control of PSS components. Such an approach is time-consuming, without guarantee of optimality, and requires re-tuning if a PSS component or SPA is replaced. Wehner et al. [82] studied different options for providing pressurized air and compared them with respect to their flow, air capacity, and mass. However, this study did not account for other components such as the *valve*, *tubing*, and *fittings* and did not quantify their effect for a given SPA. It is not yet well-understood how PSS components can be sized, selected, and controlled to simultaneously addresses the requirements of performance, portability, and user-defined constraints such as size and mass.

Here, as a follow-up to Chapter 2, we present design optimization of PSSs. We discuss the different requirements, formulate the optimization problem, and demonstrate PSS design via simulations and the optimization of a wearable and portable PSS, for a soft exosuit.

3.2 Defining the optimization problem

In order to optimize the design and selection of PSS components, we first define the requirements in terms of the following metrics:

- **Dynamic performance specifications:** These include the soft actuator fall time, rise time and maximum actuation frequency. As discussed in Section 3.1, these metrics are considered only after the selection of the appropriate SPA, which ensures that the desired force and displacement can be achieved.
- **Portability:** The overall portability of a PSS and SPA can be expressed in terms of the air and energy consumed per actuation cycle of the SPA. Alternately, we can also use the metrics of maximum number of actuation cycles attainable in a single charge for a portable system.
- **PSS specifications:** These include requirements such as PSS volume, mass, tubing length, number of outputs, and may also include other requirements such as cost or noise and vibrations.

For optimizing PSSs, the relationship between SPA, PSS, and the above specifications must be quantified. In Chapter 2, we investigated the relationship between the parameters of the PSS and SPA, and dynamic performance metrics of rise time, fall time, and maximum actuation frequency. While these were calculated in free expansion conditions, in practice, SPAs interact with their surroundings and have a non-zero force output, which will lead to deviances in the expected and observed dynamic behaviour. However, as described in Section 2.2.2, the actuation speed is fastest for blocked conditions and slowest for free expansion. By considering the dynamic performance metrics in free expansion, we get a conservative estimate of the actuation speed. If slower speed is desired, it can always be achieved via pressure control. This is why, we choose to use the model and results from Chapter 2 and consider the dynamic performance metrics in free expansion during optimization. For portability, we use the metrics of quantity of air consumed A , and energy consumed E , in one actuation cycle of inflation-deflation. We calculate these by considering isothermal expansion/contraction of air at the standard conditions P_0 , V_0 . The detailed expressions for A and E are described in Section A5. Lastly, for PSS specifications, there is no direct relationship because they are related to the available options of the component. The optimization problem can thus be written as:

$$\min O(x) = w_1 O_1(x) + w_2 O_2(x) + w_3 O_3(x) \quad (3.1)$$

where x is the design variable holding values of PSS parameters; O_1 , O_2 , and O_3 are vectors containing metrics for performance, portability and PSS specifications respectively, and w_1 to w_3 are corresponding weight vectors.

By assigning the desired importance to the different metrics and considering the available options for PSS components, we can use the above equation to optimize the design, selection,

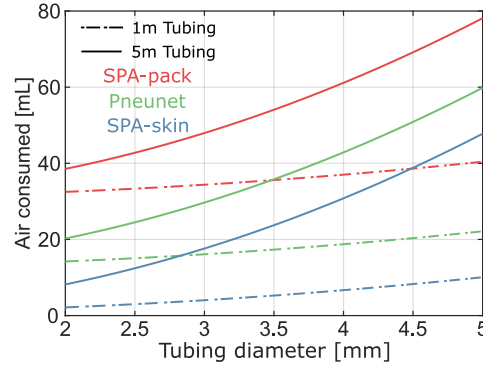


Figure 3.2: Air consumed by the 3 SPAs at different tubing sizes, calculated using Eq. (A29). The line styles represent the length (dotted - 1m, continuous - 5m) and line colours represent the SPA (red - SPA-pack, green - Pneunet, blue - SPA-skin). From Eq. (A29), we observe that the air consumption increases linearly with length and parabolically with diameter.

and control of PSS components. In the next two sections, we demonstrate this method first via simulations, and then by the design of a wearable and portable PSS for powering a soft exosuit.

3.3 Simulation study

Here, we demonstrate how PSSs can be optimized for performance and portability, utilizing the results obtained in Section 2.4. The PSS parameters, x for this study are: (i) the *source* characterized by its pressure P_{src} , (ii) the *valve*, characterized by its sonic conductance C_{valve} , and (iii) the *tubing*, characterized by its diameter D and length L . We use the metric of maximum actuation frequency, $f_{max}(x)$, for performance and air consumed per actuation cycle, $A(x)$, and energy consumed per actuation cycle, $E(x)$, for portability. We can now define a multiple-objective optimization problem for optimal performance and portability as follows:

$$\min O(x) = w_1 |f_{max}(x) - f_{desired}| + w_2^1 A(x) + w_2^2 E(x) \quad (3.2)$$

where $f_{desired}$ is the desired value of the actuation frequency. We choose $|f_{max}(x) - f_{desired}|$ as the first objective and a very large w_1 , which will incur a large penalty if there is significant difference between the achieved f_{max} and its desired value. Next, depending on the relative values of the weights w_2^1 and w_2^2 , we can consider different available options and find the optimal solution.

For the 162 test conditions considered in Section 3.4, we calculated the air and energy consumed using Eq. (A29) and (A30) respectively. Fig. 3.2 shows the air consumed in mL for the SPAs, for tubing lengths 1m and 5m. Also, Fig. 2.10 from Section 3.4 shows f_{max} for a tubing length of 1m and 5m. Using these results, we can compare different options and select optimal components for the objective function. We explore two examples as described below and in Table 3.1. In these examples, we fix the SPA used, tubing length and desired actuation frequency, and find the optimal tubing diameter and source pressure as follows:

Table 3.1: Multi-objective optimization for performance and portability

SPA-pack $L = 1 \text{ m}$ $f_{max} = 4 \text{ Hz}$

P_{src} [kPaG]	D [mm]	A [mL]	E [J]
60	3.25	35	1.66
80	2.75	33.8	1.99
100	2.5	33.3	2.33

SPA-skin $L = 5 \text{ m}$ $f_{max} = 6 \text{ Hz}$

P_{src} [kPaG]	D [mm]	A [mL]	E [J]
80	2.75	14.9	0.88
100	2.25	10.2	0.71
100	3.4	22.1	1.54

1. SPA-pack, 1 m tubing, desired $f_{max} = 4 \text{ Hz}$: For this combination, we note from Fig. 2.10 that we need Valve 2. We can achieve 4 Hz by choosing one of the three options as shown in Table 3.1. If E has to be minimized, then the first option is preferable, whereas if A is to be minimized, the third option is optimal.
2. SPA-skin, 5 m tubing, desired $f_{max} = 6 \text{ Hz}$: For this combination, we will again need valve 2, and we can choose one of the three options shown in Table 3.1. In this case, the second option with smaller diameter and higher pressure is the optimal solution as it minimizes both A and E .

The above can be easily implemented to any other set of requirements so as to meet the desired requirements of performance, portability, and PSS specifications. In addition to PSS optimization, one interesting observation from these results is that for a given PSS (P_{src} , C_{valve} , D and L), A has inverse relation with f_{max} . For example, for tubing of size 2 mm diameter and 1 m length, the f_{max} for SPA-pack and SPA-skin are 2.9 Hz and 43.5 Hz, and corresponding A values are 38.5 and 2.2 mL. This is because, the product of f_{max} and A is the average flow output per sec for the PSS, which would be roughly the same even while powering different SPAs. Furthermore, this product is proportional to the product of P_{src} and C_{valve} , which is an indication of the flow capacity of the system, as seen from Eq. (2.3).

3.4 Implementation to PSS design

Here, we demonstrate the design optimization of a wearable and portable PSS for meeting dynamic performance, portability, and PSS specifications.

Table 3.2: Design requirements and corresponding achieved values of the fabricated PSS

Dynamic performance specifications *		Achieved Values
T_{rise}	< 0.45s	0.42s
T_{fall}	< 0.65s	0.59s
f_{max}	> 0.9 Hz	0.99 Hz
Portability		Achieved Values
Number of actuations	> 5000	> 6000
PSS Specifications		Achieved Values
Overall mass	< 3 kg	1.95 kg (optimized)
Overall volume	< 0.4 x 0.3 x 0.2 m	0.3 x 0.2 x 0.15 m
Tubing length**	0.5 m	0.5 m
Output channels	6	6

*specifications for a

single SPA-pack;

**from valve to SPA-pack

3.4.1 Design requirements

We have prototyped a soft exosuit as shown in Fig. 3.4A, for studying force interactions with the human torso (detailed description in Chapter 5). This exosuit consists of six SPA-packs [60] (Fig. 3.5A), capable of producing forces up to 40 N each. We calculated the dynamic performance requirements of this exosuit for an application to support the wearer's weight in awkward work postures, based on [104; 105; 106; 107; 108], and a pilot study. These requirements must be met by a portable PSS, which should be compact and lightweight. Table 3.2 summarizes these performance requirements and PSS specifications.

Using our mapping results from Section 3.3 (Figs. 2.3, 2.4 and 2.5), we calculated the range of PSS parameters f and c which meet performance requirements given in Table 3.2. Using these values, we compared commercially available options for *source*, *valve* and *pneumatic lines* in order to find the optimal set of PSS components as described below:

1. For a tubing length of 0.5m (between valve and SPA-pack), we compared options for standard pneumatic tubing with internal diameters of 1.2mm, 2.5mm, 4mm and 5mm. Using Eq. A22, we calculated C and b for each, as well as V_{spa}^0 and K_{exp} by adding the tubing internal volume to the SPA-pack internal volume. For our specific case, the tubing volume is much smaller with respect to the SPA-pack volume (0.079L). Using a conservative approach, we considered the largest diameter to get $V_{spa}^0 = 0.083L$ and $K_{exp} = 1.51 V_{spa}^0/MPa$.
2. For $P_{op} = 0.2MPaG$ and the above value of K_{exp} , we used Figs. 2.4, 2.5 and Fig. 3.3 to find predicted values of T_{rise} for a range of P_{src} , \bar{c} and b_{eq} . The regions above $T_{rise} = 0.45s$ in Fig. 3.3 correspond to values of P_{src} , \bar{c} and b_{eq} which will satisfy the requirements of rise time. Additionally, we predicted T_{fall} for a range of \bar{c} and b_{eq} , using Figs. 2.3 and 3.4E. Using the predicted T_{fall} and T_{rise} from the figures, we calculated the acceptable range of

values of P_{src} , \bar{C} and b_{eq} .

- Next, we compared available valves and fittings, and noted the combinations of valve, tubing and fittings with \bar{C} and b_{eq} lying in the acceptable range.
- From the desired number of full actuations, we calculated the total amount of air required as 897 standard litres by applying Eq. 3.2. Using this and acceptable range of P_{src} , we

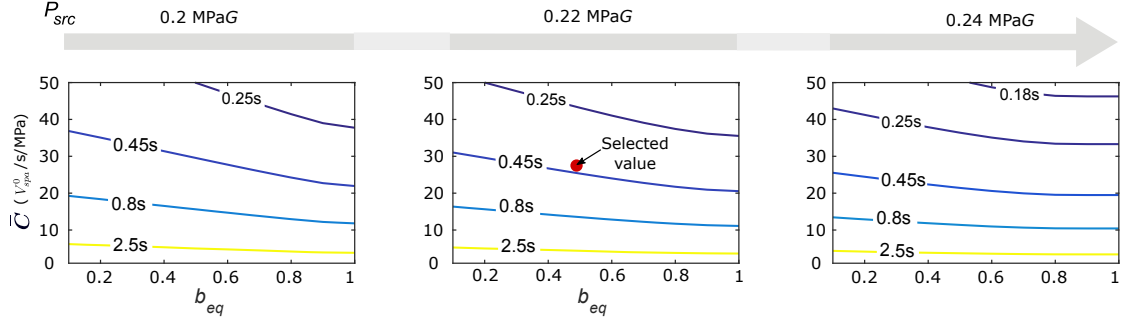


Figure 3.3: Predicted rise time for the SPA-pack with expansion ratio, $K_{exp} = 1.51$, and operating pressure, $P_{op} = 0.2\text{MPaG}$, at varying values of P_{src} , \bar{C} and b_{eq} . Since the requirement is $T_{rise} < 0.45\text{s}$, the selected valve, tubing and fittings should have \bar{C} and b_{eq} lying in the region above the curve $T_{rise} = 0.45\text{s}$. For our prototype, the selected components correspond to $P_{src} = 0.22\text{MPaG}$, $\bar{C} = 26.89$ and $b_{eq} = 0.49$. At these values, we get $T_{rise} = 0.39\text{s}$ as shown by the highlighted point.

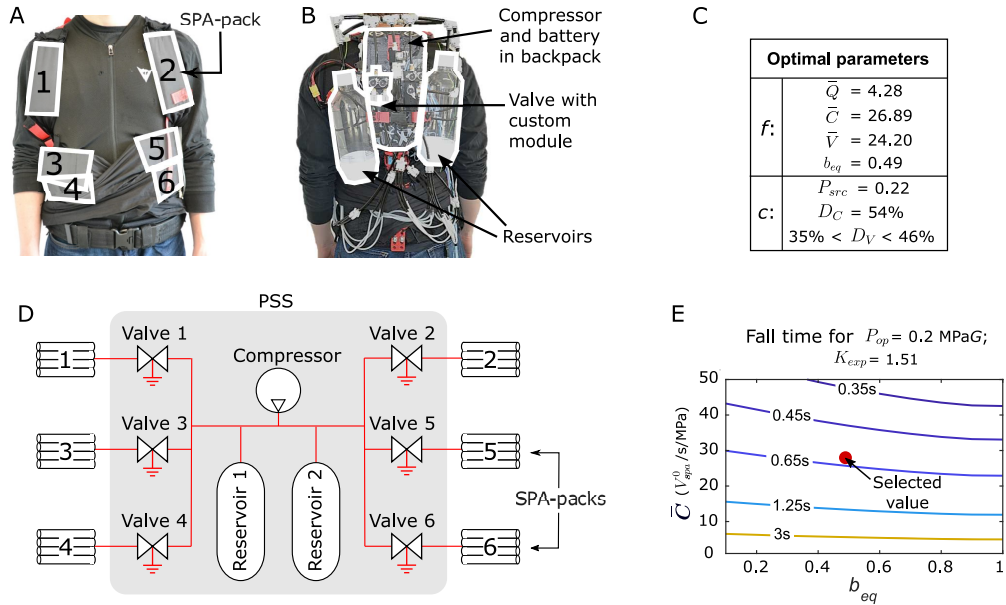


Figure 3.4: PSS design via parameter optimization (A) Soft exosuit, which is to be powered by the PSS. It consists of six SPA-packs marked 1 to 6, (B) Prototype of the optimized PSS, fabricated in the form of a backpack. (C) Optimized flow and control parameters required to meet requirements of Table 3.2, (D) Schematic of the PSS for the exosuit powering 6 SPA-packs, (E) Predicted fall time for $P_{op} = 0.2\text{MPaG}$ at a range of \bar{C} and b_{eq} . The highlighted point corresponds to the selected combination of valve, tubing and fitting for the prototype, with predicted $T_{fall} = 0.6\text{s}$.

compared available options for the *source* as follows:

- (a) Pressure regulated: We compared acceptable options among high pressure cylinders and liquid CO_2 , which could meet the total air requirement, along with their regulators.
 - (b) Compressor based: We compared acceptable compressors and battery combinations that could provide P_{src} , the total air requirement and f_{max} (from Eq. 2.18). Then we calculated \bar{v} required for simultaneously powering four SPA-packs, using Eq. 2.14, and compared possible options for reservoir.
5. For every combination of PSS components that could meet performance requirements, we calculated the total PSS volume and mass. We selected the combination with minimum mass of components, as listed in Table A3. It consists of a battery-powered compressor, two reservoirs, standard tubing and fittings, and six sets of proportional valves with custom manifolds.
 6. For the selected components, we used Eq. 2.18 and 2.19 to calculate optimal D_C and D_V . With the optimally selected components, we prototyped and assembled the PSS in the form of a backpack as shown in Fig. 3.4B. The total mass of the selected PSS components is 1.95 kg, and their optimal flow and control parameters are as listed in Fig. 3.4C, and highlighted in Figs. 2.3, 2.4, 2.5, 3.3, 3.4E.

3.4.2 Comparison with experimental testing

We tested the prototype while powering a single SPA-pack (Fig. 3.5A) in two conditions, free expansion and blocked. For both cases, we measured the pressure response ten times on a bench-top. To compare the observed dynamic behaviour with that predicted by our model, we simulated the SPA-pack response in these two conditions. For simulating blocked conditions, we selected the expansion ratio value to be, $K_{exp} = 0$.

From Fig. 3.5B, we observe that the PSS meets desired performance requirements of T_{rise} , T_{fall} and f_{max} , and the measured data shows good agreement with simulations. Additionally,

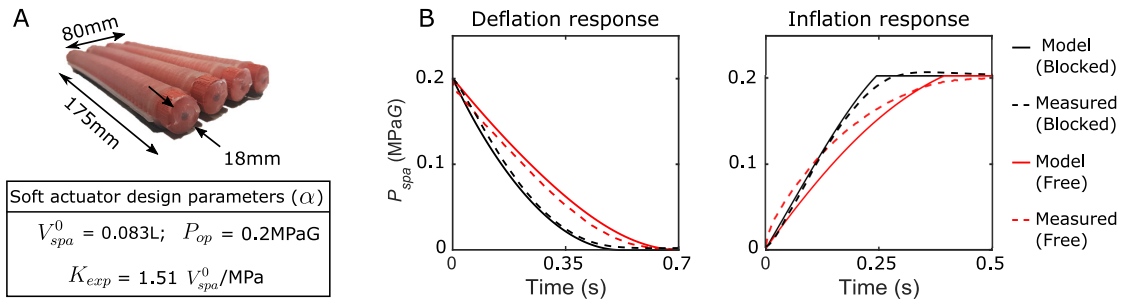


Figure 3.5: Validation of PSS parameter optimization via off-board testing of the SPA-pack dynamic performance. (A) The SPA-pack used in the soft exosuit. (B) Comparison of simulations (continuous lines) with measured pressure response (dotted lines) in inflation and deflation, in blocked (black) and free conditions (red). Each test was carried out ten times. P_{src} before inflation was 0.22MPaG and 0.24MPaG for free and blocked conditions respectively.

Table 3.3 shows the peak and root mean squared (RMS) errors between simulation and experimental results. RMS errors for blocked conditions and deflation in free conditions were found to be less than 3.1%. A slightly higher error (5.2% RMS, 13.2% peak) was observed for inflation during free expansion (Fig. 3.5B), which can be attributed to inertial forces on the SPA-pack.

Table 3.3: Comparison of measured pressure response of the SPA-pack with simulations

	RMS Error [%]		Peak Error [%]	
	Free	Blocked	Free	Blocked
Inflation	5.2	1.6	13.2	6.0
Deflation	3.1	2.1	5.2	5.1

3.5 Discussion

The design problem for PSSs is characterized by conflicting requirements of the SPA dynamic performance, portability, and user-defined specifications. Earlier approaches relied on instinct, experience, or heuristic methods for design, which are insufficient to address multiple objectives, and lead to sub-optimal systems. Here, we introduced design optimization of PSSs for simultaneously meeting these opposing requirements. After defining the optimization problem, we demonstrated our approach using two examples. First, we presented the optimization of tubing diameter and source pressure for meeting requirements of performance and air and energy consumption. We used the results of maximum actuation frequency from the previous chapter along with estimates of air and energy consumption, and discussed two case scenarios. Next, we demonstrated the design of a wearable and portable PSS for powering an exosuit with six soft actuators, while minimizing mass of the PSS components. For this, we used the mapping from PSS and SPA parameters to dynamic performance metrics from the simulation results of the previous chapter, and compared commercially available components to minimize the overall mass. Results from experimental testing with the wearable PSS showed good agreement with simulations, thereby validating the proposed approach. By enabling optimized PSSs for robotic applications this work is a step towards customizing soft robotic systems and will help to broaden the scope of soft robots. The current study was limited to using model predictions and comparing all available options from the design variables. In future studies, different optimization algorithms can be explored to address more challenging design problems than the ones discussed in this study.

4 Sensorless force and displacement estimation in soft pneumatic actuators

In Chapter 2, we investigated the effect of PSS and SPA properties on SPA dynamic response. In addition to these factors, the actuation dynamics are also affected by its loading conditions. For instance, a given SPA will exhibit different pressure responses when it is allowed to fully inflate, as compared to when it is completely blocked. This suggests that by monitoring the pressure response of a given SPA, it could be possible to speculate if and how the SPA interacts with its surroundings. In this chapter, we exploit this principle and present a previously unknown property of SPAs: self-sensing. While conventional sensing methods require displacement and/or force sensors, our proposed method enables us to estimate these quantities without the need for dedicated sensors.

4.1 Introduction

The nonlinear behaviour, compliance and highly redundant kinematics of SPAs lead to challenges in modelling and therefore necessitate sensing and feedback control for practical use [19]. Several researchers have embedded displacement sensors in SPAs, including commercial flex sensors [109; 110], or custom-fabricated sensors such as microchannels filled with ionic solutions [111; 112] or liquid metal alloys [113; 114], stretchable capacitors [115; 116], and also magnetic [117; 118], optical [119; 120] and pneumatic-based sensors [121; 122]. Force sensing has been implemented more recently, using either dedicated force sensors [123; 39] or more commonly, indirect force estimation via embedded displacement sensors [124; 125; 100; 126]. While significant work has been done, several challenges still exist including the complex and expensive manufacturing processes, alteration of the SPA mechanical properties, failure of actuator-sensor interfaces, hysteresis and drift. Furthermore, most existing studies characterize their sensors under simple loading conditions, which do not match the actual application. As the mechanical behaviour of SPAs is significantly affected by the loading conditions, this could give rise to considerable differences in sensor predictions vs. actual values of force and

The material presented in this chapter has been adapted from the following publications:
Joshi, S. & Paik, J. (2021). Sensorless force and displacement estimation in soft pneumatic actuators. IEEE/ASME Transactions on Mechatronics (under review)

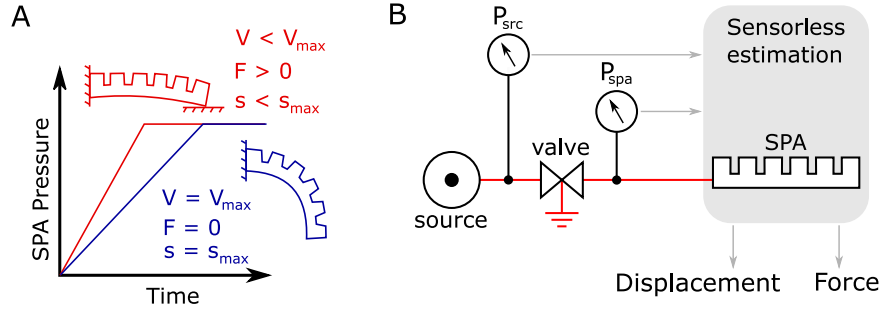


Figure 4.1: Sensorless estimation in pneumatic actuators. (A) Different pressure responses in free (blue) and blocked (red) conditions. In free expansion, the SPA inflates to its full volume and displacement and output force is zero. Due to the large volume, more air is required to pressurize it, leading to a slower response, i.e. smaller rate of change of pressure. In the blocked condition, the SPA is prevented from inflating to full volume and displacement. Due to the comparatively smaller volume, less air is required to inflate it, leading to a faster response, i.e. larger rate of change of pressure. (B) Schematic of the sensorless estimation method, that uses data from pressure measurements only to estimate SPA force and displacement.

displacement.

A possibility worth consideration is to investigate if the SPA can serve as a smart material with both actuation and sensing capabilities. As studied in Chapter 2, the pressure response of an SPA depends on the flow capacity of the pneumatic supply system, PSS (Fig. 4.1B), and the size of the SPA: a smaller SPA and high PSS flow capacity leads to faster response and vice versa. In a similar manner, the pressure response is also affected when the SPA interacts with its environment. For instance, consider the following two extremes shown in Fig. 4.1A. Under blocked condition, the SPA internal volume does not change and we get a pressure response shown by the red curve in the figure. During free expansion on the other hand, the SPA internal volume increases, which requires more airmass that in turn leads to a slower response. This was also observed from Fig. 3.5B in the previous chapter, in which the pressure response of the SPA-pack was slower for the free expansion, as compared to blocked conditions. This difference in pressure response and airmass in the SPA is thus an indicator of its interaction with the surroundings, and could be used for estimating how it interacts with its surroundings. Since the actuator itself acts as the sensing element without requiring dedicated force or displacement sensors, such a method is called self-sensing or sensorless estimation. In electrical systems like electric motors [127], shape memory alloys [128; 129], piezoelectric actuators [130; 131], dielectric elastomer actuators [132; 133; 134], twisted coil actuators [135] and metal-polymer hybrid soft actuators [136], sensorless estimation has been implemented to estimate the actuator state (e.g. temperature, displacement and/or force) by measuring and monitoring the voltage, current, charge and capacitance. Similarly in SPAs, its force and displacement could be predicted using information about pressure, flow through the PSS, airmass and volume. Such sensorless estimation in SPAs adds a new dimension to soft sensing that would eliminate the need for dedicated sensors completely, thereby circumventing their current challenges. This will enable state feedback control for applications where embedding sensors is currently not possible because sensor integration

is too difficult, expensive or not permissible, for example in magnetic resonance imaging applications [40]. Alternatively, implementing sensor fusion of this method with pre-existing sensors in the SPA would add sensing redundancy, thereby improving estimation accuracy or for use in sensing multiple displacement modes such as bending, extension or twisting [126; 116; 114]. Furthermore, this method could also be readily applied to conventional rigid pneumatic actuators. Along with these advantages, however, sensorless estimation has many challenges and uncertainties that must be addressed.

Firstly, the feasibility of sensorless methods in SPAs has not been previously studied. Secondly, as investigated in Chapter 1, the SPA loading conditions strongly govern its mechanical behaviour. Especially because this is a new sensing concept for SPAs, it is necessary to verify that sensorless estimation can consistently predict force and displacement under diverse loading conditions. Additionally, as this method models the SPA itself as a sensor, its nonlinearities and time-dependent properties would also be translated to its sensing capabilities. Sensorless estimation in SPAs would require information about their pressure, flow, airmass and volume, similar to actuator voltage, current, charge and capacitance respectively, for electrically powered actuators. Unlike electrical systems, however, there are no existing methods for estimating internal volume or airmass of SPAs in real-time; and the pressure and flow dynamics are highly nonlinear [85]. Lastly, it is not known how SPA properties such as its size, shape, actuation mode, materials used and operating pressure would affect its sensing accuracy.

Here, we address these challenges and investigate sensorless estimation for SPAs for the first time. To assuredly validate the feasibility of this method, we test a bending SPA exhaustively in a range of loading conditions based on commonly observed applications: two anchoring conditions that dictate how the SPA is constrained to its environment; and a diverse set of displacement and actuation sequences, largely consisting of randomly chosen values. After modelling the pressure dynamics, we devise a monotonic relation between pressure and PSS flow, thereby requiring only pressure sensors to estimate the flow, volume and airmass. To address the nonlinear and time-dependent behaviour of the SPA and pneumatic system, we train time-delay neural networks with the measured data, to estimate force and displacement using inputs derived from pressure measurements only. Our results show root mean square errors of under 10% and 20% for force and displacement respectively, even with previously unseen and unique testing conditions. Additionally, we compare the results to those obtained using a flex sensor affixed to the SPA, and implementing sensor fusion with our proposed method. While the flex sensor led to better results than the sensorless approach, the sensing redundancy of sensor fusion led to consistently improved accuracy than using the either of the two individually. As pressure sensors are universally used in most existing pneumatics-based devices, the proposed method can be implemented directly without the need for any additional components, even for rigid systems.

4.2 Defining pneumatic inputs and mechanical outputs for sensorless estimation

Sensorless estimation for SPAs requires a mathematically well-defined relationship between the mechanical outputs of force and displacement and the pneumatic inputs of pressure, flow, airmass, and internal volume. In addition to the SPA design and materials, such a relationship is also dependent on the loading conditions. Since sensorless estimation has not been studied before for SPAs, it is unknown whether such a relationship really exists. In this chapter, we assess the feasibility and investigate sensorless estimation for the first time.

We model the pressure and flow dynamics for SPAs and derive expressions to calculate and define the pneumatic inputs of SPA pressure, flow, airmass and internal volume, using pressure measurements only. To address the dependency on loading conditions, we consider a bending SPA in two application scenarios, mobile robots and wearable robots, and define the mechanical outputs of force and displacement.

4.2.1 Modelling pressure and flow dynamics

Using the ideal gas law, the SPA pressure dynamics can be expressed as described in Section A3. We rewrite the equations as:

$$\frac{d}{dt}(P_{spa}V_{spa}) = P_0Q_{spa} \quad (4.1)$$

where P_{spa} and V_{spa} are the instantaneous SPA pressure and volume respectively, and Q_{spa} is the mass flow rate expressed as volumetric flow at standard conditions, P_0 , T_0 . Integrating between initial time, t_0 , and current time, t , and rearranging, we get the expression for the SPA instantaneous internal volume and airmass inside the SPA as follows,

$$[V_{spa}]_t = \frac{P_0 \int_{t_0}^t Q_{spa} dt + [P_{spa}V_{spa}]_{t_0}}{[P_{spa}]_t} \quad (4.2)$$

$$\text{airmass} = \frac{[P_{spa}V_{spa}]_t}{P_0} = \int_{t_0}^t Q_{spa} dt + \frac{[P_{spa}V_{spa}]_{t_0}}{P_0} \quad (4.3)$$

Although prone to integration drift over time, this approach could still prove the feasibility of self sensing for shorter durations. Knowing the unactuated SPA volume, $[V_{spa}]_{t_0}$, and tracking the airflow, we can thus calculate the instantaneous SPA volume and the airmass inside the SPA. This can be achieved by direct measurement via flow sensors. Alternatively, we can also model and estimate the flow in real-time as it is governed by the properties of the PSS [85], valve state (*inflate*, *deflate* or *hold*) and SPA pressure. Here, we model it using an updated

4.2. Defining pneumatic inputs and mechanical outputs for sensorless estimation

version of the ISO 6358 standards [84] as,

$$Q_{spa} = C\Psi P_{High} \quad (4.4)$$

$$\Psi = \begin{cases} \left[1 - \left(\frac{\frac{P_{Low}}{P_{High}} - b}{1-b} \right)^2 \right]^m, & \frac{P_{Low}}{P_{High}} \geq b \\ 1, & \frac{P_{Low}}{P_{High}} < b \end{cases} \quad (4.5)$$

where, C , b , and m are the sonic conductance, critical ratio ($0 < b < 1$) and the subsonic index ($0 < m < 1$), respectively; P_{High} and P_{Low} are the absolute upstream and downstream pressures respectively; and Ψ is the nonlinear flow function. During inflation, $P_{High} = P_{src}$, and $P_{Low} = P_{spa}$. During deflation, $P_{High} = P_{spa}$, and $P_{Low} = P_0$. The above expression can be used to calculate the flow through a PSS consisting of a wide range of pneumatic components including valves, tubing and fittings [85]. Thus, using Eq. 4.2-4.5, we can calculate the pressure, flow, volume and air mass using only pressure sensors.

4.2.2 Defining SPA force and displacement

As demonstrated in Chapter 1, the SPA force and displacement behaviour are dictated by its loading conditions, defined by their (i) *anchoring condition*, which describes the nature of contact between the actuator and surroundings, (ii) *displacement boundary condition*, which specifies how the actuator moves at these contact points, and (iii) *actuation power*, which corresponds to the input. Here, using a bending SPA-pack, we focus on two commonly observed application scenarios of soft actuators, and define their loading conditions as follows:

- **Pulling:** The two ends of the SPA-pack are constrained to hinge joints, which allows free rotation at the ends as shown in Fig. 4.3A. This is exactly similar to the *Pulling* loading condition in Chapter 1. Here, the SPA displacement is defined by the distance between its two ends.
- **Three-point bending:** The central section of the SPA is fixed, while the two ends are constrained using an overlapping fabric to prevent vertically upward motion of the ends as shown in Fig. 4.4A. This type of anchoring condition is observed in wearable devices where an SPA is attached to the user's body via flexible, non-stretchable straps [20; 40]. The displacement is defined by the deflection of the SPA mid-point with respect to its two ends. In this anchoring condition, there are additional nonlinearities due to making and breaking contact, slack in the fabric strap and friction at the cantilever.

4.3 Experimental characterization of SPA-pack

As sensorless estimation in SPAs has not been studied before, the nature of the relationship between pneumatic inputs and mechanical outputs is unknown. Furthermore, it is affected by the nonlinearities of SPA material properties, pressure dynamics, flow dynamics, and loading conditions. Therefore, for this first study, we experimentally characterize the SPA and adopt a data-driven method to investigate the correlation between the inputs and outputs. We first characterize the PSS and model its flow according to ISO 6358 (Eq. 4.5). Then, we exhaustively characterize the SPA-pack while controlling its loading conditions for the two application scenarios described earlier.

4.3.1 Experimental setup

We power the SPA-pack using a PSS consisting of a regulated pressure supply at 200 kPaG from an external compressor, solenoid valves (SMC VV100 series) and standard pneumatic tubes (SMC, I.D. = 2.5mm) as well as pressure (Panasonic MPX5500DP) and flow sensors (Honeywell AWM5000 series) as shown in Fig. 4.2A. To facilitate the comparison of sensorless estimation with conventional sensing, we affixed a standard flex sensor (SpectraSymbol, 113mm x 6.4mm x 0.5mm) on the non-extending side of the SPA-pack as described in Fig. A5. In order to accurately control the SPA loading conditions and measure its force and displacement, we used the modular robotic platform described in Section 1.3 and Fig. 1.1.

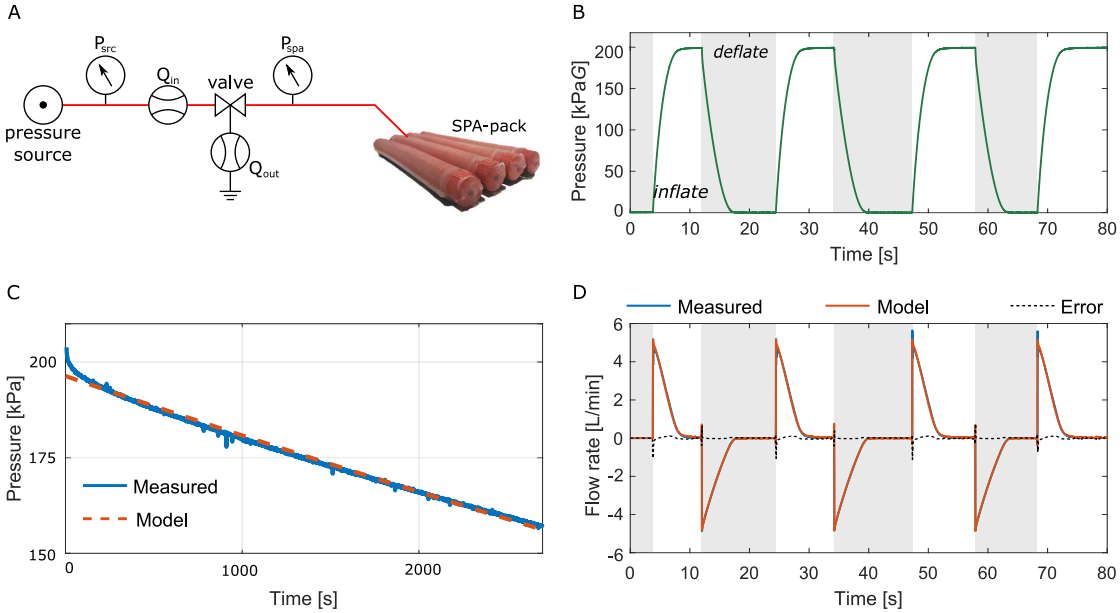


Figure 4.2: PSS characterization: We powered an SPA-pack [60] using a PSS, measured the flow during inflation and deflation, and fit the model parameters C_{eq} , b_{eq} , and m_{eq} to the measured data. (A) The SPA-pack used for testing, (B) The measured pressure response, (C) Measured vs. model pressure response during leakage characterization. We inflated the SPA-pack in completely blocked conditions, monitored the pressure response due to leakage, and fit the measured data using the ISO 6358 [84] standards. (D) Measured vs. calculated flow using ISO 6358 [84].

4.3.2 Experimental protocol and data collection

PSS Characterization

We characterized the PSS and express the flow as a monotonic function of pressure, which eliminates the requirement of a flow sensor. We inflated and deflated the SPA-pack cyclically between 0 kPaG to 200 kPaG ten times, measured the pressure and flow (Fig. 4.2), and fitted the parameters of Eq. 4.4 and 4.5 to the measured data, using the *lsqcurvefit* solver in MATLAB. Additionally, since presence of leakage induces errors in the integrated quantities of Eq. 4.3, we also characterized leakage flow. We inflated an SPA-pack to 200 kPaG under blocked conditions, and monitored its pressure for 45 minutes. Assuming that SPA internal volume remains constant under blocked conditions, we modelled the pressure loss due to leakage as:

$$\dot{P}_{spa} V_{spa}^0 = P_0 Q_{leak} \quad (4.6)$$

where Q_{leak} is the leakage flow. Fig. 4.2C shows the measured vs. modelled flow and Fig. 4.2D shows the measured vs. modelled pressure response due to leakage. Table 4.1 shows the fitted values of the ISO 6358 model for the flow paths of inflation, deflation and leakage.

Table 4.1: ISO 6358 parameters for Inflation, deflation and leakage

Valve path	C [lpm/kPa]	b	m
Inflation	1.8×10^{-2}	0.15	0.57
Deflation	1.74×10^{-2}	0.12	0.6
Leakage	3.36×10^{-7}	0.5	0.5

SPA characterization

SPA loading conditions are defined by its *anchoring conditions*, *displacement boundary conditions* and *actuation power*. We affixed the SPA-pack to the platform in the two anchoring conditions as described earlier. For *pulling*, displacement is directly calculated from the distance between modules 1 and 3, ranging from 0mm, when the SPA-pack is flat (Fig. 4.3B), to 80mm when the SPA-pack is bent (Fig. 4.3C). For *three-point bending*, displacement is the deflection of the SPA mid-point with respect to its two ends, ranging from 0mm when the SPA-pack is flat (Fig. 4.4B), to 70mm, when it is bent (Fig. 4.4C). Since the SPA-pack is constrained by the fabric strap, there are instances when the straps become loose and the SPA is in free expansion (zero force). As a result, the ground truth values of displacement cannot be directly calculated using the motion of module 2. We address this by calculating ground truth of the displacement separately for regions of constrained (non-zero force) and free motion (zero force) of the SPA as described in Section A8. Next, we define actuation power as the percentage of airmass inside the SPA, with respect to its full capacity. We calculated the full

capacity by inflating the SPA-pack from 0 to 200 kPaG at zero displacement, and integrating the flow rate with respect to time. This was found to be 0.181L for pulling, and 0.173L for three-point bending. Based on the displacement and actuation power, we then characterized the SPA-pack in four loading sequences as shown in Fig. 4.5:

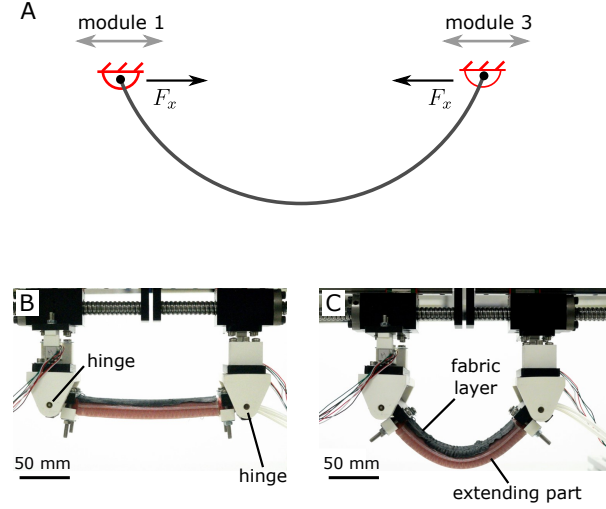


Figure 4.3: Pulling force: This loading condition is defined by hinge constraints on the two ends of the bending SPA. It is observed in inchworm robots [58; 59; 46]. (A) Schematic of SPA-pack affixed on the robotic testing platform, (B) SPA-pack in flat configuration (C) SPA-pack in bent configuration

1. *hold*: We inputted a fixed amount of airmass into the SPA, and enforced an oscillating displacement from 0 to 100% in a triangular pattern with three waves, as shown in Fig. 4.5. We repeated this for 10%, 20%, 30%, ..., 100% of full capacity, to have a total of 10 tests.
2. *cyclic*: This consists of a cyclic wave of displacement between 0 and 100%, and a cyclic pressure control of 0 and 200 kPaG. We repeated this four times, with each test lasting 300s.
3. *step*: This consists of a step displacement, followed by a step of air input. We used three values each for the displacement and airmass (25%, 50% and 75% of full capacity) to have a total of 9 tests.
4. *random*: For this, the microcontroller generated randomized set points for the displacement and airmass, at randomized time intervals. The randomizer was a pseudo-random value from 0%, 5%, 10%, 15%, ..., 100% for the displacement and airmass. The time interval between different values was also chosen randomly from 0s, 0.5s, 1s, 1.5s, ..., 10s. We repeated 20 such tests, each lasting 300s.

For all tests, the displacement speed was 5mm/s except for *cyclic*, where we used four different speeds for the four tests, from 5mm/s to 10mm/s to ensure unique loading conditions.

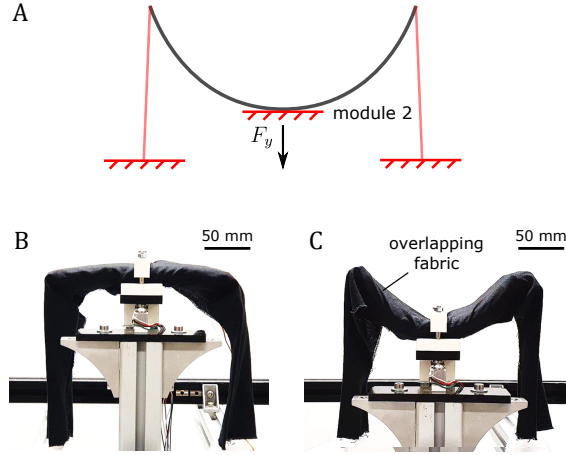


Figure 4.4: *Three-point bending:* This loading condition is defined by fixed constraint at the central section, while the ends are constrained in the vertically upward direction. It is observed in wearable robots [20; 40]. (A) Schematic of SPA-pack affixed on the robotic testing platform, (B) SPA-pack in flat configuration (C) SPA-pack in bent configuration

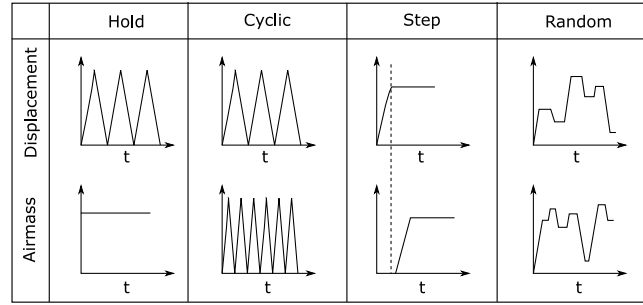


Figure 4.5: Displacement and air input conditions during the four loading sequences: (i) *hold*, (ii) *cyclic*, (iii) *step*, and (iv) *random*

4.4 Neural network design, training and validation

In the previous sections, we collected data for a bending SPA in two anchoring conditions and a large set of displacement and actuation sequences. In this section, we aim to establish a relationship between the pneumatic inputs (pressure, flow, air mass, and volume) and mechanical outputs (force and displacement). Initially, we tested polynomial regression with the pneumatic inputs. Although it showed good accuracy for the loading sequence of 'hold', it could not map the input-output relation for the other three loading sequences. This is primarily because of the nonlinearities in the SPA design, material properties, pressure and flow dynamics, and loading conditions. Furthermore, some of the input features are calculated using integrated quantities, which are prone to drift. Neural networks, and more specifically time-driven neural networks, pose an attractive choice for mapping this kind of nonlinear and time-dependent input-output correlation. Therefore, we implemented time-delay neural nets as follows:

$$Y(t) = f(X(t-1), X(t-2), \dots, X(t-N-1)) \quad (4.7)$$

where $Y(t)$ represents the force and displacement, and $X(t)$ represents neural net inputs at time-step t . We heuristically chose a delay of two time steps, i.e., $N = 2$, based on the time required for training and estimation accuracy. Using the MATLAB Deep Learning Toolbox, we designed neural nets consisting of an input layer, one hidden layer and an output layer, as shown in Fig. 4.6D. The activation functions were tan-sigmoid for the hidden layer and linear for the output layer.

4.4.1 Defining input features and neural net architectures

Based on the SPA pressure, flow, airmass and volume, we designed and tested different input features for sensorless estimation and heuristically selected the following thirteen:

- i SPA pressure: P_{spa} , which was measured using a pressure sensor
- ii Related to flow: $Q_{in}, Q_{out}, Q_{leak}$, which were calculated using the ISO 6358 model as described in 2.3 and 4.5 and Table 4.1.
- iii Related to airmass: These are calculated by integrating the flow values: $P_0 \int Q_{in} dt$, $P_0 \int Q_{out} dt$, $P_0 \int Q_{leak} dt$, initial value of $[P_{spa} V_{spa}]_{t_0}$, and the estimate of $P_{spa} V_{spa}$ using Eq. 4.3.
- iv Related to volume: These are calculated by dividing the airmass related features with the SPA pressure and include an estimate of V_{spa} along with $\frac{\int Q_{in} dt}{P_{spa}}$, $\frac{\int Q_{out} dt}{P_{spa}}$, $\frac{\int Q_{leak} dt}{P_{spa}}$

From Eq. 4.2-4.5, we see that all the above input features are calculated from pressure data. Therefore, theoretically, the neural net should be able to map the relationship from valve-state (ON, OFF, HOLD) and pressures to the SPA force and displacement. However, as these additional inputs represent physical properties, they provide information rich features [137], which improved our estimation accuracy. Similarly, some of these features are redundant, for example $P_{spa} V_{spa} = [P_{spa} V_{spa}]_{t_0} + \int (Q_{in} dt - Q_{out} - Q_{leak}) dt$. However, small deviances in calibration or integration drifts can accumulate large errors over time which is why we chose to keep the redundancy.

Rather than studying sensorless estimation by itself, it would be advantageous to evaluate its effectiveness compared to conventional sensing approaches. Therefore, we implemented and compared a total of three sensing methods in this study: (i) sensorless estimation, which uses all of the 13 features described previously as shown in Fig. 4.6A, (ii) flex sensor, which uses data from the air pressure sensor and the flex sensor as shown in Fig. 4.6B, and (iii) sensor fusion, which simply uses data from the flex sensor in addition to the 13 features of sensorless estimation as shown in Fig. 4.6C. For each, we considered four hidden layer sizes consisting of either 4, 8, 12 or 16 neurons, to give 12 neural net architectures.

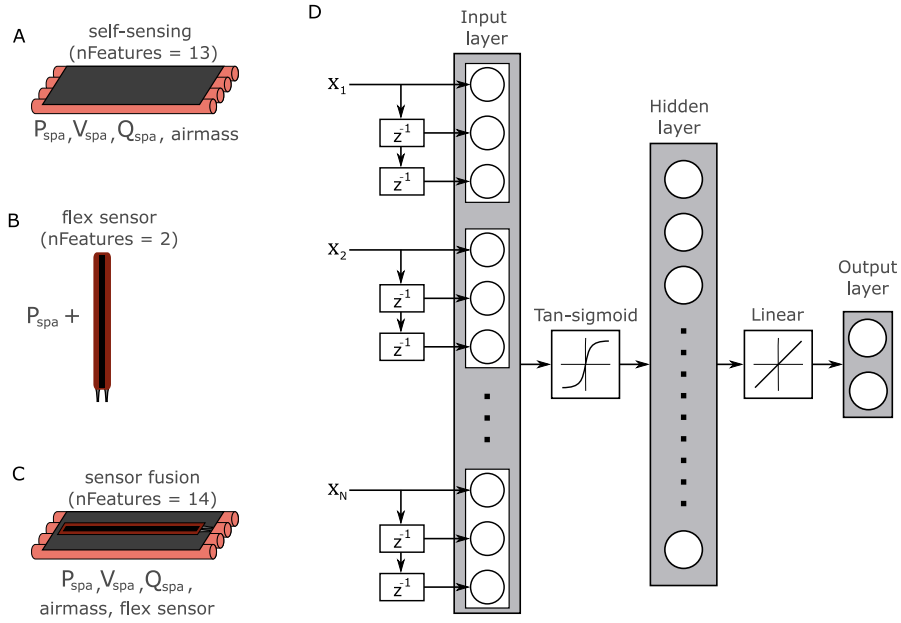


Figure 4.6: Neural network architectures used in this study. (A) Self-sensing, consisting of 13 input features containing information about SPA pressure, volume, flow and airmass, (B) Flex sensor, which uses SPA pressure and flex sensor reading as input features, (C) sensor fusion, that uses the 13 input features of sensorless estimation as well as flex sensor reading. (D) General architecture of the time-delay neural network consisting of an input layer, hidden layer and an output layer. In addition to the features of the current time-step, the input layer includes previous feature values up to two time-steps. The hidden layer consists of either 4, 8, 12 or 16 neurons. With the three types of input feature sets, we have a total of 12 neural network architectures. The output layer consists of force and displacement. The activation functions are tan-sigmoid between the input and hidden layers, and linear between the hidden and output layers.

4.4.2 Training the neural networks

We first divided the data from each loading scenario into training and testing sets as shown in Table 4.2:

Table 4.2: Data partitioning into training and testing sets

Loading sequence	Training	Testing
<i>hold</i>	15 min	4 min
<i>step</i>	2 min	0.5 min
<i>cyclic</i>	20 min	5 min
<i>random</i>	75 min.	25 min.

For training the data, we used the Levenberg-Marquardt algorithm and a total of 1000 epochs. During training, the MATLAB deep learning toolbox further split the data as 70% for training, 15% for validation and 15% for testing. To prevent overfitting, training was stopped if the validation error failed to decrease for six iterations. After training, each neural network was implemented on the testing data, comprising of previously unseen data.

4.5 Results and discussion

Here, we analyzed the estimation accuracy of the three estimation strategies, and how it was affected for the different anchoring conditions, loading sequences and hidden layer size. From Figs. 4.7 to 4.12, the blue curves correspond to ground truth values, and the remaining correspond to the estimated values using the three strategies: sensorless estimation (yellow), flex sensor (violet) and sensor fusion (green). For pulling force, Figs. 4.7 and 4.8 compare the ground truth vs. estimated force and displacement respectively, of the best performing feature neural nets for the three estimation strategies. Similarly, Figs. 4.9 and 4.10 compare results for three-point bending. Figs. 4.11 and 4.12 show the root mean squares (rms) and standard deviation (sd) of the errors for the 12 neural net architectures used for pulling and three-point bending respectively.

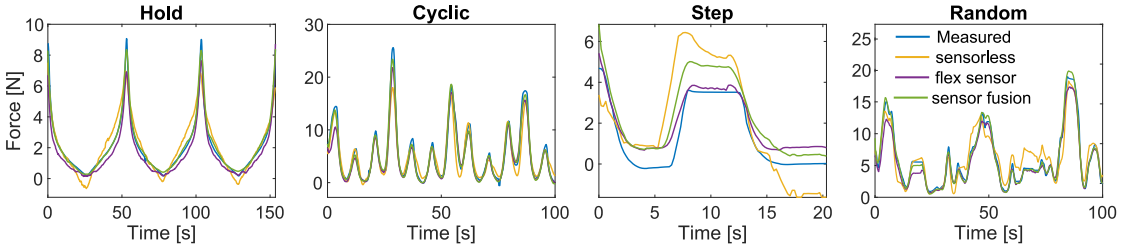


Figure 4.7: Force estimation for pulling with previously unseen data using the three estimation strategies and four loading sequences. While sensorless estimation is not the best performing approach, we see good agreement with the ground truth values. The best results are with sensor fusion, which combines data from the other two estimation strategies. We also see that the estimation accuracies are in the following order of decreasing magnitude: *hold*, *cyclic*, *random*, *step*.

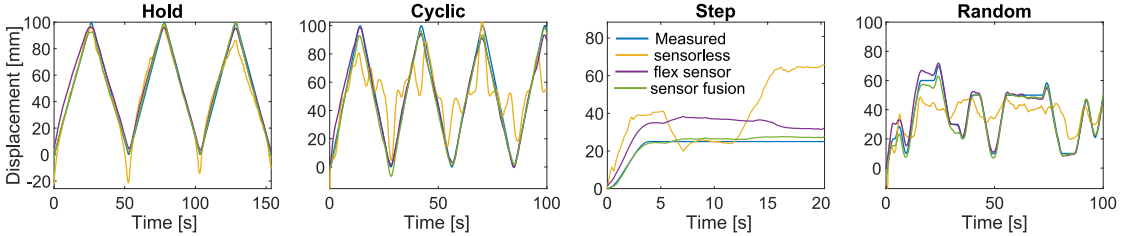


Figure 4.8: Displacement estimation for pulling with previously unseen data using the three estimation strategies and four loading sequences. We observe similar results as those for force estimation, with sensor fusion showing highest accuracy, followed by flex sensor and sensorless estimation. Compared to force estimation, the differences between sensorless estimation and the other two approaches are higher for displacement estimation.

4.5.1 Effect of estimation strategy

1. **Sensorless:** For many of the graphs from Figs. 4.7 to 4.10, we observe good agreement between the ground truth values and the estimated values. These results demonstrate for the first time that data solely from pressure sensors can be intelligently used to extract information about the SPA, not just for simple loading sequences such as *hold*, but also for complex ones

such as *random*. For the best performing neural net, the rms errors are 1.81N and 19.4mm for pulling and 2.61N and 10.3mm for three-point bending respectively. This establishes that, at least for the considered SPA and loading condition, a mathematically well-defined relationship exists between the mechanical outputs and pneumatic inputs. At the same time, however, we also observe large estimation errors with only a qualitative trend, especially for step and random loading sequences. Furthermore, we observe that the estimation error gradually increases over time, which can be attributed to integration drifts from Eq. 4.2 and 4.3. These results suggest that sensorless estimation can be a viable option for SPAs, but more investigation is required for improving estimation accuracy.

2. **Flex sensor:** This corresponds to the conventionally used estimation strategy of combining pressure sensor data with a displacement sensor. We see that the addition of a displacement sensor to the SPA shows an improvement in estimation accuracy. The rms errors are 0.91N and 5.7mm for pulling and 1.29N and 3.3mm for three-point bending. Another aspect to notice is that the difference between sensorless estimation and conventional sensing is higher for displacement estimation. This is expected because the flex sensor data is a direct measurement of the displacement, whereas force estimation is done indirectly.

3. **Sensor fusion:** This corresponds to the combination of sensorless estimation with conventional sensing. From the figures, we see that the estimation accuracy of both force and displacement increases with sensor fusion. Especially from the error bars of Figs. 4.11 and 4.12, we notice that the lowest rms and sd error for virtually all hidden layer sizes is minimum for the sensor fusion approach. Therefore, for existing SPA-based devices containing displacement sensors, we can expect an improved estimation accuracy combining them with sensorless estimation, without any changes in the hardware. For the best performing case, the rms errors are 0.76N and 2.94mm for pulling, and 1.21N and 3.15mm for three-point bending.

4.5.2 Effect of number of hidden neurons

The number of neurons is directly related to the complexity of the model fitted by the neural network. For all hidden layer sizes and all estimation approaches, the training errors decreased with an increase in the number of neurons as the neural net is able to better fit to the measured data. During testing, however, the errors are prone to increase due to overfitting. For sensorless estimation, we observe from Figs. 4.11 and 4.12, either improved accuracy or overfitting for

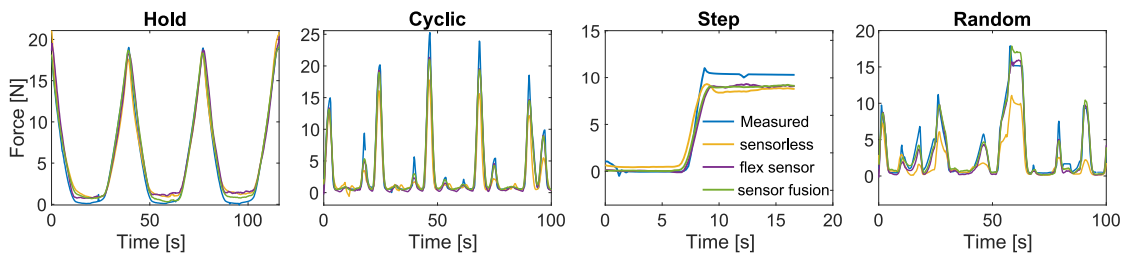


Figure 4.9: Force estimation for three-point bending with previously unseen data using the three estimation strategies and four loading sequences. We again find similar results as those for pulling, with highest accuracy in sensor-fusion.

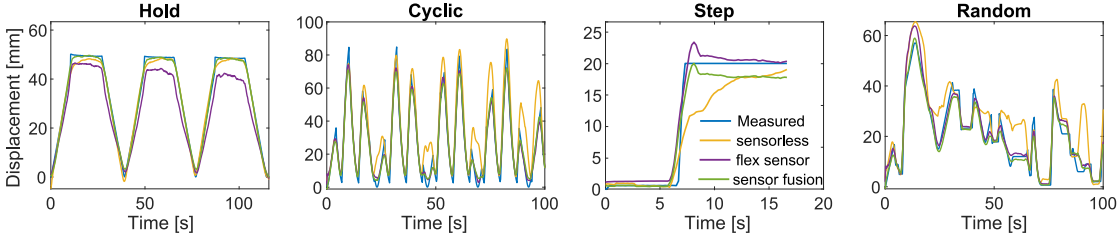


Figure 4.10: Displacement estimation for three-point bending with previously unseen data using the three estimation strategies and four loading sequences. Here we see good agreement with ground truth values for all estimation approaches and loading sequences.

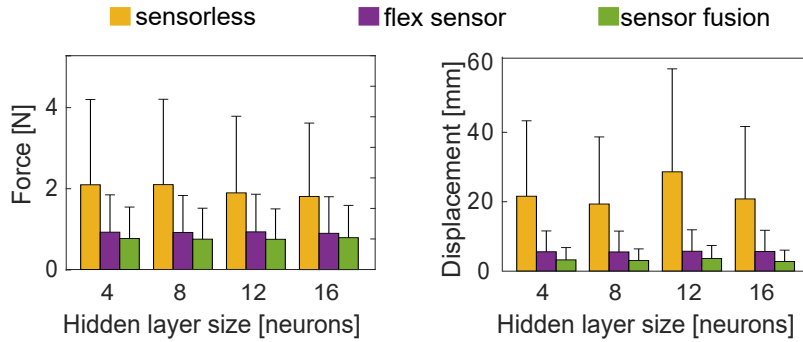


Figure 4.11: Error bars for force and displacement estimation of the 12 neural net architectures, for the anchoring condition: Pulling. In sensorless estimation, we see an increase in accuracy in force estimation, and overfitting for displacement estimation with an increase in the number of hidden neurons. For the other two approaches, there is very little effect of the number of neurons. Here we also see a significant and consistent improvement by using sensor fusion.

different cases, with increasing number of hidden neurons. For the flex sensor and sensor fusion approaches, this did not show significant differences.

4.5.3 Effect of loading conditions

The loading conditions can be divided based on their anchoring conditions: pulling and three-point bending; and loading sequences: *hold*, *cyclic*, *step*, *random*. With respect to the anchoring conditions, we found slightly better accuracies in force estimation during pulling, and for displacement estimation during three-point bending. For three-point bending, factors such as making and breaking of contact, slack in the fabric and friction at the cantilever attachment are likely sources of increased force estimation errors. On the contrary, a possible reason for improved displacement accuracy in this loading condition could be attributed to the regions of free-displacement, where the displacement depends only on the pressure. We also discover that the differences between flex sensor and sensor fusion are more pronounced in pulling than in three-point bending.

The estimation accuracy showed considerably larger differences with respect to the loading sequences. For all estimation approaches, accuracy was in the following sequence of decreasing magnitude: *hold*, *cyclic*, *random* and *step*. The poorer accuracy for *step* can be attributed to

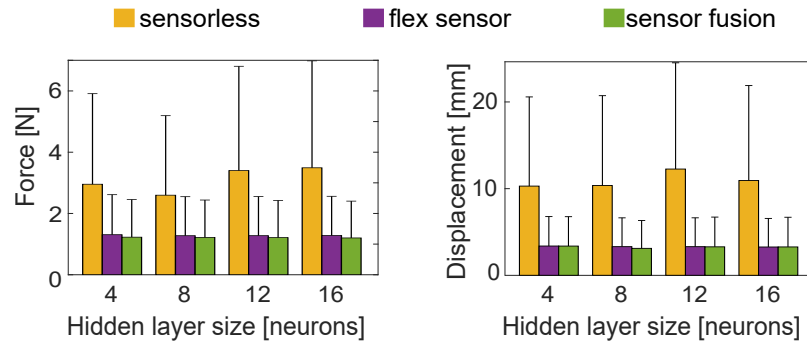


Figure 4.12: Error bars for force and displacement estimation of the 12 neural net architectures, for the anchoring condition: Three-point bending. In sensorless estimation, we see an initial increase in accuracy followed by overfitting, with increase in number of hidden neurons. For the other two approaches, there is very little effect of the number of neurons. Here as well, we see an improvement in accuracy for sensor-fusion, but the difference is not as pronounced as that for pulling.

the comparatively less data (2 mins) out of the total 112 min. Another potential reason for the low accuracy is that the SPA displacement was enforced in its deflated state, which led to only slight changes in the pressure, difficult to detect using the sensorless estimation approach.

4.6 Discussion

In this chapter, we presented a new concept to estimate force and displacement of SPAs without requiring dedicated sensors. This sensorless estimation method is based on the idea that SPA pressure, flow, air mass and volume data could be used to extract information about how the SPA is interacting with its environment. The only sensors used in this approach were the pressure sensors for the SPA and pneumatic source, which are readily present in existing devices. The proposed experimental protocol, consisting largely of randomized loading sequences, helped to validate that sensorless estimation can consistently predict force and displacement under diverse loading conditions. Predictions with sensorless estimation showed qualitative to good agreement with the measured ground truth values with under 10 and 20% rms errors for force and displacement estimation respectively. These results represent the first application and experimental validation of sensorless estimation in SPAs. Even though estimation accuracy for sensorless estimation was slightly lesser than that using a conventional flex sensor, combining the data from the two increased accuracy in all tested conditions as it provides additional information via sensing redundancy. While we used a bending SPA here, this method could be used for any pneumatic actuator, soft or rigid, and any type of motion as it depends only on the pressure, flow and volume dynamics. For systems without dedicated sensors, this method enables SPA displacement and force estimation and can be used for sensorless control, which was not possible previously. For SPAs containing displacement sensors, sensor fusion with sensorless estimation can be implemented to further improve accuracy or possibly for sensing multiple displacement modes such as simultaneous bending and extension. Lastly, the experimental protocol used in this study can be applied for characterizing and testing other sensors for soft robots, as it enables well-defined and

repeatable loading conditions which more closely recreates the intended application.

While our results corroborate the feasibility of sensorless estimation for the specific SPA and loading conditions, a general conclusion cannot be yet made. The primary reason for this is because sensorless estimation will work only if there exists a mathematically well-defined relationship between the mechanical outputs and the pneumatic inputs. Future studies could conduct a more theoretical study of sensorless estimation in pneumatic actuators and investigate the validity of this assumption. Another future direction could be to address integration drift, which was one of the sources of errors in the current study.

5 Design and biomechanical analysis of soft exosuit for the human torso

In the previous chapters, we quantified the static and dynamic performance of SPAs, and demonstrated optimization of the pneumatic supply system in order to meet desired SPA performance and PSS requirements such as size, mass, and air and energy consumption. However, a fundamental part that determines the impact of soft wearable robots is their effect on the biomechanics of the user. When providing the desired forces or moments across the human joints, soft wearable robots use the wearer's body as the primary structure to transmit forces. As a result, it becomes crucial to assess the complete effect of such devices so as to judge the beneficial or detrimental effects, if any, and develop the appropriate design or control strategies. This becomes even more important when the device applies large forces on the body, or acts on sensitive locations such as the spine. In this chapter, we address this requirement via the design, modelling, and testing of a soft exosuit for assisting the human torso.

5.1 Introduction

The human torso is subject to considerable mechanical effort in occupations involving awkward postures and handling heavy loads, for example, in construction, industrial workplaces or nursing [138; 139; 140]. Even when handled by the upper limbs, the muscles of the torso need to be constantly active for stabilizing the body, supporting the load, and transferring forces to the ground. This often leads to pain in the lower back pain, neck and shoulder, increased occurrence of injuries, and negatively impacts the quality of life of the workers. One possible way to address this problem is through wearable assistive devices, which apply forces externally on the body and share some of the load taken by the muscles.

Several researchers have designed devices for assisting the torso during forward bending and lifting. Many of these devices consist of a rigid frame comprising of a torso section and a thigh section connected at the hip joint, powered by either passive elastic elements [141; 142; 143; 144; 145; 146; 147; 105; 148; 149; 150] or active components such as electric motors [106; 151; 152; 104; 153; 108; 154; 155; 173] or pneumatic actuators [156]. Recently there

has been an increase in the development of soft assistive devices or exosuits, designed using fabric or other compliant materials, that rely on the wearer's body for structural support and act as external muscles. Existing soft exosuits for the torso usually consist of an upper shoulder section and a thigh section connected with tension generating elements such as passive elastic bands [157; 158; 159; 160; 161; 162; 163] or active cable-driven actuators [164] which act in parallel to the muscles of the back. Subject trials with both rigid and soft devices have shown considerable reductions in the measured values of perceived load, electromyographic (EMG) activity of back and abdominal muscles, fatigue and metabolic rate while using assistive devices during static bending or lifting tasks. Some studies have additionally reported reduced moment loads at the hip or lumbo-sacral (L5/S1) joint using rigid multi-body models for the torso, and reduced muscle forces and compression on the L5/S1 joint, calculated using EMG-driven models.

Although these studies demonstrate the effectiveness of torso assistive devices, there still remain challenges and knowledge gaps that need to be addressed. Firstly, existing studies do not provide the complete picture of the effect of wearable assistive devices on the torso. Most studies evaluate their devices by measuring EMG of the back extensor muscles, in particular, the erector spinae. This muscle, however, is a collection of several muscles, namely iliocostalis, longissimus and spinalis, each of which can be further sub-divided based on their origin and insertion points. Surface EMG, which measures local excitation at a limited number of locations, is insufficient to convey the individual muscle activity. Also, surface EMG is prone to errors due to noise, cross-talk between different muscles, imprecise electrode placement, and is challenging for deeper muscles such as the multifidus [174]. Other than the kinematics, EMG and metabolic rate, other metrics such as compressive, shear and moment loading on the vertebral joints can help to understand the overall effect of the assistive device. However, it is difficult to assess these metrics reliably with existing methods. As a consequence, it is not possible to evaluate how much a device is truly offloading the back or redistributing the load, for e.g. from the superficial muscles to the deeper ones, or redirecting the compressive and shear loads across the intervertebral joints. Lastly, existing methods for evaluation are time-consuming and require special training and equipment such as motion capture, force plates, EMG, and gas calorimetry systems. This slows the initial design and evaluation phases of torso assistive devices leading to slower iterations. In addition to evaluation methods, torso assistive devices also face design challenges due to the redundant kinematics of the spine and relative trade-offs between rigid and soft assistive devices. Rigid devices tend to be bulky in size and weight, and their kinematics are not fully compatible with those of the torso, thereby constraining the natural motion of the wearer. While soft exosuits bypass these limitations, it is difficult to measure or model their interaction forces because they are distributed over large surfaces and the force magnitude depends on the location, tightness of fit, friction, and skin elasticity. Lastly, while manual material handling tasks are combinations of forward and lateral bending and twisting of the torso, most studies have only focussed on forward bending assistance. Thus, there is a need to investigate new methods for design and evaluation of torso assistance devices that will supplement the knowledge from previous studies.

Here, we address the above challenges via the design, modelling, testing and biomechanical evaluation of a soft reconfigurable exosuit. We first present our soft exosuit design, which is in the form of a vest or jacket and consists of SPAs placed flat on the body, overlapped by fabric and nylon webbing. Depending on the application, the SPAs and webbing can be reconfigured so as to provide assistance in different tasks such as forward bending, lateral bending, and posture support. We present two iterations of the exosuit, an initial design that contained the SPA-packs studied in previous chapters, and an updated final design that contained high force, low-profile pouch-type SPAs. We test the final exosuit in forward bending assistance with two subjects and measure the SPA interaction forces at seven static angles. We then develop an exosuit-human model, by resolving the measured SPA interaction forces into tension vectors in the exosuit straps and applying them on a musculoskeletal model of the torso. Via simulations, we calculate the effect of the exosuit on six muscle groups and on the compressive, shear and moment loading on the inter-vertebral joints. Results show that the exosuit significantly offloads many of the torso muscles and inter-vertebral joints, especially for the lumbar vertebrae at large bending angles. At the same time, the results also depict that some of the torso loading gets redistributed, particularly from superficial to deeper muscles and from lumbar to upper thoracic vertebrae. These results, for the first time, provide such an in-depth assessment of torso assistive devices and highlight the interesting trends of how a wearable assistive device affects the muscles and joints of the torso. The presented design, modelling, and evaluation methods are readily adaptable to other torso assistance devices and can be used to develop, compare, and optimize them and their control strategies.

5.2 Design and evaluation strategies for soft reconfigurable exosuit

While significant progress has been made, there are still some challenges in the design and evaluation of torso assistive devices as detailed in Section 5.1. Here, we address these challenges by designing a soft exosuit and developing a biomechanical exosuit-human model for simulation, analysis and evaluation.

5.2.1 Soft exosuit design

The requirements for effective wearable assistive devices include: sufficiently large force/-moment and displacement capacity across the joints, low weight, low-profile design, well-distributed forces on the body, minimal shear forces, kinematic compatibility with biological joints, and transparency when not in use [165]. A soft exosuit, made using compliant and fabric-based components could potentially address many of these requirements. One of the early attempts towards such a soft assistive device for the torso was the SPA-belt as depicted in Fig. 5.1A, and described in Robertson and Paik [23]. Weighing 1.3 kg, this device consisted of four SPA-packs placed laterally around the hip, and fastened onto the waist using an elastic and nylon belt. When pressurized, the SPA-packs bend inwards to push and support the torso in lateral bending. However, the device only applied forces to the lower spine (L3 to S1) and

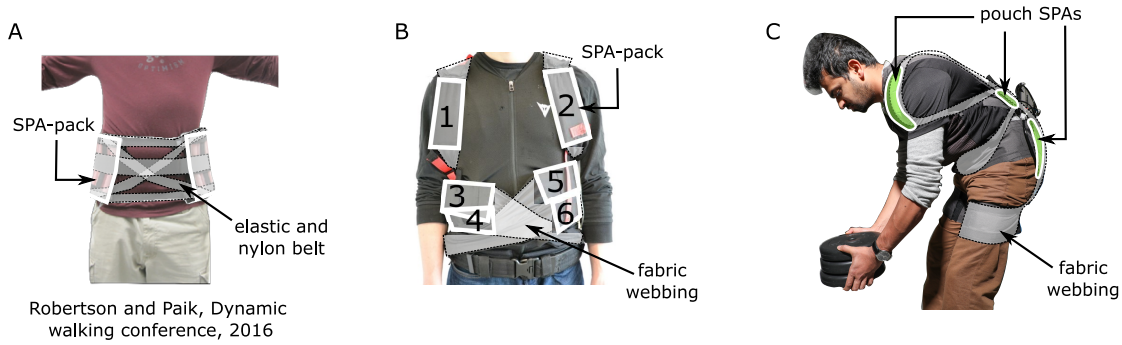


Figure 5.1: Different versions of the soft torso assistive device. (A) The SPA-belt by Robertson and Paik [23]. It provides lateral bending assistance. (B) Initial version of the torso exosuit presented in this thesis. It consists of six SPA-packs placed flat on the torso and overlapped by fabric webbing, which is anchored at the waist. It provides forward and lateral bending assistance. (C) The final version of the torso exosuit presented in this thesis. It consists of pouch-type SPAs also overlapped by fabric webbing, which is anchored at the waist and thigh. It provides forward bending assistance.

the elastic belt added to series elasticity that reduced the device-human interaction force. Therefore, it could not provide sufficient force for assisting the user.

Here, we present two design iterations of a soft reconfigurable exosuit. The design principle behind both these designs is to place SPAs flat on the body and overlap them with fabric or nylon webbing, routed and anchored strategically on the torso so as to produce an assistive moment on the entire spine.

Initial design: SPA-pack based torso exosuit

The initial design of the soft exosuit is shown in Figs. 5.1B and 5.2A, and consists of six SPA-packs, two on the shoulders, and two each on the lateral sides of the abdomen. They are loosely held on a spandex jacket and overlapped by fabric webbing as seen in the figure. They are powered by the wearable and portable PSS as shown in Fig. 5.2B, which was designed and optimized in Section 3.4. The total exosuit weight, including SPAs and portable PSS is 3.7 kg.

When pressurized, the SPA-packs on the shoulders push the shoulders behind, and generate tension in the fabric webbing in order to create a net extension moment on the spine, as shown in Fig. 5.2D. Similarly, the two SPAs on either side push into the lateral side of the rib and pull on the fabric webbing that pull the wearer from a bent position to an upright position as shown in Fig. 5.2E. The appropriate loading condition and corresponding force and displacement capacity of each SPA when powered at different pressures is depicted in Fig. 5.2F. Similarly, Fig. 5.2C shows the SPA-pack dynamic response in inflation and deflation. Combining the loading condition, mechanical characterization, and pressure dynamics, we can estimate the interaction forces and SPA displacement via sensorless estimation as detailed in Chapter 4. We implemented three levels of control in the entire system:

- Low-level pressure control: We measure the SPA pressure using pressure sensors, and

5.2. Design and evaluation strategies for soft reconfigurable exosuit

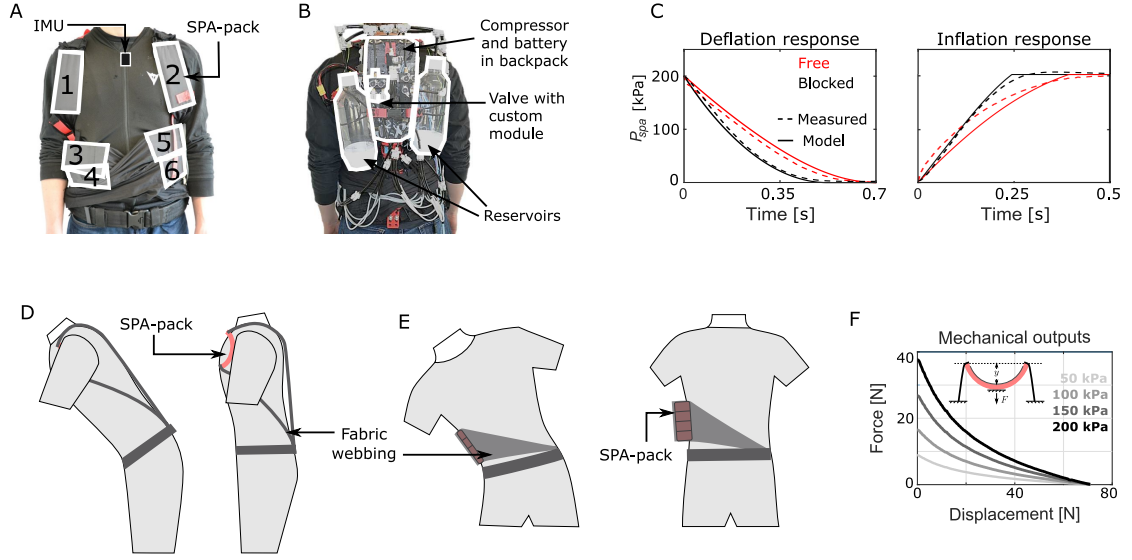


Figure 5.2: The initial design of the soft exosuit for assisting the torso. (A) The fabricated prototype for forward and lateral bending assistance. It consists of six SPA-packs placed flat on the body, overlapped by fabric straps that help to hold the SPAs against the body, and transmit the forces to different regions around the torso. It also consists of an IMU to measure the orientation of the torso, which is used for high-level control of the SPAs, (B) The wearable and portable PSS, designed to power the exosuit for up to 1 hour of continuous use. As described in Section 3.4, the PSS was optimized for minimum mass of components while meeting dynamic performance requirements, (C) Dynamic response characterization of the SPA-pack, powered by the wearable and portable PSS, (D) Schematic showing the exosuit configured in forward bending assistance, (E) Schematic showing the exosuit configured for lateral bending assistance, (F) Mechanical outputs characterization of the SPA-packs in the loading condition, three-point bending, as described in Section 4.3.

control it by switching the corresponding valve states to INFLATE, DEFLATE, or HOLD. We kept an error margin of 5 kPa to prevent excessive switching of the valves.

- **High-level actuation control:** For controlling which SPA to power, we affix an inertial measurement unit (IMU) to the chest of the wearer as shown in Fig. 5.2A that measures the forward and lateral bending of the torso. We implement a simple control algorithm that powers SPAs 1 and 2 when the forward bending angle is over 10 degrees. Similarly, when the lateral bending angle is over 5 degrees, SPAs 3 and 4, or 5 and 6 are powered, depending on the direction of bending.
- **Compressor control:** We first set an upper and lower limit on the reservoir pressure. Then, we used pressure sensor feedback to switch ON the compressor if the reservoir pressure is below the lower limit, and switch OFF if it is above the upper limit.

This exosuit represents a complete wearable assistive device that includes actuation, power, sensing, and control. From our pilot testing, however, it was observed that this exosuit could not generate sufficient assistive moment to the user. This was due to the relatively low force capacity of the SPAs, high compliance at the human-exosuit interface, and the weight of the portable PSS which negated some of the assistive moment of the exosuit. At the same time,

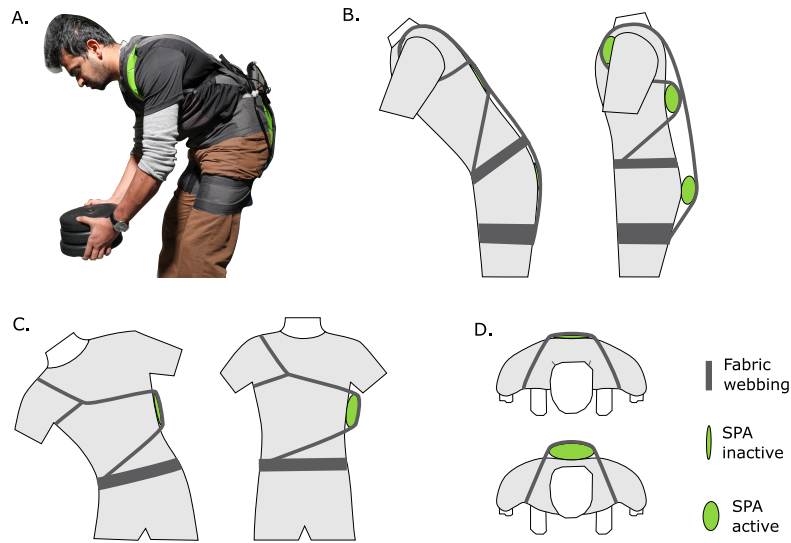


Figure 5.3: The final design of soft exosuit for assisting the torso. It consists of pouch-type SPAs placed flat on the body, overlapped by fabric straps that help to hold the SPAs against the body, and transmit the forces to different regions around the torso. By strategically routing the anchoring and routing points, this design can be reconfigured to provide assistance in different motions. (A) The fabricated prototype for forward bending assistance, (B) Schematic showing the exosuit configured in forward bending assistance, (C) Schematic showing the exosuit configured in lateral bending assistance, (D) Schematic showing the exosuit configured for posture assistance.

however, we gained valuable insights from this design, most important being:

- Since forward bending is a combination of motion at the spine and hip, the webbing must cross the joints of both.
- Compliance in the exosuit-human interface acts as series elasticity and reduces both, interaction force and bandwidth
- Friction between the exosuit and its wearer leads to undesirable shear forces on the skin. They can be reduced by choosing low-friction materials.
- Friction can also be reduced by routing the webbing such that at any overlapping section, the resultant of tension forces acts somewhat normally to the user's body.

Final design: SPA-pouch based torso exosuit

Using the insights and experience from the initial version of the soft exosuit, we updated and improved the design and developed the soft exosuit as shown in Figs. 5.1C and 5.3. The design strategy for this exosuit consists of low-weight, high-force pouch-type SPAs placed directly on the torso and an overlapping nylon webbing layer. The SPAs are flat when unpowered, bulge out when pressurized, and push out on the webbing. This generates tension in the inextensible webbing, which generates a net moment on the spine. Furthermore, when the pouch-type SPA

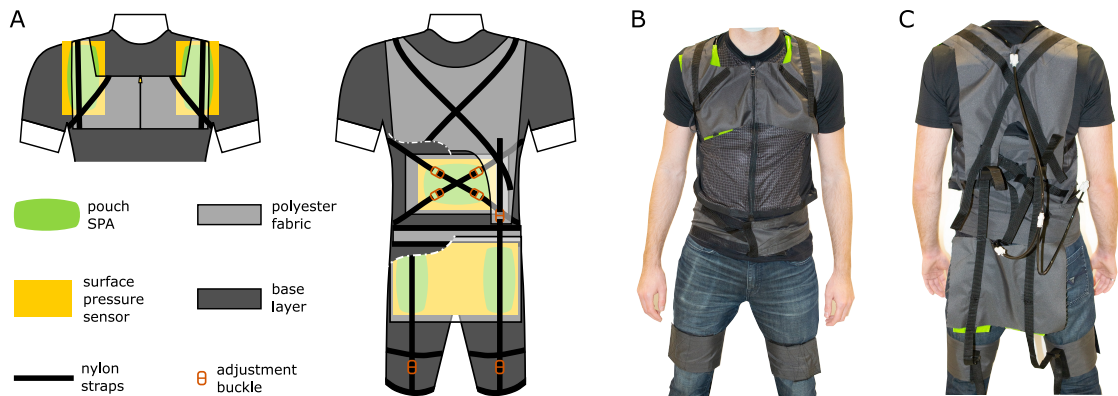


Figure 5.4: Design of the exosuit: (A) Schematic showing different layers of the exosuit. It consists of (i) an inner base layer for holding all other layers, (ii) an SPA layer that generates the forces, (iii) a polyester fabric layer reinforced by nylon webbing that transmits the forces to the body, and (iv) a pressure sensing layer that measures interaction forces. Some sections from the back side are cut out in the figure to show the inner layers. (B) Fabricated prototype (front view), (C) Fabricated prototype (back view)

expands, it pushes the webbing away from the spine, thereby increasing the moment arm of the tension forces. This helps to generate a large moment on the spine with lower magnitude of tension, which is expected to reduce spinal loading, similar to the passive exosuit by Lamers and Zelik [163]. Based on this design strategy, we outlined three configurations of this exosuit for forward bending assistance, lateral bending assistance and posture support as shown in Fig. 5.3B, C, and D respectively. These can be achieved by rearranging the locations of the webbing and the SPAs, making it a reconfigurable soft exosuit.

Among these three, we focussed on forward bending support in this study and designed the exosuit as shown in Fig. 5.3A and B. It consists of inextensible webbing that overlaps pouch-type SPAs placed on the chest, lower back, and lower hip. The webbing is anchored on the waist and thigh, and routed in the following sequence: anterior side of the waist - lower back SPA - chest SPA - over the shoulders - hip SPA - thigh. When powered, the SPA and webbing on the back generate an extensor moment on the spine. Similarly the SPA and webbing on the lower hips generate an extensor moment on the hip joints. The chest SPA is placed at the connection of these two sections and acts like a tensioner pulley that increases the overall tension in the webbing. We fabricated the exosuit in four layers as shown in Fig. 5.4, as follows:

- Inner base layer: This is the structural layer in the form of a spandex jacket that holds all other components together. Its low friction also allows the webbing to slide freely, helping to reduce shear forces on the skin.
- SPAs: This is the force generating layer consisting of pouch-type SPAs, which inflate and push against the user when pressurized, as shown in Fig. 5.4. We fabricate them via heat-sealing of TPU-coated nylon fabric. The SPAs measure 10 x 20 cm and 500 microns thick when completely flat, bulge out to form a cylindrical shape of around 6.4 cm when

pressurized and can bear pressures up to 100 kPa. We place two SPAs on the chest, one on the lower back, and two on the lower hip.

- Outer webbing layer: This is the force transmission layer, and consists of polyester sections reinforced by nylon webbing, overlapping the SPAs and torso.
- Sensing layer: This is an additional layer consisting of pressure-sensing array sensors placed between the SPAs and base layer as shown in Fig. 5.4. These sensors, as shown in Fig. A6 allow us to measure the interaction pressure and forces applied by the SPAs on the wearer.

To don the exosuit, the inner base layer is first worn as a jacket or vest, and the outer fabric layer is then strapped on the waist and thighs using Velcro. The SPAs are attached to the outer layer also with Velcro. The locations of the SPAs and length of the nylon webbing can be adjusted, which helps to customize the exosuit to the user. Fig.5.3A shows the fabricated exosuit worn by a user. The total weight of the exosuit is 0.82 kg without the sensors and 1.45 kg with the sensors.

Summary

Table 5.1: Comparison of the SPA-belt with the two presented exosuit designs

	SPA-belt	Initial exosuit design	Final exosuit design
Assists in	Lateral bending	Forward/lateral bending	Forward bending
Acting on	L3 to S1	Entire spine	Entire spine and hip joint
Actuation	4 SPA-packs (35 N each)	6 SPA-packs (35 N each)	5 pouch-type SPAs (350 N each)
Power	Off-board	On-board PSS	Off-board
Sensing	-	IMUs for bending angle, sensorless force estimation	IMUs for bending angle, pressure sensing arrays
Control	Manual	IMU-based	Manual
Mass	1.3 kg	3.7 kg	0.8 kg

Table 5.1 compares the two presented exosuit designs with the SPA-belt. We see that the initial version of the exosuit is the most complete version, and contains on-board actuation, power, sensing, and control. Its force capacity, however, is small and it acts only on the spine making it insufficient to assist the torso in forward bending. The final exosuit design addresses this limitation by having high-force SPAs and webbing that crosses the spine as well as hip joints. We hypothesize that this design should be able to support the wearer, and therefore choose this exosuit for our biomechanical analysis. In the forthcoming sections, **any reference to 'exosuit' will refer to the final version of the exosuit** unless specified otherwise.

5.2.2 Evaluation methods

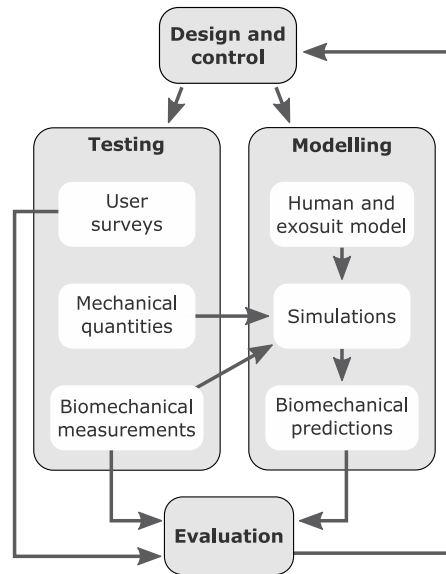


Figure 5.5: Flow chart depicting the various stages of wearable robot development. Once designed, the device can be evaluated either using (i) user surveys, (ii) measurement of biomechanical quantities like muscle activity or heart rate, and (iii) predictions using biomechanics model of the human-exosuit. The evaluation results can be fed back to the initial stage for further iterations in design and control.

The various phases in the development of wearable assistive devices are depicted in Fig. 5.5. After defining the design and control strategy, the device is evaluated using experimental testing and/or predictions through modelling. Various testing methods involve measurement of three types of metrics [165]: (i) user surveys, which include subjective questionnaires, (ii) measurement of biomechanical values, such as EMG activity of targetted muscles, metabolic rate, heart rate, blood pressure, blood oxygen levels and so on, and (iii) predictions of biomechanical metrics such as muscle forces, joint moments, and bone-on-bone loading at the joints, using biomechanics models. All the three methods are complementary to each other and together develop a comprehensive understanding of how the device affects the user.

Although user studies and biomechanical measurements have been carried out extensively in torso assistance devices, biomechanical modelling has not been investigated in detail. The most commonly used models lump the thigh and torso into two or three rigid links, and use forward or inverse dynamics to estimate the impact of their assistive device on the joint moments. Some studies also report force estimates of superficial back muscles and L5/S1 loading using EMG-driven models. However, these models are not sufficient to evaluate the effect of their devices on forces of the various groups and sub-groups of torso muscles or compressive and shear loading on the different vertebrae. Here, we address this research gap and develop a comprehensive exosuit-human biomechanical model for the presented soft exosuit. After defining the model, we conduct experiments with two subjects and measure the interaction forces applied by the exosuit SPAs at different bending angles, using surface pressure sensing arrays placed under the SPA layer. We then carry out an inverse biomechanics

simulation by inputting the measured force and kinematic values, so as to calculate predicted loading on the muscles and joints.

5.3 Biomechanical modelling of the exosuit

We model the soft exosuit by calculating the tension force vectors in its different straps and applying them on a musculoskeletal model of the torso.

5.3.1 Torso musculoskeletal model

We use a modified version of the thoracolumbar spine and rib cage model by Bruno et al. [166]. It consists of individual segments for each of the vertebrae, ribs, shoulder complex, neck, head, pelvis and thigh. It has 93 degrees-of-freedom (DoF) of motion and consists of 552 musculotendon actuators modelled using the Thelen muscle model [167]. Out of the 93 DoF, 51 correspond to the vertebrae, 12 thoracic and 5 lumbar, each with 3 DoF corresponding to flexion-extension, lateral bending and axial twisting. The remaining DoF correspond to motions of the head and neck, abdomen, arms, pelvis-ground, and individual ribs. To this model, we appended two segments corresponding to the left and right thigh, and three DoF each for hip rotation. Additional information about this model can be found in [166].

During forward bending of the torso, motion at the spine and hip joints is in only one axis of rotation. Therefore, we only consider 20 out of the 99 DoF, corresponding to flexion-extension of the 17 vertebrae, two hip joints, and pelvis rotation with respect to the ground. Furthermore, we describe the overall motion of the torso using a single forward bending angle as the cumulative sum of the flexion-extension from the thigh to T1 vertebra. We calculate the individual vertebrae and hip angles as proportions of this overall torso angle using the Tables S1 and S2 as described in Bruno et al. [166]. To visualize this musculoskeletal model, and perform kinematic and kinetic analysis, we use OpenSim, an open-source platform for musculoskeletal modelling and analysis [168].

5.3.2 Exosuit model

The effect of the exosuit on its user is because of the forces it applies on the wearer at all the contact locations. These interaction forces can be calculated using the tension forces developed in the straps throughout the exosuit. Here, we develop the final exosuit-human model by calculating these tension forces and modelling them in the musculoskeletal torso model described in Section 5.3.1.

We first place a set of virtual markers on the musculoskeletal model, along the routing of the exosuit straps as shown in Fig. 5.6. We determined these locations by measuring the bony landmarks on the collar bones, ribs, spine, iliac crest, and the thigh. Since we only consider flexion-extension, we placed the markers in the sagittal plane, which is the 2-D plane

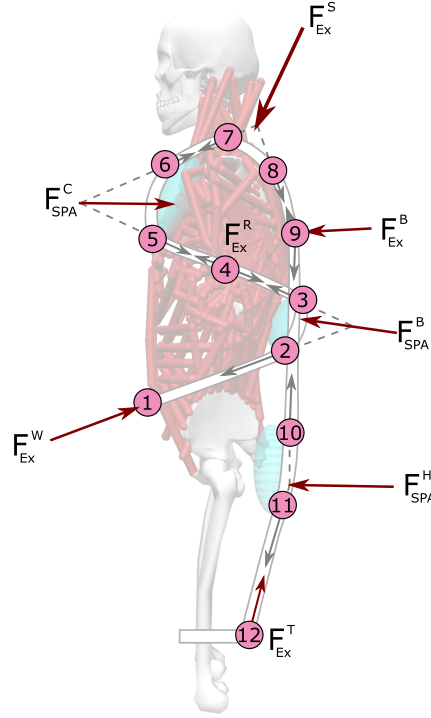


Figure 5.6: Forces applied by the exosuit. The two main sources of the exosuit forces are the SPAs and the tension in the fabric straps. We resolve these forces and apply them at the corresponding location in the musculoskeletal model.

that splits the body into left and right halves. Starting from marker 1 at the waist, the virtual markers are placed along the lower back (2 and 3), ribs (4) chest (5 and 6), shoulders (7 and 8), upper back (9), hip (10 and 11) and thigh (12) as shown in Fig. 5.6. We fix these markers to appropriate body segments so that the markers move along with the musculoskeletal model. Segments formed by connecting any two successive markers represent sections of the exosuit straps. This gives us a set of vectors that move with the musculoskeletal model and represent the force vectors of the tension in the exosuit straps. Next, we group the strap tensions into eight resultant forces as shown in Fig. 5.6 and Table 5.2. The first three forces of Table 5.2 represent the interaction forces of the SPA at the chest, back, and hip. As mentioned previously, we experimentally measure these interaction forces using surface pressure sensing arrays. In order to resolve the exosuit strap tensions from the measured SPA interaction forces, we make certain assumptions:

- The magnitude of tension for the two strap sections overlapping an SPA are equal, i.e. $|\overrightarrow{F_{5,4}}| = |\overrightarrow{F_{6,7}}|$, $|\overrightarrow{F_{3,4}}| = |\overrightarrow{F_{2,1}}|$, $|\overrightarrow{F_{10,9}}| = |\overrightarrow{F_{11,12}}|$
- For all strap segments, $\overrightarrow{F_{i,i+1}} = -\overrightarrow{F_{i+1,i}}$
- The magnitude of tension forces is equal for upper back and the hip straps, i.e. $|\overrightarrow{F_{8,9}}| = |\overrightarrow{F_{9,10}}| = |\overrightarrow{F_{11,12}}|$

Table 5.2: Force resolution

Resultant Force	Exosuit strap tension	Acting on
F_{SPA}^C	$\vec{F}_{5,4} + \vec{F}_{6,7}$	Sternum
F_{SPA}^B	$\vec{F}_{2,1} + \vec{F}_{3,4}$	L1
F_{SPA}^H	$\vec{F}_{10,9} + \vec{F}_{11,12}$	Pelvis
F_{Ex}^W	$\vec{F}_{1,2}$	Pelvis
F_{Ex}^S	$\vec{F}_{7,6} + \vec{F}_{8,9}$	T1
F_{Ex}^B	$\vec{F}_{9,8} + \vec{F}_{9,10}$	T7
F_{Ex}^T	$\vec{F}_{12,11}$	Femur
F_{Ex}^R	$\vec{F}_{4,5} + \vec{F}_{4,3}$	Rib 9

Although these assumptions simplify the exosuit force dynamics slightly, they enable us to account for all the interaction forces applied by the exosuit on the wearer, and lead to a comprehensive model of the soft exosuit.

5.4 Testing the exosuit in forward bending support

To evaluate the effect of the soft exosuit, we tested it with two subjects in static forward bending. We measured the SPA forces, implemented them in the model described in Section III and calculated the muscle and joint loading on the spine.

5.4.1 Experimental protocol

We tested the exosuit with two healthy male subjects (S1: H = 1.82m, W = 73kg; and S2: H = 1.84m, W = 80kg) after taking informed and written consent. After donning on the exosuit, we adjusted the nylon strap lengths such that when worn and unpowered, the subjects could freely bend forward up to an angle of 90 degrees relative to upright position. We then affixed pressure sensing array mats (Sensing Tex) on the base layer of the exosuit using Velcro fasteners, just underneath the SPAs to measure the interaction forces. These consisted of two small mats (0.25 x 0.25m) with a grid of 8x8 sensors placed under each SPA on the chest, and two large mats (0.44 x 0.44m) with a grid of 16x16 sensors placed under the SPAs on the hips and back. We connected the sensing mats to a PC via USB and collected the contact pressure data with a demo software by Sensing Tex. Prior to testing, we characterized the pressure sensing arrays as described in Section A9. To measure forward bending angle, we affixed an inertial measurement unit (Adafruit 10 DoF IMU) to the sternum of the subjects using medical micropore adhesive tape. To power the SPAs, we used an external compressor and a digital pressure regulator (SMC ITV series) that maintained uniform pressure in all SPAs. We provided the subjects with a PC monitor to read their IMU-measured forward bending angle

in real-time.

We measured the SPA forces and forward bending angle for a total of seven angles: 0, 15, 30,...90 degrees; and four SPA air pressure: 5, 10, 15, 20 kPa. The test comprised of holding a certain pressure in the SPAs and gradually increasing the forward bending angle. The subjects were instructed to hold each bending angle for 10 s before proceeding to the next angle. The mean forces measured at the chest, hip and back SPAs are depicted in Fig. 5.7.

5.4.2 Modelling forces in OpenSim

After collecting the SPA force for each bending angle, we calculated the tension in the straps of the exosuit as described in Section III.B. Using the strap tensions, we calculated the eight net forces shown in Fig. 5.6 and Table 5.2. To estimate the effect of these forces on the subjects, we inputted their values in OpenSim and calculated the muscle forces, spinal loads, and moment at the hip joint for the four pressures and no exosuit conditions (zero force). The different steps carried out are as follows:

1. For each forward bending angle, we calculate and store the individual joint angles (vertebral and hip angles in sagittal plane) in separate *Kinematics.mot* files.
2. Using the OpenSim API in Matlab, we load the different *Kinematics.mot* files, simulate the joint angles in the model, and calculate the position of all virtual markers in the ground frame.
3. Using marker locations, we calculated the directions of all strap tension forces as $\vec{dir}(F_{i,j}) = pos(j) - pos(i)$.
4. Using Fig. 5.6 and Table 5.2, we resolved the measured SPA forces and calculated the magnitude and direction of the tension forces in the straps. We store these force magnitude and location vectors as columns in an *ExternalForces.mot* file.

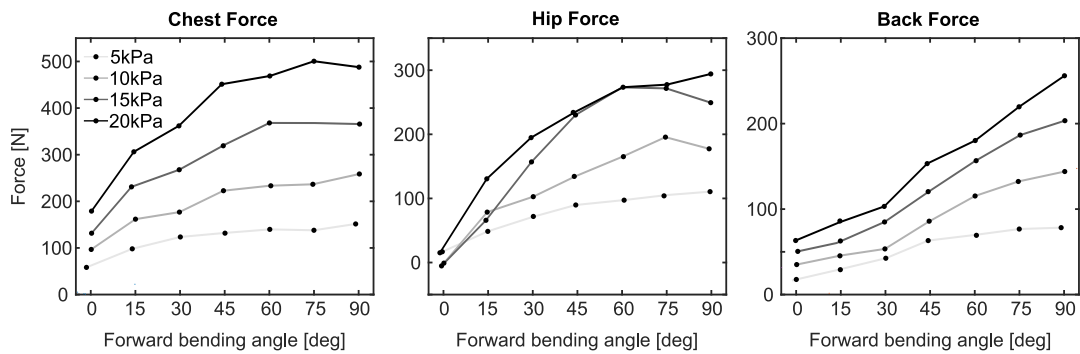


Figure 5.7: Measured interaction forces between the exosuit and subject 1 at the chest, back and hip SPAs for the seven forward bending angles and four air pressures. We see that the forces increase with increasing pressure, as expected, and also increase with bending angles. This occurs because the straps pull on the SPAs and the wearer, which compresses the SPAs, leading to higher interaction forces.

5. We create a *setup.xml* file that links the forces in the *ExternalForces.mot* file to the appropriate body segment on which the force is to be applied as given in Table 5.2.
6. We run *Static Optimization* on the OpenSim API to calculate the muscle forces. The inputs to *Static Optimization* are the *Kinematics.mot*, *ExternalForces.mot* and *setup.xml* files, and its outputs are activation values and forces of the 552 musculotendon actuators and hip moments.
7. Lastly, we run the *Joint Reaction analysis* to calculate the inter-vertebral loads in the normal and shear directions. The inputs to this process are the inputs and outputs from the *Static Optimization* analysis.

We wrote a custom Matlab script to perform the above for the 35 test conditions that included seven bending angles each for the four SPA pressures and no-exosuit condition. Lastly, to assess how the SPA forces evolve at different bending angles, we simulated a constant stiffness condition, in which the tension in all straps was assumed equal, and proportional to the forward bending angle. We chose the tension value equal to 0 N at 0 degrees, and linearly increasing with the angle, to reach a peak value of 200 N 90 degrees. This peak value is roughly equal to the tension at the chest straps ($\vec{F}_{5,4}$, $\vec{F}_{6,7}$) at 20 kPa and 90 degrees.

5.5 Results

From the testing and simulations described in Section IV, we calculated the muscle forces, spinal loads, and hip moments for static forward bending at seven angles and four conditions: no exosuit, 10 kPa, 20 kPa, and constant stiffness model. The model used in this study consists of 552 musculotendon actuators representing the individual muscle fascicles of the torso. We considered the 222 relevant fascicles out of the 552, and combined them into six major muscle groups of the torso as shown in Table 5.3. These represent the main active muscle fascicles during forward bending. Fig. 5.8 shows the muscle forces of the six muscle groups, as predicted by the simulations. Each plot is supplemented with a graphic showing the corresponding muscle group and the maximum force capacity. Fig. 5.9 shows the compression, shear and moment loading across the intervertebral joints for four forward bending angles. In all graphs, the dotted line corresponds to *no exosuit* condition, the two grey lines correspond to the exosuit powered at 10 kPa (light grey) and 20 kPa (dark grey) conditions, and the red line corresponds to the simulated constant stiffness condition.

The *erector spinae* is the main extensor of the spine, while *latissimus dorsi* acts synergistically during spine extension. From Fig. 5.8, we see that the exosuit significantly reduces the forces of these two muscle groups, thus sharing some of their load. At the same time, we also see increased effort of the *rectus abdominus* and *internal oblique* muscle groups, especially for lower bending angles. This happens because even when standing upright, the exosuit applies a net extensor moment on the spine, which is balanced by these abdominal muscles. This co-activation leads to larger compressive forces on the entire spine as seen from the upper

Table 5.3: Muscle groups and their main functions

Muscle group	function	nFascicles
Erector spinae	back extension, spinal stability	76
Multifidus	back extension, spinal stability	88
Latissimus dorsi	shoulder extension, spinal stability	28
External oblique	back flexion, transverse rotation	16
Internal oblique	back flexion, transverse rotation	12
Rectus Abdominus	back flexion, spinal stability	2

right graph of Fig. 5.9. On the other hand, the *multifidus* muscle, which is also a spine extensor shows increased loading with the exosuit. This non-intuitive behaviour can be explained by analysing the moment loading on the spine.

From Fig. 5.9, we see that although the exosuit applies a net extensor moment across the lower vertebrae, it is accompanied by a net flexor moment across the upper vertebrae. The overall effect of this is to see somewhat equal moment loading across the spine. Although the *erector spinae* is comprised of long muscles acting across several inter-vertebral joints, the *multifidus* is a group of shorter muscles acting across one to three inter-vertebral joints. Therefore, the net flexor moment across the upper vertebrae has to be balanced by fascicles of the *multifidus* group, leading to increased overall forces. This is reflected in the compressive forces in the spine, which shows increased loading for the upper vertebrae, with reduced loading on the lower ones. The middle column of Fig. 5.9 shows the shear loading in the spine. We see an overall reduction in the shear forces with the exosuit as compared to without. A peculiar observation from these graphs is the elevated shear forces in the regions of T1/T2 to T3/T4 and T10/T11 to L4/L5 joints. This is because of the exosuit forces F_{Ex}^S and F_{SPA}^B acting on the shoulder and back respectively.

We also observe that for the muscles of *erector spinae*, *latissimus dorsi* and *external oblique*, the simulated constant stiffness model resembles closely to the exosuit at 20 kPa. For the remaining muscles, the predicted forces between these two conditions is similar only for larger angles, and the constant stiffness model behaves similar to the no exosuit condition at smaller bending angles. The same pattern is seen also for the spinal loading, in which we see that for the larger angles of 60 and 90 degrees, the constant stiffness model shows similar loading pattern as the exosuit at 20 kPa. At the smaller angles, especially for 0 degrees, the constant stiffness model is exactly equal to the no exosuit conditions, as the tension forces are zero.

Lastly, we compared our results to those from eleven devices reported in literature. Fig. 5.10 shows the comparison of three metrics: *erector spinae* muscle activation, compressive loading at the L5/S1 joint, and moment at the L5/S1. From the various studies for each device, we selected the largest reported values of the metrics. We see that for all the three metrics, our device is comparable to existing devices, with around 60% reduction for ES activity and hip moment, and around 42% reduction for the compressive spinal force. The simulations predict similar or slightly higher assistance than previous studies, which is mainly due to the significantly higher forces (250 to 500 N) applied by the SPAs at 20 kPa. We also see

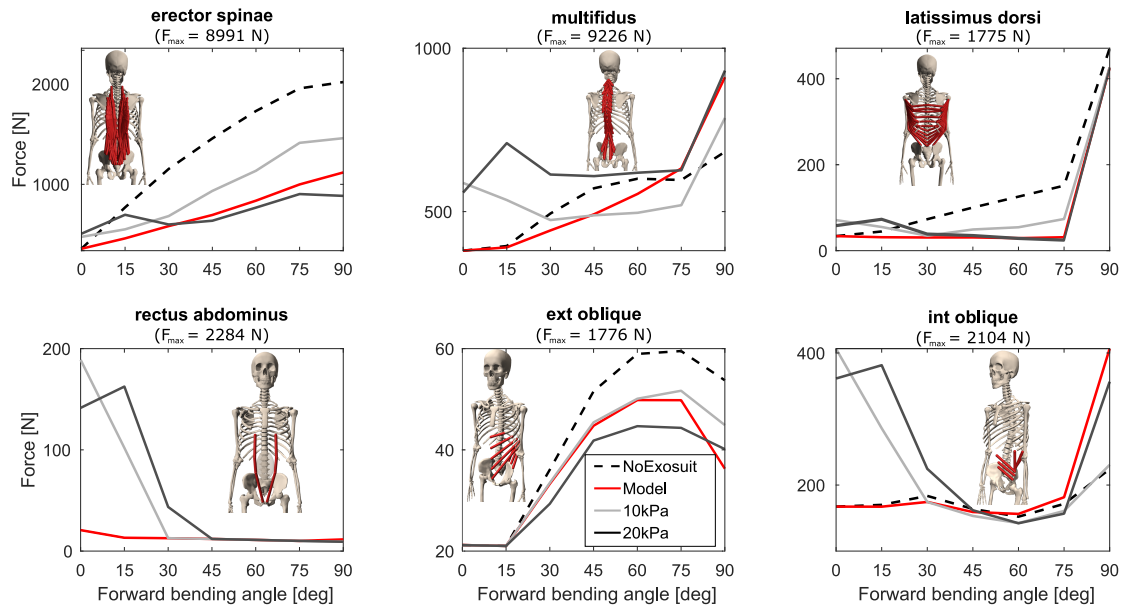


Figure 5.8: Loading across the muscles of the torso for the four conditions: no exosuit, exosuit at 10 kPa, exosuit at 20 kPa, simulated constant stiffness model. Overall, we see a reduction in muscle forces while using the exosuit. This is seen significantly for the *erector spinae* group, which is the primary extensor of the back. We also observe a slight negative effect on the *rectus abdominus*, *internal oblique* and the *multifidus* muscles, especially at lower angles. For the abdominal muscles, this is expected, as the exosuit applies a moment opposite to that applied by the muscles. For the multifidus, this occurs because of the increase in moment across the upper intervertebral joints (Fig. 5.9 right column), which has to be compensated by the *multifidus* muscle group.

that most studies only report the EMG activity of the *erector spinae*, with relatively fewer studies reporting the L5 moment or compressive forces. This is because the muscle activity is measured, whereas the moment and compressive loading requires additional modelling, simulations and analysis.

These results effectively demonstrate that, while there is a reduction in the average compressive, shear and moment loading across the spine, the exosuit does redistribute the load. This is primarily from the *erector spinae* to the *multifidus* muscle group, and from the lower to upper vertebrae. More studies and analysis with medical researchers will have to be conducted to analyse the overall impact of the device. However, we can still use the device to shift the moment across the vertebrae to temporally share the load across the vertebrae and could reduce the occurrences of work-related musculoskeletal disorders.

5.6 Discussion

In this Chapter, we presented the design, modelling, testing, and biomechanical evaluation of a soft exosuit. The proposed design consists of pouch-type SPAs that generate large, but well-distributed forces, and nylon webbing that helps to redirect these forces to the desired locations on the torso in order to generate an assistive moment at the spine. The location of

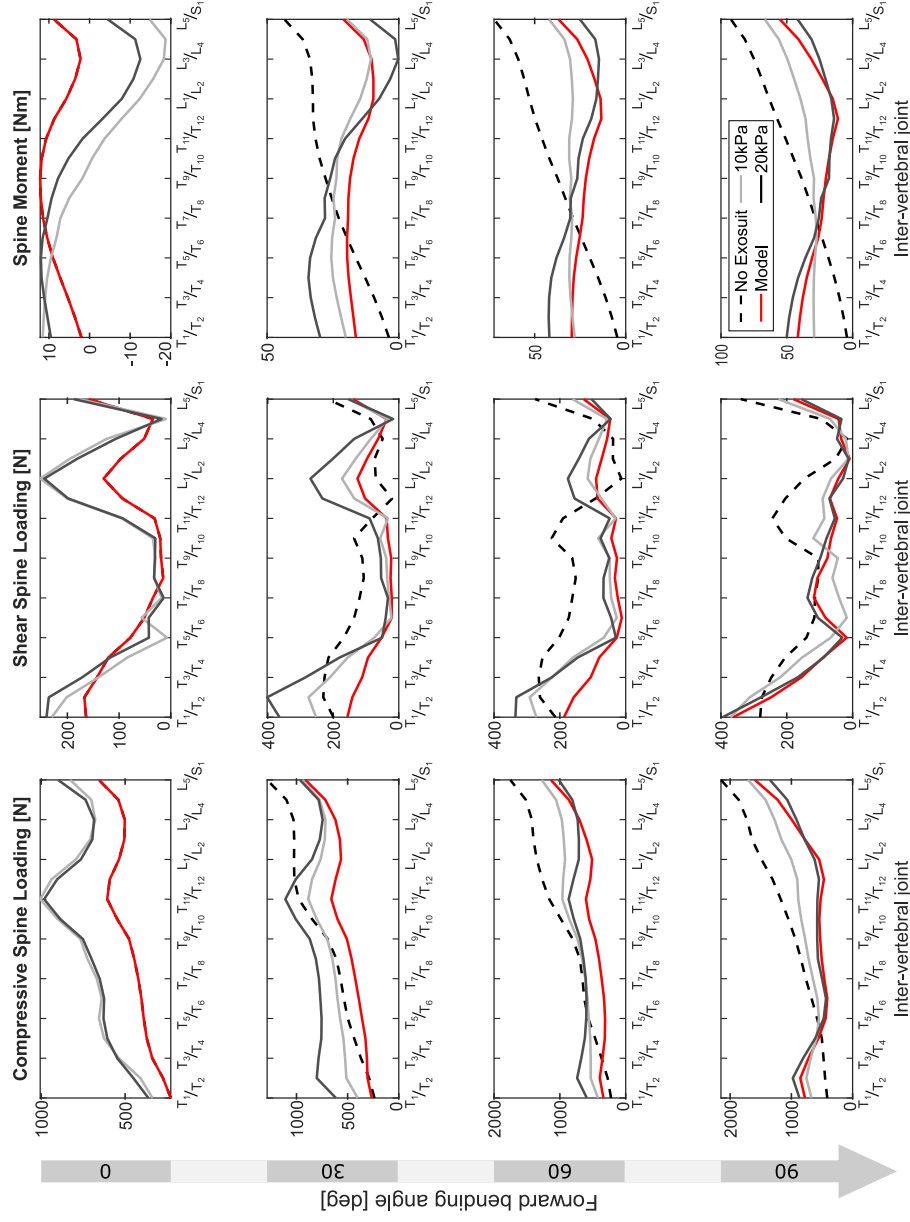


Figure 5.9: Loading across the intervertebral joints at four forward bending angles, 0, 30, 60, and 90 degrees, for the four conditions: no exosuit, exosuit at 10 kPa, exosuit at 20 kPa, simulated constant stiffness model. The left, middle and right columns correspond to compressive, shear, and moment loading. The arrow on the left depicts the increasing forward bending angle. We observe an overall decrease in the loading of the spine with the exosuit for all three loads, especially at the higher angles of 60 and 90 degrees. At the lower angles, however, some negative effects are seen, especially for compressive loading and spine moment. We also observe that there is a general trend of loading being redistributed from the lower to upper vertebrae, while using the exosuit. These effects need further analysis so as to assess how they would affect the user.

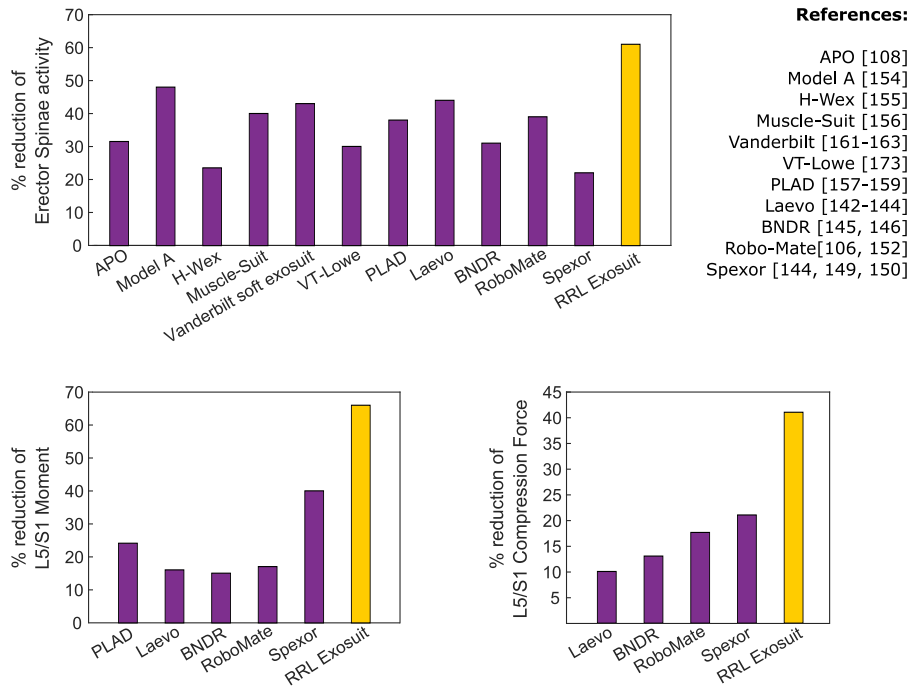


Figure 5.10: Comparison of the biomechanical effect of the proposed exosuit with state of the art devices using the metrics of % reduction in muscle activity, L5/S1 moment, and L5/S1 compression force. For all the considered devices, we chose the largest value reported in literature. The bar in yellow corresponds to the predicted values of the metrics for the proposed exosuit. Firstly we observe that measured muscle activity is the most commonly reported metric. Secondly, the predicted values of the exosuit are comparable or higher for the presented exosuit. This is primarily because of the high forces (up to 500 N) applied by the exosuit.

the SPAs and webbing can be reconfigured easily to assist different motions such as forward or lateral bending, twisting, and posture support. The modelling approach presented in this work considers the forces applied in all the sections of the webbing so as to accurately capture the complete effect of the exosuit. After testing with two subjects in forward bending assistance, we inputted the measured interaction forces into the human-exosuit model and calculated the loading on the intervertebral joints and six muscle groups. The results show that using the exosuit can have significantly positive benefits on these metrics especially at larger bending angles. At the same time, operating the exosuit at lower bending angles can lead to co-contraction of abdominal muscles which can lead to increased hip moment as well as compressive and shear forces in the spine. Lastly, we also observed that even for an overall positive effect on the lumbar spine and muscles, using the exosuit led to some load redistribution from the superficial to the deep muscles, and from the lumbar to thoracic vertebrae. These findings provide a new insight into the effect of soft torso exosuits, and supplement the existing studies which conduct user surveys and measure EMG activity of some of the muscle groups. The design methodology, model, and biomechanical analysis presented in this study can be readily implemented in future studies with existing and new exosuits towards the iteration, comparison, and optimization of soft wearable robots.

In future studies, the effect of the exosuit in dynamic forward bending as well as other motions such as lateral bending or twisting can be investigated. Additional user studies in the future with measurement of biomechanical quantities such as muscle activity and metabolic rate will help to corroborate the predictions of the biomechanics simulations. Another direction would be to address some of modelling simplifications, for instance, by using more degrees of freedom to represent spine and hip kinematics. Similarly, forces need to be measured in both compression and shear so as to accurately represent the interaction between the user and the exosuit. Lastly, future investigations could consolidate the different areas of characterization, dynamic modelling, PSS optimization, and self-sensing in the final version of the exosuit so as to develop a complete system, similar to what was demonstrated for the initial version.

6 Conclusions and future outlook

Soft robots possessing unique properties of compliance and conformability provide an innovative approach to wearable robots, circumventing challenges in traditional rigid designs such as kinematic incompatibility, design complexity and bulky form factors. However, there were still some fundamental knowledge gaps related to understanding the mechanical performance of these robots and how they impact the biomechanics of the user. This thesis aimed to address some of these challenges and create a broader and deeper understanding of soft systems that could lead to effective design of wearable robots. The main contributions of this thesis are:

- Systematic, repeatable and accurate characterization of soft actuator mechanical performance.
- Modelling dynamic behaviour of nonlinear pneumatic actuators.
- Design, optimization, and biomechanical evaluation of wearable soft robots.

The sections below summarise the main findings, future research directions, and the broad impact of this thesis.

6.1 Conclusions

In Chapter 1, we focussed on quantifying the mechanical performance of soft robots. Previous studies characterized soft robots either in blocked conditions or limited range of motion, and often in loading conditions that differed from those of the intended application. The approach presented in this thesis is based on recreating application-specific loading conditions around a soft robot in order to accurately capture its mechanical behaviour while interacting with the surroundings. We developed an experimental protocol and platform, and demonstrated our method by characterizing a bending soft actuator in three loading conditions. This led to three distinct force and displacement characteristics, thus highlighting the importance of loading conditions on soft robot mechanical performance. The protocol presented is readily

applicable to existing and future soft robots for accurate and consistent characterization of their mechanical performance, and helps to better understand the impact of loading conditions. This can be further exploited to optimize the design and control of soft robots. Additionally, we extended this method for characterizing a meso-scale haptic device. While most previous studies with such devices report only user surveys or characterization in a small range of motion, we quantified the force-displacement characteristics of our fingertip haptic device in three actuation modes and in its entire range of motion. These methods and results will enable researchers to quantify and assess the forces applied by meso-scale haptic devices and link it to the psychophysical sensations felt by the user. This represents a direct characterization of the physical human-robot interface, and can help us to better understand how haptic sensations affect the user.

In Chapter 2, we investigated the dynamic behaviour of soft pneumatic actuators. We first presented a comprehensive pressure dynamics model that considers the impact of the *source*, *valve*, *tubing*, and *fittings*. We then quantified the direct relationship from the PSS component parameters and SPA design properties to the SPA dynamic performance using simulations, corroborated with exhaustive experimental testing. These studies included a wide range of model parameter combinations spanning commonly used SPAs and PSS components, and create an improved understanding of how different parameters affect SPA dynamic response. Using these results, it is now possible to tailor the PSS to meet the desired SPA dynamic performance. Furthermore, as several wearable and non-wearable applications demand additional requirements such as duration of untethered operation, or size and mass, we developed multi-objective design optimization for PSSs in Chapter 3. This is the first instance of optimizing the PSS for simultaneously meeting requirements of performance, portability, and user-defined constraints such as mass and size. The presented model as well as PSS optimization would enable improved and optimized systems for other researchers working with soft actuators, or pneumatic systems in general.

By investigating the effect of loading on dynamic behaviour, in Chapter 4, we introduced a previously unknown property of SPAs: self-sensing. This concept models the SPA itself as a pneumatic sensor, and uses the measured dynamic pressure response to estimate the interaction force and displacement. Using characterization data from experimental testing, we trained data-driven neural networks to estimate the interaction force and displacement using data derived solely from pressure sensors. This is a new direction in pneumatic actuators and can be readily implemented in existing systems without any change in hardware. For actuators without any dedicated sensors, our method enables the estimation of displacement and force, which was not possible previously. Furthermore, for actuators with sensors, the addition of this sensorless method increases estimation accuracy due to the added sensing redundancy.

The last part of the thesis was dedicated towards investigating the effect of soft exosuits on the biomechanics of the user. As soft exosuits use the wearer's body as the structure to transmit forces, it is critical to understand how they affect the biomechanics of the user, especially

for sensitive locations such as the spine. While existing studies conduct user surveys or measure muscle activity of a few muscles, this information is insufficient for an in-depth evaluation. In Chapter 5, we presented the design of a soft exosuit for the torso, and developed a comprehensive human-exosuit model so as to analyse the effect of the device on the muscle and joint loading of the wearer. The presented soft exosuit is powered by pouch-type SPAs sandwiched between the user and strategically routed fabric webbing, and can be reconfigured to assist the wearer in different motions such as forward bending, lateral bending, twisting, and posture support. To evaluate its effect on the user, we modelled the forces generated in each section of the exosuit, and implemented them on a musculoskeletal model of the human torso. We tested the exosuit with two subjects and inputted the measured interaction forces in the human-exosuit model. Predictions from simulations indicate decreased overall loading on the torso muscles and intervertebral joints, but also accompanied by some load redistribution to the deeper muscles and upper vertebrae. This represents the first instance of quantifying the impact of soft exosuits on the entirety of the spine and the deep muscle groups of the torso. They also highlight the importance and need of comprehensive human-exosuit modelling and simulations in addition to solely measuring EMG of certain muscle groups, which is commonly carried out in previous studies. The design, modelling, testing, and biomechanical evaluation presented in this work will act as a foundation towards better understanding and improved designs of torso exosuits.

6.2 Current limitations of the thesis and future research directions

The principal objective of this thesis was to investigate and quantify the mechanical behaviour, dynamic performance, and biomechanical effect on the user, in order to create a system-wide understanding of soft and wearable robots. Divided into five chapters, this thesis addresses the research questions posed at the start and provides meaningful insights towards design, dynamic analysis, and evaluation of soft and wearable robots. At the same time, it is important to outline the scope of application and limitations of this research.

The novel characterization protocol aimed to recreate the environment around soft robots, but we only studied three types of anchoring conditions at the contact point: hinged, fixed, and overlapping fabric. It would be useful to explore other boundary conditions observed in practice such as impedance of the contact point or having a boundary surface instead of a contact point. Detailed investigation with different types of such boundary conditions would help to create a general understanding of how they affect mechanical behaviour of soft robots. Also, we only characterized the quasi-static mechanical output. Future studies can focus on implementing the proposed method during dynamic characterization. Lastly, for some type of loading conditions such as granular medium, compliant surface contact, or variable loading would be challenging to recreate using the presented method. In such a case, other approaches, including analytical or numerical methods will have to be adopted.

In the pressure dynamics model presented in this thesis, we assumed all processes to be

isothermal at standard conditions. A more accurate thermodynamics model would be useful for future studies, especially for systems with large pressure changes, for example, carbon dioxide cartridges or high pressure (20 MPa) gas cylinders. Furthermore, in modelling the dynamic response, we did not consider the effect of inertia or viscoelasticity. In future studies, these effects could be incorporated in the model and SPA frequency response can be analysed to study the interplay between inertial, viscoelastic and pressure dynamics. This model can be additionally combined with the force and displacement output of SPAs, in order to create a complete dynamics model for SPAs and pneumatic actuators in general. Such a complete model could help to achieve accurate model-based control of soft robots.

The presented method of sensorless estimation in SPAs represents a new dimension in sensing and feedback control. The main underlying assumption in this approach is the existence of a one-to-one relationship between the mechanical outputs (force and displacement) and pneumatic inputs (pressure, flow, volume, airmass). Therefore, sensorless estimation would work for only those actuators where this assumption is held. A theoretical investigation of this property would help to establish the feasibility and stability of sensorless estimation in a general case and outline the conditions where it would or would not work. It would be also useful to study how different aspects such as properties of the PSS and SPA, and loading conditions affect sensing accuracy. Lastly, future studies could be directed towards addressing integration drifts, which was one of the main source of error in the current study.

With respect to the exosuit, we only tested in static forward bending. Therefore, while the exosuit provides sufficient support, we could not evaluate if it could respond dynamically to the movements of the wearer. Future efforts would be directed towards testing the device in dynamic lifting. Also, clinical studies with more subjects and measurement of biomechanical parameters such as muscle activity and metabolic rate can be carried out to support and validate the findings from simulations. At the component level, the pouch-type SPAs had low actuation speed due to the low operating pressure and large internal volume. Different SPA designs can be explored that can provide a similar amount of support, while being operational at higher speeds. Additionally, more sensors can be incorporated into the exosuit for measuring SPA forces, exosuit tension, or subject kinematics. In addition to forward bending, the design strategy presented in this thesis can be adapted for designing torso exosuits for assisting diverse movements such as lateral bending, twisting, or compounded motions. Lastly, the biomechanical modelling and simulations can be applied to optimize design and control parameters of the exosuit such as actuator locations and forces, routing of the fabric webbing, and different control strategies. Lastly, our results indicate that there are some potentially detrimental effects of using the exosuit, namely, increased loading on upper vertebrae and deeper muscles. These effects must be carefully studied with experts in biomechanics and physiology so as to prevent any negative side effects of such wearable assistive devices.

While this thesis investigated different aspects of soft and wearable robots, it could not include a complete system incorporating them all. Although the initial design of the exosuit did have

on-board actuation, power, sensing, and control, the final exosuit design only included actuation and sensing. In upcoming studies, these different technologies could be consolidated to develop a complete exosuit system.

6.3 Broad impact

Looking back at the beginning, this thesis addressed fundamental challenges existing in soft and wearable robots, which included quantifying their mechanical output, dynamic performance, and biomechanical effect on the user. From Fig. 3 in the Introduction, we can see the broad impact of this work creates core understanding in *Performance characterization* and *Core supporting systems*, which constitute the fundamental principles that govern how soft technologies work. The knowledge developed is applicable not only to wearable robots, but also other applications including mobile robots, manipulators and haptic devices. For instance, the method for accurate and repeatable mechanical characterization is applicable to soft robots in general, whereas the dynamic modelling, PSS optimization and self-sensing are applicable to all pneumatic robots. Towards the specific application of wearable robots, we presented a human-exosuit model, conducted simulations, and analysed how the exosuit affects biomechanical quantities of the user. These can be readily adopted by other researchers in the field for both soft and rigid torso assistance devices, so as to supplement their findings from user surveys and measurement of biomechanical quantities. While there is still plenty more that can be accomplished, the findings of this thesis contribute to basic building blocks that will be useful for the future evolution of robotic technologies.

Appendices

A1 Kinematics of the Haptigami

We model Haptigami as two squares with equal dimensions and of side length s , as presented in Fig. A1b. The bottom face is grounded, while the top face is free, with O and C representing the coordinates of their square centers. The sphere, placed between the two faces, is fixed to the bottom face, with vector $\vec{S}_b = (-Fpos, 0, 0)$ representing the point of contact. $Fpos$ is the distance between the square's center and sphere contact point on the bottom square. We assume the top face to freely slide and roll over the sphere, with the point of contact given by vector $\vec{S}_t = \vec{S}_b + r \cdot \vec{z} + r \cdot \vec{n} = (x_0, y_0, z_0)$:

$$x_0 = r \cdot n_x - Fpos; \quad y_0 = r \cdot n_y; \quad z_0 = r \cdot n_z + r \quad (A1)$$

where n_x , n_y and n_z are x, y and z components, respectively, of the unit vector \vec{n} , normal to the upper platform. Using spherical coordinates, \vec{n} is defined as $\vec{n} = (\sin(\psi) \cdot \cos(\delta), \sin(\psi) \cdot \sin(\delta), \cos(\psi))$.

Using the above equations, the plane corresponding to the top face is given by

$$n_x \cdot (x - x_0) + n_y \cdot (y - y_0) + n_z \cdot (z - z_0) = 0 \quad (A2)$$

We define Haptigami's motion as the relative motion between the top and bottom faces denoted by the Cardan angles roll and pitch, calculated as follows:

$$roll = \frac{\arccos(\psi)}{\sqrt{\sin^2(\psi) \cdot \cos^2(\delta) + \cos^2(\psi)}} \quad (A3)$$

$$pitch = \frac{\arccos(\psi)}{\sqrt{\sin^2(\delta) \cdot \sin^2(\psi) + \cos^2(\psi)}} \quad (A4)$$

Controlling the tendon lengths, powered by the piezomotors allows achieving this motion. The vectors \vec{Tfront} and \vec{Tside} , which are connected at the mid-points, $Mfront$ and $Mside$, of the top face edges represent these tendons.

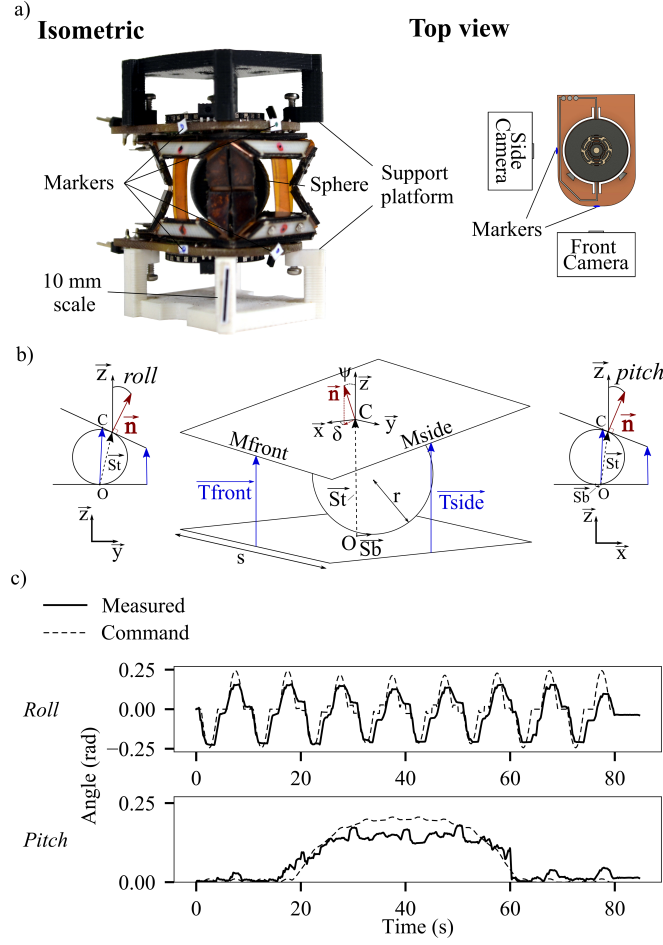


Figure A1: Haptigami's kinematic model and closed-loop control experiment and results: a) Experimental setup used to verify kinematic model; We fixed Haptigami on a support platform with a 3D-printed sphere inside and used a front and side cameras to record the marker positions, deducing the tendon lengths and platform orientation. b) We model our system as two plates with a sphere inside, representing the user's finger contact point and determine the motion of the two plates by the sphere and tendon lengths. c) Comparison between model and the measured values of roll and pitch angles.

$$\overrightarrow{T_{front}} = \begin{bmatrix} 0 \\ (s/2) \cdot (1 - \cos(roll)) \\ T_{side_z} + (s/2) \cdot \sin(roll) \end{bmatrix} \quad (A5)$$

$$\overrightarrow{T_{side}} = \begin{bmatrix} (s/2) \cdot (1 - \cos(pitch)) \\ 0 \\ T_{front_z} + (s/2) \cdot \sin(pitch) \end{bmatrix} \quad (A6)$$

As points M_{front} and M_{side} lie on the top face, they satisfy (A2).

$$\begin{aligned} n_x \cdot M_{side_x} + n_y \cdot M_{side_y} + n_z \cdot M_{side_z} &= d \\ n_x \cdot M_{front_x} + n_y \cdot M_{front_y} + n_z \cdot M_{front_z} &= d \end{aligned} \quad (A7)$$

where $d = n_x x_0 + n_y y_0 + n_z z_0$. The set of equations (A1) to (A7) gives the kinematics of Haptigami that relate the inputs, $\|\overrightarrow{Tside}\|$, $\|\overrightarrow{Tfront}\|$, to the outputs, $pitch$, $roll$ or ψ and δ . The forward kinematics are difficult to derive due to the complexity of the equations required to isolate ψ and δ . To address this, we use the numeric solver NLSolve.jl [169] which gives the correct angle in an average time of 1ms after the first compilation. Solving (A7) gives the reverse kinematics:

$$\begin{aligned} \|\overrightarrow{Tfront}\| = & (((\cos(pitch)s - s - 2Fpos) \cos(\delta) \\ & - s \sin(\delta)) \sin(\varphi) \\ & + (-\sin(pitch)s + \\ & 2r) \cos(\varphi) + 2r) / (2 \cos(\varphi)) \end{aligned} \quad (A8)$$

$$\begin{aligned} \|\overrightarrow{Tside}\| = & (((-s - 2Fpos) \cos(\delta) + s \sin(\delta) \\ & (\cos(roll) - 1)) \sin(\varphi) \\ & + (-\sin(roll)s + 2r) \cos(\varphi) \\ & + 2r) / (2 \cos(\varphi)) \end{aligned} \quad (A9)$$

Additionally, we determine the top plate's centre coordinates as follows:

$$\begin{aligned} \overrightarrow{OC} = & \frac{\overrightarrow{OMside} + \overrightarrow{OMfront}}{2} \\ & + \frac{\overrightarrow{OMside} - \overrightarrow{OMfront}}{2} \times \vec{n} \end{aligned} \quad (A10)$$

Finally, to control the interface, we converted the tendon lengths into rotation angles of the driving piezomotors using the conventional offset slider-crank kinematic equations that relate the motor rotation angle θ , to the tendon length t , as explained in [170]. The slider position x of a slider-crank mechanism, which is a measure of the tendon length, is given by:

$$x = a \cdot \cos(\theta) + b \cdot \cos(\mu(\theta)) \quad (A11)$$

with

$$\mu(\theta) = \arcsin\left(\frac{a \cdot \sin(\theta) - c}{b}\right) \quad (A12)$$

where a , b and c , are the crank, rod and offset size, respectively and μ is the angle between the connecting rod and the slider.

We solve the above by using a solver in [171] to get the equation for $\theta(x)$, and we use this equation directly in the control.

A2 Modelling pressure dynamics of PSS

We classify PSSs into two types: *constant pressure PSSs* and *constant flow PSSs*; as described in Fig. 2.2. For *constant pressure PSSs*, we have $\dot{P}_{src} = 0$. For *constant flow PSSs*, P_{src} does not remain constant due to inflow and outflow from the reservoir. Applying ideal gas equations and expressing mass flow rate as standard volumetric flow at P_0 , T_0 , the *source* pressure dynamics are given by:

$$\dot{P}_{src} V_{res} = \frac{RT_0}{M_{air}} \rho_{air} (Q_{com} - pos(Q_{spa})) \quad (A13)$$

where V_{res} is the reservoir volume including dead volume of the tubing and fittings between the compressor and reservoir, R is the ideal gas constant, M_{air} is molar mass of air, ρ_{air} is air density at P_0 , T_0 , Q_{com} is the mass flow from the compressor expressed in standard L/s, and $pos(Q_{spa})$ is the positive mass flow from the actuator, i.e., flow from reservoir to soft actuator, in standard L/s.

Negative actuator flow does not affect P_{src} , as the air is exhausted to the ambient. For one mole of air at standard conditions, $M_{air}/\rho_{air} = V_0 \times 10^{-6}$, and $P_0 V_0 \times 10^{-6} = RT_0$, where V_0 is the volume of one mole of air at P_0 , T_0 . The 10^{-6} term is seen because V_0 is expressed in L instead of m^3 . Using these relations in Eq. A13 we get,

$$\dot{P}_{src} = \frac{P_0}{V_{res}} (Q_{com} - pos(Q_{spa})) \quad (A14)$$

The flow Q_{spa} is through the *valve* and *pneumatic line*, i.e. tubing and fittings. To model it, we use ISO 6358 [84]. This is an empirical approximation of the analytical solution of flow through an orifice, and is suitable for modelling gas flow through a variety of pneumatic components as well as through series and parallel combinations [172; 85; 90]. It describes the flow through a component using two parameters, sonic conductance, C , and critical ratio, b , ($0 < b < 1$), as shown below:

$$Q = C\Psi P_{High} \quad (A15)$$

$$\Psi = \begin{cases} \sqrt{1 - \left(\frac{\frac{P_{Low}}{P_{High}} - b}{1-b}\right)^2}, & \frac{P_{Low}}{P_{High}} \geq b \\ 1, & \frac{P_{Low}}{P_{High}} < b \end{cases} \quad (A16)$$

where P_{High} and P_{Low} are the absolute upstream and downstream pressures respectively; C and b are the sonic conductance and critical ratio respectively of the component, and Ψ is the non-linear flow function.

The nature of flow depends on the ratio of downstream to upstream pressure. If the pressure ratio is below the critical value, b , the flow is choked, i.e. air flows at sonic speed, and the flow

is only dependent on P_{High} and C . When pressure ratio is above b , the flow is a non-linear function of b , C and P_{High} . When the pressure ratio becomes 1, there is no flow due to absence of a pressure differential. While Eq. A15 and A16 define flow for a single component, the combined effect of the various components in the flow path can be modelled with the same set of equations by using the equivalent conductance and critical ratio [85]. Below, we discuss empirical expressions for the elementary combinations of series and parallel, which can be used to model complex PSSs containing several components [98; 85].

• **Series combinations**

For components connected in series, the equivalent parameters C_{eq} and b_{eq} are calculated in sequence starting from the first component in the direction of flow. First an auxiliary variable, ϵ , is calculated as given by [98]:

$$\epsilon = \frac{C_1}{b_1 C_2} \quad (A17)$$

where subscripts 1 and 2 correspond to the first and second component respectively in the flow path (in the direction of flow).

The value of ϵ predicts which component will be choked (sonic flow). If $\epsilon \leq 1$, flow in the first component becomes choked. If $\epsilon = 1$, both components have choked flow. If $\epsilon \geq 1$, the second component becomes choked.

Next, the equivalent sonic conductance $C_{1,2}$ of the series connection is given by [98] and [85]:

$$C_{1,2} = \begin{cases} C_1 & , \epsilon \leq 1 \\ \epsilon C_2 \cdot \frac{\epsilon b_1 + (1-b_1) \sqrt{\epsilon^2 + \left(\frac{1-b_1}{b_1}\right)^2}}{\epsilon^2 + \left(\frac{1-b_1}{b_1}\right)^2} & , \epsilon \geq 1 \end{cases} \quad (A18)$$

And the equivalent critical pressure ratio is given by

$$b_{1,2} = 1 - C_{1,2}^2 \left(\frac{1-b_1}{C_1^2} + \frac{1-b_2}{C_2^2} \right) \quad (A19)$$

If there is a third component, the above steps must be repeated by taking $C_{1,2}$, $b_{1,2}$ and C_3 , b_3 . The equivalent parameters, C_{eq} and b_{eq} of the entire flow path can be calculated by sequentially following these steps while considering all components in series.

• **Parallel combinations**

If the components are connected in parallel, the equivalent sonic conductance is given by the empirical relation described by [98; 85]:

$$C_{eq} = \sum_{i=1}^n C_i \quad (A20)$$

And the critical ratio is given by,

$$\frac{C_{eq}}{\sqrt{1-b_{eq}}} = \sum_{i=1} \frac{C_i}{\sqrt{1-b_i}} \quad (A21)$$

By appropriately using the relations A17 to A21, we can calculate C_{eq} and b_{eq} for a set of tubing, fittings and valves. Moreover we can design and model more complex PSSs connecting several components. C and b for valves, tubing and fittings can be generally found from manufacturers' technical manuals, or can be characterized using the guidelines given by ISO 6358 [84]. For the tubing, they can also be calculated using the following empirical relationship as described by Eckersten et. al [85; 98]:

$$C_{tubing} = \frac{0.029D^2}{\sqrt{\frac{L}{D^{1.25}} + 510}}; \quad b = \frac{474C}{D^2} \quad (A22)$$

where L and D are the tubing length and inner diameter respectively in m.

A3 Modelling soft actuator pressure dynamics

We model the soft actuator as a chamber with variable internal volume, V_{spa} .

$$\dot{P}_{spa} V_{spa} + P_{spa} \dot{V}_{spa} = P_0 Q_{spa} \quad (A23)$$

where P_{spa} is the instantaneous soft actuator pressure; V_{spa} is the soft actuator internal volume including dead volume of tubing and fittings between valve and soft actuator; and Q_{spa} is the mass flow to the soft actuator expressed in standard L/s.

V_{spa} is governed by P_{spa} , soft actuator design, external forces and inertial forces. Neglecting effect of the external and inertial forces, we express the freely expanding/contracting soft actuator volume quasi-statically as a function of its pressure. A general case with a non-linear relation between pressure and volume can be modelled by defining $V_{spa} = f(P_{spa})$. In this case, the dynamics are given by:

$$V_{spa} = f(P_{spa}); \quad \dot{V} = \frac{df}{dP_{spa}} \dot{P}_{spa} \quad (A24)$$

$$\dot{P}_{spa} f(P_{spa}) + P_{spa} \frac{df}{dP_{spa}} \dot{P} = P_0 Q_{spa} \quad (A25)$$

Rearranging the above, we get the soft actuator pressure dynamics, while implicitly considering internal volume dynamics as:

$$\dot{P}_{spa} = \frac{P_0 Q_{spa}}{f(P_{spa}) + P_{spa} \frac{df}{dP_{spa}}} \quad (\text{A26})$$

Based on several recent studies [10; 53; 45; 54; 28], we consider a linear pressure-volume relation in this study as:

$$V_{spa} = f(P_{spa}) = V_{spa}^0 (1 + K_{exp}(P_{spa} - P_0)) \quad (\text{A27})$$

where we define the expansion ratio, K_{exp} , as a constant relating P_{spa} to V_{spa} ; and V_{spa}^0 is the actuator volume at $P_{spa} = P_0$.

Thus, we have $\frac{df}{dP_{spa}} = V_{spa}^0 K_{exp}$, to give:

$$\dot{P}_{spa} = \frac{P_0 Q_{spa}}{V_{spa}^0 (1 + K_{exp}(P_{spa} - P_0)) + V_{spa}^0 K_{exp} P_{spa}} = \frac{P_0 Q_{spa}}{V_{spa}^0 (1 + K_{exp}(2P_{spa} - P_0))} \quad (\text{A28})$$

A4 Defining valve duty cycle

To achieve cyclic actuation, an alternating and repeating control sequence has to be applied to the valve. For the context of this paper, we define two valve states, ON and OFF, as described in Fig. A2. The total ON time includes time of inflation (red), in addition to the time for which the soft actuator stays at P_{op} (blue). Similarly, OFF time includes the time for deflation (yellow) and the time for which the soft actuator stays at P_0 (green). Based on these ON and OFF valve states, we define valve duty cycle D_V as the ratio of the valve ON time to the total cycle time (ON + OFF times). Thus, a cyclic actuation will constitute alternating ON and OFF states of the valve, in which the variables are valve operation frequency and duty cycle. f_{max} is achieved when the valve switches state as soon as it reaches one of the extremes P_{op} or P_0 , i.e., only the red and yellow sections.

While we make an assumption here that P_{spa} oscillates between P_{op} and P_0 , in practice, care must be taken to ensure that P_{spa} does not increase beyond P_{op} to prevent overpressure, which may damage the soft actuator.

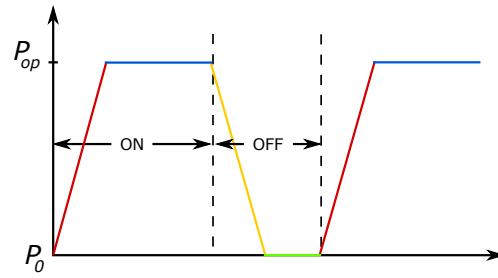


Figure A2: The different valve states during cyclic actuation. The ON time includes inflation (red), and $P_{spa} = P_{op}$ (blue). The OFF time includes deflation (yellow) and $P_{spa} = P_0$ (green). Duty cycle is defined as the ratio of ON time to the total cycle time (ON + OFF Time).

A5 Expressions for air and energy consumed

Let V_0 and V_{op} be the initial and final internal volumes respectively of the SPA. After adding the volumes of tubing $V_t = \pi D^2 L/4$ and fittings, V_f , the total internal volume increases from $V_0 + V_t + V_f$ at P_0 to $V_{op} + V_t + V_f$ at the SPA operating pressure, P_{op} . Taking the difference, the amount of air required to inflate the SPA from P_0 to P_{op} is given by:

$$A = \frac{P_{op}(V_{op} + V_t + V_f) - P_0(V_0 + V_t + V_f)}{P_0} \quad (A29)$$

where all pressure values are expressed in absolute pressure, and A is the consumed air mass expressed in terms of volume at standard conditions. This air, supplied to the SPA from the *source*, is stored at P_{src} .

The energy required by the *source* to pressurize this amount of air from P_0 to P_{src} can be calculated using the work done in isothermal compression as follows:

$$E = A \times P_0 \log_e \frac{P_{src}}{P_0} \quad (A30)$$

We see that the energy required is dependent on the storage pressure P_{src} , in addition to the air consumed. Thus, for the same air consumed, A , a larger P_{src} will lead to higher energy consumption. However, this consideration is only important for PSSs where the pressurized air is actively generated, such as compressors [82]. For PSSs powered by high pressure (20MPa to 30 MPa) gas cylinders or liquid CO_2 cartridges, E should not be considered [82].

A6 Validating PSS simulation results via testing with pneunet

Table A1: Comparison of measured rise time, MAF and duty cycle of pneunet with simulations

Source pressure [MPaG]	Rise time [s]		f_{max} [Hz] and Duty cycle [%]	
	Model	Measured	Model	Measured
0.10	1.29	1.22	0.45 (57.1%)	0.45 (58.2%)
0.15	0.70	0.71	0.62 (43.5%)	0.61 (43.0%)
0.20	0.53	0.53	0.69 (36.5%)	0.69 (36.1%)
0.25	0.44	0.43	0.74 (31.7%)	0.74 (31.6%)
0.30	0.37	0.36	0.78 (28.1%)	0.78 (28.0%)
0.35	0.33	0.31	0.80 (25.0%)	0.82 (25.3%)
0.40	0.29	0.27	0.83 (22.6%)	0.84 (23.1%)

Table A2: RMS and peak errors between experimental and predicted pressure response of the pneunet during inflation and deflation

Inflation response		
Source pressure [MPaG]	RMS error [%]	Peak error [%]
0.10	0.80	1.35
0.15	0.63	1.06
0.20	0.77	1.51
0.25	1.63	2.30
0.30	2.36	2.97
0.35	4.14	5.11
0.40	5.21	6.32
Deflation response		
	RMS error [%]	Peak error [%]
-	0.51	1.06

A7 Selected components for optimal PSS design

Table A3: Details of optimally selected components

Component	Description	mass (kg)
Compressor	Double piston compressor, <i>Thomas GD</i> Output flow is linear with back pressure, i.e. P_{src} $\bar{Q} = 6.02 - 7.93(P_{src} - P_0)$ at $P_{src} = 0.22\text{MPaG}$, $\bar{Q} = 4.28$	0.7
Battery	8000 mAh, <i>Turnigy</i>	0.68
Reservoir	Two <i>SodaStream</i> bottles, 1 L each	0.06
Valve and manifold	Proportional flow valve, <i>Parker LowPro</i> . Controllable sonic conductance with peak value of $C = 2.2\text{L/s/MPa}$	0.074 each
Tubing	Standard tubing, <i>SMC</i>	0.023
Fittings	Standard fittings, <i>SMC</i>	0.051
	Overall mass	1.95

A8 Calculating ground-truth values for displacement in Three-point bending

For three point bending, we enforce the anchoring condition by securing the central section of the SPA-pack in a cantilever constraint on module 2 of the robotic platform, and enveloping an overlapping fabric as shown in Fig. 4.4. During testing, we measure the force F_y recorded by the load-cell of module 2 as shown in Fig. 4.4A. The displacement is defined by the deflection of the SPA mid-point with respect to its two ends, which we enforced by controlling the linear motor of module 2. As the SPA is constrained between the linear motor and the fabric straps, the SPA displacement is equal to that of the linear motor only when the strap is taught. When the strap is loose, the SPA is unconstrained, i.e. in free expansion, and hence, the displacement of the linear motor is not equal to that of the SPA. Rather than using external sensors for calculating displacement, we calculated the SPA displacement using the existing setup.

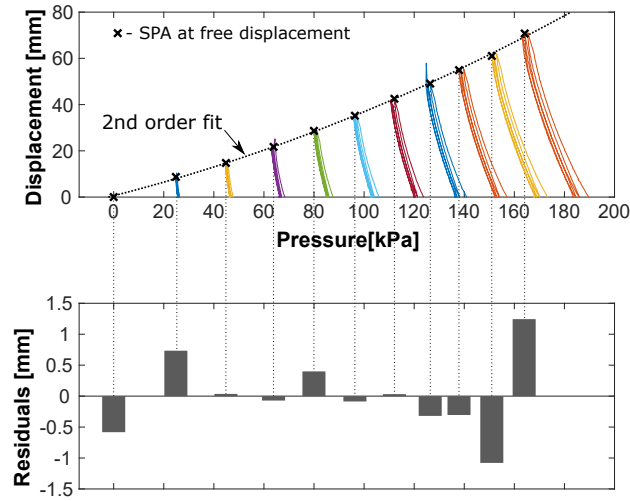


Figure A3: Defining displacement of the SPA-pack for three-point bending. We first separated the regions for constrained and free expansion, and plotted the pressure vs. displacement of the SPA-pack in the constrained expansion region. The points of largest displacement then correspond to the initiation of free expansion. We noted these points for the *hold* loading sequence, and fitted a second order polynomial to define the displacement as a function of SPA pressure. Good agreement is seen between the model and measured values as observed from the residuals.

First, we identified whether the SPA is constrained or unconstrained, using a small threshold on the measured force, $F_{min} = 1N$. For the constrained region ($F > F_{min}$), we considered displacement equal to that of the linear motor. For the unconstrained condition ($F < F_{min}$), as the displacement is only governed by the SPA air pressure, we modelled the free displacement as a function of its pressure. To find this mapping, we first plotted the measured pressure vs. *module 2* displacement in the constrained region ($F > F_{min}$), for the *hold* loading sequence. Then, we marked the points with largest displacement as shown in Fig. A3. These points correspond to the instances when the strap tension just becomes zero, thereby corresponding to the boundary between constrained and unconstrained SPA displacement. Using these

A8. Calculating ground-truth values for displacement in Three-point bending

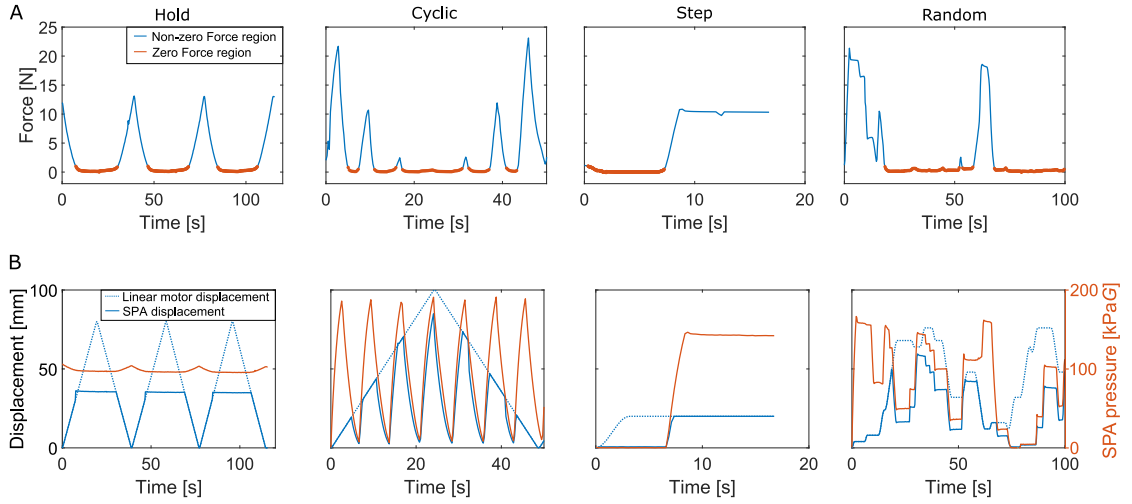


Figure A4: Calculating displacement for three-point bending. A. Using a small force threshold ($F_{min} = 1N$), we identify regions of either constrained or unconstrained expansion of the SPA-pack. The red curves have close to zero forces, thus corresponding to free displacement, while the blue curves have non-zero forces corresponding to constrained displacement. B. Comparison of calculated SPA displacement, module 2 linear motor displacement and SPA pressure. The continuous blue curves are the SPA displacement whereas the dotted curves are the displacement of the linear motor. The two curves coincide when the force is non-zero, thus showing constrained expansion of the SPA-pack. When they diverge, it means that the SPA is in free expansion and is therefore only a function of the pressure.

points, we fitted a second order polynomial, as shown by the dotted curve in Fig. A3. Using this method, we identified regions of constrained and unconstrained displacement in the entire dataset, and calculated the displacement for the SPA-pack. For the different loading sequences (*hold*, *step*, *cyclic*, *random*), Fig. A4A shows the regions of constrained or free expansion using the threshold, and Fig. A4B shows the displacement of the module 2 linear motor, the SPA-pack and the SPA pressure.

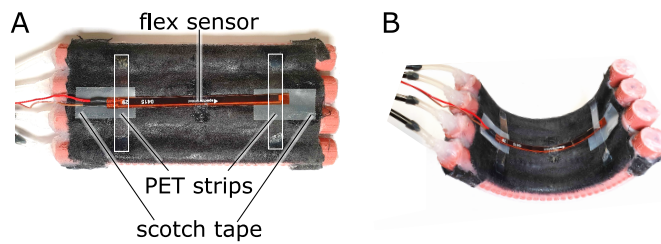


Figure A5: The SPA-pack sensorized with a standard flex sensor. We affixed a standard flex sensor (SpectraSymbol, 113mm x 6.4mm x 0.5mm) on the non-extending side of the SPA-pack. We affixed it at the centre only using silicone glue, Dow Corning 734. Additionally, we secured two PET strips on the SPA, which prevent the ends of the flex sensor from bending outwards from the SPA. Lastly, we stuck a low-friction tape between the flex sensor and the SPA-pack, which allowed the ends of the flex sensor to glide freely over the SPA-pack during bending. A. The SPA-pack in deflated state, B. The SPA-pack in inflated state.

A9 Characterization of pouch-type SPAs and contact pressure sensor

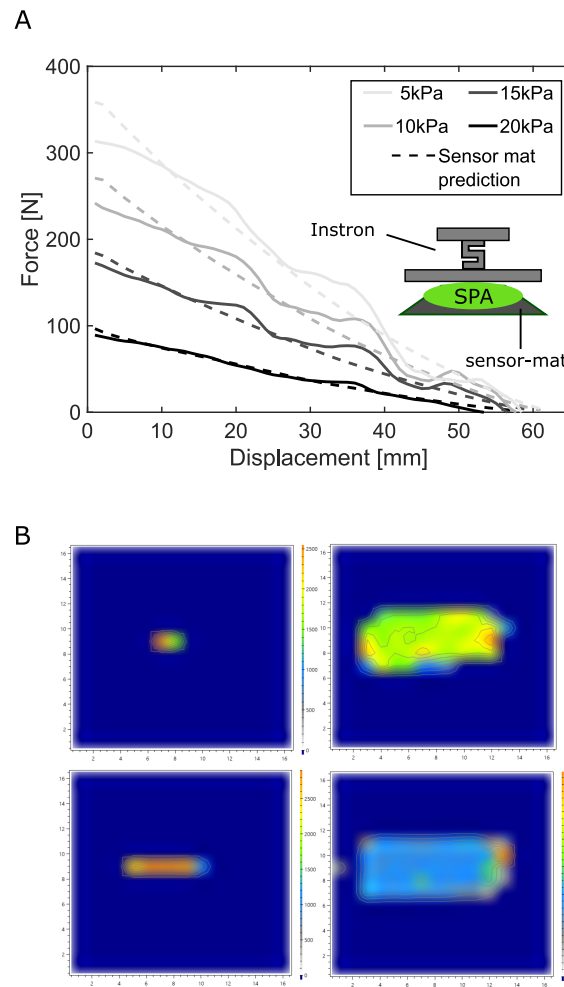


Figure A6: Characterization of the pressure sensing array and pouch-type SPA. The mats contain an array of force sensors arranged in a grid of either 8x8 or 16x16. We calibrated this mat and the force output of the pouch-type SPA by testing it in a standard Instron testing machine. We loaded the SPA and mat in the Instron and measured the ground truth values of force and displacement at four different air pressures. At the same time, we used a proprietary data acquisition software from SensingTex to recorded the readings from the pressure sensing mats containing 64 or 256 data-points per reading. We then fitted a linear regression model between the sensor reading and the ground truth values of force. (A) Experimental setup and the force vs. displacement data of the SPA. The continuous curves represent ground-truth values, and the dashed curves represent sensor predictions from the regression model. (B) Screenshots of the data acquisition software for the pressure sensing array, captured at different instances.

Bibliography

- [1] Mayumi Matsuda, Nobuaki Iwasaki, Yuki Mataka, Hirotaka Mutsuzaki, Kenichi Yoshikawa, Kazushi Takahashi, Keiko Enomoto, Kumiko Sano, Aoi Kubota, Tomohiro Nakayama, et al. Robot-assisted training using hybrid assistive limb® for cerebral palsy. *Brain and Development*, 40(8):642–648, 2018.
- [2] Jemina Fasola, Romain Baud, Tristan Vouga, Auke Ijspeert, and Mohamed Bouri. Bioinspired postural controllers for a locked-ankle exoskeleton targeting complete sci users. *Frontiers in Robotics and AI*, 7:156, 2020.
- [3] Amir Ebrahimi, Dorothea Gröninger, Rapahel Singer, and Urs Schneider. Control parameter optimization of the actively powered upper body exoskeleton using subjective feedbacks. In *Control, Automation and Robotics (ICCAR), 2017 3rd International Conference on*, pages 432–437. IEEE, 2017.
- [4] BT Quinlivan, S Lee, P Malcolm, DM Rossi, M Grimmer, C Siviyy, N Karavas, D Wagner, A Asbeck, I Galiana, et al. Assistance magnitude versus metabolic cost reductions for a tethered multiarticular soft exosuit. *Science robotics*, 2(2):eaah4416, 2017.
- [5] Michele Xiloyannis, Domenico Chiaradia, Antonio Frisoli, and Lorenzo Masia. Physiological and kinematic effects of a soft exosuit on arm movements. *Journal of neuroengineering and rehabilitation*, 16(1):1–15, 2019.
- [6] Tomoki Abe, Shoichiro Koizumi, Hiroyuki Nabae, Gen Endo, Koichi Suzumori, Nao Sato, Michiko Adachi, and Fumi Takamizawa. Fabrication of “18 weave” muscles and their application to soft power support suit for upper limbs using thin mckibben muscle. *IEEE Robotics and Automation Letters*, 4(3):2532–2538, 2019.
- [7] Panagiotis Polygerinos, Zheng Wang, Kevin C Galloway, Robert J Wood, and Conor J Walsh. Soft robotic glove for combined assistance and at-home rehabilitation. *Robotics and Autonomous Systems*, 73:135–143, 2015.
- [8] José L Pons. *Wearable robots: biomechatronic exoskeletons*. John Wiley & Sons, 2008.
- [9] Yasmin Ansari, Mariangela Manti, Egidio Falotico, Matteo Cianchetti, and Cecilia Laschi. Multiobjective optimization for stiffness and position control in a soft robot arm module. *IEEE Robotics and Automation Letters*, 3(1):108–115, 2017.

- [10] Bobak Mosadegh, Panagiotis Polygerinos, Christoph Keplinger, Sophia Wennstedt, Robert F Shepherd, Unmukt Gupta, Jongmin Shim, Katia Bertoldi, Conor J Walsh, and George M Whitesides. Pneumatic networks for soft robotics that actuate rapidly. *Advanced Functional Materials*, 24(15):2163–2170, 2014.
- [11] Matthias Hofer and Raffaello D’Andrea. Design, modeling and control of a soft robotic arm. In *2018 IEEE/RSJ International Conference on Intelligent Robots and Systems (IROS)*, pages 1456–1463. IEEE, 2018.
- [12] Carly M Thalman, Quoc P Lam, Pham H Nguyen, Saivimal Sridar, and Panagiotis Polygerinos. A novel soft elbow exosuit to supplement bicep lifting capacity. In *2018 IEEE/RSJ International Conference on Intelligent Robots and Systems (IROS)*, pages 6965–6971. IEEE, 2018.
- [13] Simon Hauser, Matthew Robertson, Auke Ijspeert, and Jamie Paik. Jammjoint: A variable stiffness device based on granular jamming for wearable joint support. *IEEE Robotics and Automation Letters*, 2(2):849–855, 2017.
- [14] Ciarán T O’Neill, Nathan S Phipps, Leonardo Cappello, Sabrina Paganoni, and Conor J Walsh. A soft wearable robot for the shoulder: Design, characterization, and preliminary testing. In *2017 International Conference on Rehabilitation Robotics (ICORR)*, pages 1672–1678. IEEE, 2017.
- [15] Saivimal Sridar, Zhi Qiao, Niveditha Muthukrishnan, Wenlong Zhang, and Panagiotis Polygerinos. A soft-inflatable exosuit for knee rehabilitation: Assisting swing phase during walking. *Frontiers in Robotics and AI*, 5:44, 2018.
- [16] Yong-Lae Park, Bor-rong Chen, Néstor O Pérez-Arancibia, Diana Young, Leia Stirling, Robert J Wood, Eugene C Goldfield, and Radhika Nagpal. Design and control of a bio-inspired soft wearable robotic device for ankle–foot rehabilitation. *Bioinspiration & biomimetics*, 9(1):016007, 2014.
- [17] Jan Fras and Kaspar Althoefer. Soft biomimetic prosthetic hand: Design, manufacturing and preliminary examination. In *2018 IEEE/RSJ International Conference on Intelligent Robots and Systems (IROS)*, pages 1–6. IEEE, 2018.
- [18] Gunjan Agarwal, Nicolas Besuchet, Basile Audergon, and Jamie Paik. Stretchable materials for robust soft actuators towards assistive wearable devices. *Scientific reports*, 6:34224, 2016.
- [19] Daniela Rus and Michael T Tolley. Design, fabrication and control of soft robots. *Nature*, 521(7553):467–475, 2015.
- [20] Hong Kai Yap, Benjamin WK Ang, Jeong Hoon Lim, James CH Goh, and Chen-Hua Yeow. A fabric-regulated soft robotic glove with user intent detection using emg and rfid for hand assistive application. In *Robotics and Automation (ICRA), 2016 IEEE International Conference on*, pages 3537–3542. IEEE, 2016.

-
- [21] ROAM Robotics Lab. <http://www.roamrobotics.com/>. Accessed: 05-11-2017.
- [22] Michael Wehner, Brendan Quinlivan, Patrick M Aubin, Ernesto Martinez-Villalpando, Michael Baumann, Leia Stirling, Kenneth Holt, Robert Wood, and Conor Walsh. A lightweight soft exosuit for gait assistance. In *Robotics and Automation (ICRA), 2013 IEEE International Conference on*, pages 3362–3369. IEEE, 2013.
- [23] Matthew Aaron Robertson and Jamie Paik. Trunk postural tracking of assistive soft pneumatic actuator belt. In *Dynamic Walking Conference*, number EPFL-TALK-231820, 2016.
- [24] Deepak Trivedi, Amir Lotfi, and Christopher D Rahn. Geometrically exact models for soft robotic manipulators. *IEEE Transactions on Robotics*, 24(4):773–780, 2008.
- [25] Panagiotis Polygerinos, Zheng Wang, Johannes TB Overvelde, Kevin C Galloway, Robert J Wood, Katia Bertoldi, and Conor J Walsh. Modeling of soft fiber-reinforced bending actuators. *IEEE Transactions on Robotics*, 31(3):778–789, 2015.
- [26] Ming Luo, Mahdi Agheli, and Cagdas D Onal. Theoretical modeling and experimental analysis of a pressure-operated soft robotic snake. *Soft Robotics*, 1(2):136–146, 2014.
- [27] Valentin Falkenhahn, Alexander Hildebrandt, Rüdiger Neumann, and Oliver Sawodny. Model-based feedforward position control of constant curvature continuum robots using feedback linearization. In *Robotics and Automation (ICRA), 2015 IEEE International Conference on*, pages 762–767. IEEE, 2015.
- [28] Andrew D Marchese and Daniela Rus. Design, kinematics, and control of a soft spatial fluidic elastomer manipulator. *The International Journal of Robotics Research*, 35(7):840–869, 2016.
- [29] Andrew D Marchese, Russ Tedrake, and Daniela Rus. Dynamics and trajectory optimization for a soft spatial fluidic elastomer manipulator. *The International Journal of Robotics Research*, 35(8):1000–1019, 2016.
- [30] Cosimo Della Santina, Robert K Katzschmann, Antonio Bicchi, and Daniela Rus. Dynamic control of soft robots interacting with the environment. In *IEEE International Conference on Soft Robotics 2018*. IEEE, 2018.
- [31] Christian Duriez. Control of elastic soft robots based on real-time finite element method. In *Robotics and Automation (ICRA), 2013 IEEE International Conference on*, pages 3982–3987. IEEE, 2013.
- [32] Philip Moseley, Juan Manuel Florez, Harshal Arun Sonar, Gunjan Agarwal, William Curtin, and Jamie Paik. Modeling, design, and development of soft pneumatic actuators with finite element method. *Advanced Engineering Materials*, 18(6):978–988, 2016.

- [33] Heather Culbertson, Samuel B Schorr, and Allison M Okamura. Haptics: The present and future of artificial touch sensation. *Annual Review of Control, Robotics, and Autonomous Systems*, 1:385–409, 2018.
- [34] Francesco Chinello, Monica Malvezzi, Domenico Prattichizzo, and Claudio Pacchierotti. A modular wearable finger interface for cutaneous and kinesthetic interaction: control and evaluation. *IEEE Transactions on Industrial Electronics*, 67(1):706–716, 2019.
- [35] Daniele Leonardis, Massimiliano Solazzi, Ilaria Bortone, and Antonio Frisoli. A 3-rsr haptic wearable device for rendering fingertip contact forces. *IEEE transactions on haptics*, 10(3):305–316, 2016.
- [36] Sagar Joshi and Jamie Paik. Multi-dof force characterization of soft actuators. *IEEE Robotics and Automation Letters*, 4(4):3679–3686, 2019.
- [37] Ramses V Martinez, Ana C Glavan, Christoph Keplinger, Alexis I Oyetibo, and George M Whitesides. Soft actuators and robots that are resistant to mechanical damage. *Advanced Functional Materials*, 24(20):3003–3010, 2014.
- [38] Yong-Lae Park, Jobim Santos, Kevin G Galloway, Eugene C Goldfield, and Robert J Wood. A soft wearable robotic device for active knee motions using flat pneumatic artificial muscles. In *Robotics and Automation (ICRA), 2014 IEEE International Conference on*, pages 4805–4810. IEEE, 2014.
- [39] Harshal Arun Sonar and Jamie Paik. Soft pneumatic actuator skin with piezoelectric sensors for vibrotactile feedback. *Frontiers in Robotics and AI*, 2:38, 2016.
- [40] Hong Kai Yap, Nazir Kamaldin, Jeong Hoon Lim, Fatima Nasrallah, James CH Goh, and Chen-Hua Yeow. A magnetic resonance compatible soft wearable robotic glove for hand rehabilitation and brain imaging. *IEEE transactions on neural systems and rehabilitation engineering*, 2016.
- [41] Victoria Oguntosin, William S Harwin, Sadao Kawamura, Slawomir J Nasuto, and Yoshikatsu Hayashi. Development of a wearable assistive soft robotic device for elbow rehabilitation. In *Rehabilitation Robotics (ICORR), 2015 IEEE International Conference on*, pages 747–752. IEEE, 2015.
- [42] Michael T Tolley, Robert F Shepherd, Bobak Mosadegh, Kevin C Galloway, Michael Wehner, Michael Karpelson, Robert J Wood, and George M Whitesides. A resilient, untethered soft robot. *Soft Robotics*, 1(3):213–223, 2014.
- [43] Robert F Shepherd, Filip Ilievski, Wonjae Choi, Stephen A Morin, Adam A Stokes, Aaron D Mazzeo, Xin Chen, Michael Wang, and George M Whitesides. Multigait soft robot. *Proceedings of the National Academy of Sciences*, 108(51):20400–20403, 2011.
- [44] Cagdas D Onal and Daniela Rus. Autonomous undulatory serpentine locomotion utilizing body dynamics of a fluidic soft robot. *Bioinspiration & biomimetics*, 8(2):026003, 2013.

-
- [45] Andrew D Marchese, Cagdas D Onal, and Daniela Rus. Autonomous soft robotic fish capable of escape maneuvers using fluidic elastomer actuators. *Soft Robotics*, 1(1):75–87, 2014.
- [46] Jiawei Cao, Lei Qin, Jun Liu, Qinyuan Ren, Choon Chiang Foo, Hongqiang Wang, Heow Pueh Lee, and Jian Zhu. Untethered soft robot capable of stable locomotion using soft electrostatic actuators. *Extreme Mechanics Letters*, 21:9–16, 2018.
- [47] Adam A Stokes, Robert F Shepherd, Stephen A Morin, Filip Ilievski, and George M Whitesides. A hybrid combining hard and soft robots. *Soft Robotics*, 1(1):70–74, 2014.
- [48] Filip Ilievski, Aaron D Mazzeo, Robert F Shepherd, Xin Chen, and George M Whitesides. Soft robotics for chemists. *Angewandte Chemie*, 123(8):1930–1935, 2011.
- [49] Mariangela Manti, Taimoor Hassan, Giovanni Passetti, Nicolò D’Elia, Cecilia Laschi, and Matteo Cianchetti. A bioinspired soft robotic gripper for adaptable and effective grasping. *Soft Robotics*, 2(3):107–116, 2015.
- [50] Federico Renda, Michele Girelli, Marcello Calisti, Matteo Cianchetti, and Cecilia Laschi. Dynamic model of a multibending soft robot arm driven by cables. *IEEE Transactions on Robotics*, 30(5):1109–1122, 2014.
- [51] François Faure, Christian Duriez, Hervé Delingette, Jérémie Allard, Benjamin Gilles, Stéphanie Marchesseau, Hugo Talbot, Hadrien Courtecuisse, Guillaume Bousquet, Igor Peterlik, et al. Sofa: A multi-model framework for interactive physical simulation. In *Soft Tissue Biomechanical Modeling for Computer Assisted Surgery*, pages 283–321. Springer, 2012.
- [52] Cagdas D Onal and Daniela Rus. A modular approach to soft robots. In *Biomedical Robotics and Biomechatronics (BioRob), 2012 4th IEEE RAS & EMBS International Conference on*, pages 1038–1045. IEEE, 2012.
- [53] Yoel Shapiro, Alon Wolf, and Kosa Gabor. Bi-bellows: Pneumatic bending actuator. *Sensors and Actuators A: Physical*, 167(2):484–494, 2011.
- [54] Andrew D Marchese, Robert K Katzschmann, and Daniela Rus. A recipe for soft fluidic elastomer robots. *Soft Robotics*, 2(1):7–25, 2015.
- [55] Zheng Wang, Panagiotis Polygerinos, Johannes TB Overvelde, Kevin C Galloway, Katia Bertoldi, and Conor J Walsh. Interaction forces of soft fiber reinforced bending actuators. *IEEE/ASME Transactions on Mechatronics*, 22(2):717–727, 2017.
- [56] Yong-Lae Park, Bor-rong Chen, Carmel Majidi, Robert J Wood, Radhika Nagpal, and Eugene Goldfield. Active modular elastomer sleeve for soft wearable assistance robots. In *Intelligent Robots and Systems (IROS), 2012 IEEE/RSJ International Conference on*, pages 1595–1602. IEEE, 2012.

- [57] Yi Sun, Yun Seong Song, and Jamie Paik. Characterization of silicone rubber based soft pneumatic actuators. In *2013 IEEE/RSJ International Conference on Intelligent Robots and Systems*, pages 4446–4453. Ieee, 2013.
- [58] Guoying Gu, Jiang Zou, Ruike Zhao, Xuanhe Zhao, and Xiangyang Zhu. Soft wall-climbing robots. *Science Robotics*, 3(25):eaat2874, 2018.
- [59] Huaxia Guo, Jinhua Zhang, Tao Wang, Yuanjie Li, Jun Hong, and Yue Li. Design and control of an inchworm-inspired soft robot with omega-arching locomotion. In *2017 IEEE International Conference on Robotics and Automation (ICRA)*, pages 4154–4159. IEEE, 2017.
- [60] Matthew A Robertson, Hamed Sadeghi, Juan Manuel Florez, and Jamie Paik. Soft pneumatic actuator fascicles for high force and reliability. *Soft Robotics*, 4(1):23–32, 2017.
- [61] Frederic H Giraud, Sagar Joshi, and Jamie Paik. Haptigami: a fingertip haptic interface with vibrotactile and 3-dof cutaneous force feedback. *IEEE Transactions on Haptics (under review)*, 2021.
- [62] James Cannan and Huosheng Hu. Human-machine interaction (hmi): A survey. *University of Essex*, 2011.
- [63] Tyler Rose, Chang S Nam, and Karen B Chen. Immersion of virtual reality for rehabilitation-review. *Applied ergonomics*, 69:153–161, 2018.
- [64] Nooshin Jafari, Kim D Adams, and Mahdi Tavakoli. Haptics to improve task performance in people with disabilities: A review of previous studies and a guide to future research with children with disabilities. *Journal of rehabilitation and assistive technologies engineering*, 3:2055668316668147, 2016.
- [65] Dylan P Losey, Craig G McDonald, Edoardo Battaglia, and Marcia K O’Malley. A review of intent detection, arbitration, and communication aspects of shared control for physical human–robot interaction. *Applied Mechanics Reviews*, 70(1):010804, 2018.
- [66] Niels Christian Nilsson, Stefania Serafin, Frank Steinicke, and Rolf Nordahl. Natural walking in virtual reality: A review. *Computers in Entertainment (CIE)*, 16(2):8, 2018.
- [67] Claudio Pacchierotti, Stephen Sinclair, Massimiliano Solazzi, Antonio Frisoli, Vincent Hayward, and Domenico Prattichizzo. Wearable haptic systems for the fingertip and the hand: taxonomy, review, and perspectives. *IEEE transactions on haptics*, 10(4):580–600, 2017.
- [68] Claudio Pacchierotti, Asad Tirmizi, and Domenico Prattichizzo. Improving transparency in teleoperation by means of cutaneous tactile force feedback. *ACM Transactions on Applied Perception (TAP)*, 11(1):1–16, 2014.

-
- [69] Francesco Chinello, Monica Malvezzi, Claudio Pacchierotti, and Domenico Prattichizzo. Design and development of a 3rrs wearable fingertip cutaneous device. In *2015 IEEE International Conference on Advanced Intelligent Mechatronics (AIM)*, pages 293–298. IEEE, 2015.
- [70] Daniele Leonardis, Massimiliano Solazzi, Ilaria Bortone, and Antonio Frisoli. A wearable fingertip haptic device with 3 dof asymmetric 3-rsr kinematics. In *2015 IEEE World Haptics Conference (WHC)*, pages 388–393. IEEE, 2015.
- [71] Samuel Benjamin Schorr and Allison M Okamura. Three-dimensional skin deformation as force substitution: Wearable device design and performance during haptic exploration of virtual environments. *IEEE transactions on haptics*, 10(3):418–430, 2017.
- [72] F. Chinello, C. Pacchierotti, M. Malvezzi, and D. Prattichizzo. A three revolute-revolute-spherical wearable fingertip cutaneous device for stiffness rendering. *IEEE Transactions on Haptics*, 11(1):39–50, 2018.
- [73] Y. Mo, A. Song, and H. Qin. Analysis and performance evaluation of a 3-dof wearable fingertip device for haptic applications. *IEEE Access*, 7:170430–170441, 2019.
- [74] Steven A Wall and William Harwin. A high bandwidth interface for haptic human computer interaction. *Mechatronics*, 11(4):371–387, 2001.
- [75] Susan J Lederman and Roberta L Klatzky. Sensing and displaying spatially distributed fingertip forces in haptic interfaces for teleoperator and virtual environment systems. *Presence: Teleoperators & Virtual Environments*, 8(1):86–103, 1999.
- [76] Sagar Joshi and Jamie Paik. Pneumatic supply system parameter optimization for soft actuators. *Soft Robotics*, 2020.
- [77] Sagar Joshi, Harshal Arun Sonar, and Jamie Paik. Flow path optimization for soft pneumatic actuators - towards optimal performance and portability. *IEEE Robotics and Automation Letters (under review)*, 2021.
- [78] Michael Wehner, Ryan L Truby, Daniel J Fitzgerald, Bobak Mosadegh, George M Whitesides, Jennifer A Lewis, and Robert J Wood. An integrated design and fabrication strategy for entirely soft, autonomous robots. *Nature*, 536(7617):451–455, 2016.
- [79] Laura Paez, Gunjan Agarwal, and Jamie Paik. Design and analysis of a soft pneumatic actuator with origami shell reinforcement. *Soft Robotics*, 3(3):109–119, 2016.
- [80] Fionnuala Connolly, Conor J Walsh, and Katia Bertoldi. Automatic design of fiber-reinforced soft actuators for trajectory matching. *Proceedings of the National Academy of Sciences*, 114(1):51–56, 2017.
- [81] Ellen T Roche, Robert Wohlfarth, Johannes TB Overvelde, Nikolay V Vasilyev, Frank A Pigula, David J Mooney, Katia Bertoldi, and Conor J Walsh. A bioinspired soft actuated material. *Advanced Materials*, 26(8):1200–1206, 2014.

- [82] Michael Wehner, Michael T Tolley, Yiğit Mengüç, Yong-Lae Park, Annan Mozeika, Ye Ding, Cagdas Onal, Robert F Shepherd, George M Whitesides, and Robert J Wood. Pneumatic energy sources for autonomous and wearable soft robotics. *Soft Robotics*, 1(4):263–274, 2014.
- [83] Boran Wang, Andrew McDaid, Morteza Biglari-Abhari, Timothy Giffney, and Kean Aw. A bimorph pneumatic bending actuator by control of fiber braiding angle. *Sensors and Actuators A: Physical*, 257:173–184, 2017.
- [84] ISO 6358-1:2013. <https://www.iso.org/standard/56612.html>. Accessed: 10-12-2017.
- [85] Peter Beater. *Pneumatic drives*. Springer, 2007.
- [86] Bong-Soo Kang, Curt S Kothera, Benjamin KS Woods, and Norman M Wereley. Dynamic modeling of mckibben pneumatic artificial muscles for antagonistic actuation. In *Robotics and Automation, 2009. ICRA'09. IEEE International Conference on*, pages 182–187. IEEE, 2009.
- [87] Takashi Itto and Kiminao Kogiso. Hybrid modeling of mckibben pneumatic artificial muscle systems. In *Industrial Technology (ICIT), 2011 IEEE International Conference on*, pages 65–70. IEEE, 2011.
- [88] Xiangrong Shen. Nonlinear model-based control of pneumatic artificial muscle servo systems. *Control Engineering Practice*, 18(3):311–317, 2010.
- [89] T Nguyen, J Leavitt, F Jabbari, and JE Bobrow. Accurate sliding-mode control of pneumatic systems using low-cost solenoid valves. *IEEE/ASME Transactions on mechatronics*, 12(2):216–219, 2007.
- [90] Paul G Harris, Garret E O'Donnell, and Tom Whelan. Modelling and identification of industrial pneumatic drive system. *The International Journal of Advanced Manufacturing Technology*, 58(9-12):1075–1086, 2012.
- [91] Kenji Kawashima, Yukio Ishii, Tatsuya Funaki, and Toshiharu Kagawa. Determination of flow rate characteristics of pneumatic solenoid valves using an isothermal chamber. *J. Fluids Eng.*, 126(2):273–279, 2004.
- [92] Ma Jungong, Chen Juan, Zhao Ke, and Mitsuru Senoo. Flow-rate characteristics parameters of pneumatic component. In *2008 IEEE International Conference on Automation and Logistics*, pages 2946–2949. IEEE, 2008.
- [93] Massimo Sorli and Stefano Pastorelli. Performance of a pneumatic force controlling servosystem: influence of valves conductance. *Robotics and Autonomous Systems*, 30(3):283–300, 2000.
- [94] Xiaoxia Cheng, Linglong Du, Gang Yang, and Baoren Li. Adaptive robust control of dynamic gas pressure in a vacuum servo system. *Vacuum*, 148:184–194, 2018.

-
- [95] Mitsuru Senoo, Huping ZHANG, and Naotake ONEYAMA. Study and suggestions on pneumatic component flow-rate characteristics. In *Proceedings of the JFPS International Symposium on Fluid Power*, volume 2002, pages 67–72. The Japan Fluid Power System Society, 2002.
- [96] Kiyoshi KUROSHITA. Study on measurement method of flow-rate characteristics of pneumatic solenoid valve. In *Proceedings of the JFPS International Symposium on Fluid Power*, volume 2002, pages 73–78. The Japan Fluid Power System Society, 2002.
- [97] SMC - Flow rate calculator. https://www.smc.eu/portal_ssl/webpages/01_products/engineering_tools/flow_rate_calculator/flow_rate_calculator.jsp, 2021. Accessed: 03-12-2017.
- [98] J Eckersten. Simplified flow calculations for pneumatic components. *Atlas Copco Air Compendium*. Atlas Copco AB, Tukholma, pages 183–192, 1975.
- [99] Aventics Pneumatic calculator/converter. https://www.aventics.com/computation/converter/flow_converter.jsp, 2021. Accessed: 10-11-2020.
- [100] Harshal A Sonar, Aaron P Gerratt, Stéphanie P Lacour, and Jamie Paik. Closed-loop haptic feedback control using a self-sensing soft pneumatic actuator skin. *Soft robotics*, 7(1):22–29, 2020.
- [101] R Adam Bilodeau, Edward L White, and Rebecca K Kramer. Monolithic fabrication of sensors and actuators in a soft robotic gripper. In *2015 IEEE/RSJ International Conference on Intelligent Robots and Systems (IROS)*, pages 2324–2329. IEEE, 2015.
- [102] Gabriele Frediani and Federico Carpi. Tactile display of softness on fingertip. *Scientific reports*, 10(1):1–10, 2020.
- [103] Seppe Terryn, Joost Brancart, Dirk Lefeber, Guy Van Assche, and Bram Vanderborght. Self-healing soft pneumatic robots. *Science Robotics*, 2(9), 2017.
- [104] Kousei Miura, Hideki Kadone, Masao Koda, Tetsuya Abe, Hiroshi Kumagai, Katsuya Nagashima, Kentaro Mataka, Kengo Fujii, Hiroshi Noguchi, Toru Funayama, et al. The hybrid assistive limb (hal) for care support successfully reduced lumbar load in repetitive lifting movements. *Journal of Clinical Neuroscience*, 53:276–279, 2018.
- [105] Matthew Millard, Manish Sreenivasa, and Katja Mombaur. Predicting the motions and forces of wearable robotic systems using optimal control. *Frontiers in Robotics and AI*, 4:41, 2017.
- [106] Stefano Toxiri, Jesús Ortiz, Jawad Masood, Jorge Fernández, Luis A Mateos, and Darwin G Caldwell. A wearable device for reducing spinal loads during lifting tasks: Biomechanics and design concepts. In *Robotics and Biomimetics (ROBIO), 2015 IEEE International Conference on*, pages 2295–2300. IEEE, 2015.

Bibliography

- [107] Cota Nabeshima, Ko Ayusawa, Conrad Hochberg, and Eiichi Yoshida. Standard performance test of wearable robots for lumbar support. *IEEE Robotics and Automation Letters*, 3(3):2182–2189, 2018.
- [108] Baojun Chen, Lorenzo Grazi, Francesco Lanotte, Nicola Vitiello, and Simona Crea. A real-time lift detection strategy for a hip exoskeleton. *Frontiers in neurorobotics*, 12:17, 2018.
- [109] Khaled Elgeneidy, Niels Lohse, and Michael Jackson. Bending angle prediction and control of soft pneumatic actuators with embedded flex sensors—a data-driven approach. *Mechatronics*, 50:234–247, 2018.
- [110] Giada Gerboni, Alessandro Diodato, Gastone Ciuti, Matteo Cianchetti, and Arianna Menciassi. Feedback control of soft robot actuators via commercial flex bend sensors. *IEEE/ASME Transactions on Mechatronics*, 22(4):1881–1888, 2017.
- [111] Andreas Frutiger, Joseph T Muth, Daniel M Vogt, Yiğit Mengüç, Alexandre Campo, Alexander D Valentine, Conor J Walsh, and Jennifer A Lewis. Capacitive soft strain sensors via multicore-shell fiber printing. *Advanced Materials*, 27(15):2440–2446, 2015.
- [112] Sanlin S Robinson, Kevin W O’Brien, Huichan Zhao, Bryan N Peele, Chris M Larson, Benjamin C Mac Murray, Ilse M Van Meerbeek, Simon N Dunham, and Robert F Shepherd. Integrated soft sensors and elastomeric actuators for tactile machines with kinesthetic sense. *Extreme Mechanics Letters*, 5:47–53, 2015.
- [113] Yufei Hao, Tianmiao Wang, Zhexin Xie, Wenguang Sun, Zemin Liu, Xi Fang, Minxuan Yang, and Li Wen. A eutectic-alloy-infused soft actuator with sensing, tunable degrees of freedom, and stiffness properties. *Journal of Micromechanics and Microengineering*, 28(2):024004, 2018.
- [114] Vincent Wall, Gabriel Zöllner, and Oliver Brock. A method for sensorizing soft actuators and its application to the rbo hand 2. In *2017 IEEE International Conference on Robotics and Automation (ICRA)*, pages 4965–4970. IEEE, 2017.
- [115] Michelle C Yuen, Henry Tonoyan, Edward L White, Maria Telleria, and Rebecca K Kramer. Fabric sensory sleeves for soft robot state estimation. In *2017 IEEE international conference on robotics and automation (ICRA)*, pages 5511–5518. IEEE, 2017.
- [116] Michelle C Yuen, Rebecca Kramer-Bottiglio, and Jamie Paik. Strain sensor-embedded soft pneumatic actuators for extension and bending feedback. In *2018 IEEE International Conference on Soft Robotics (RoboSoft)*, pages 202–207. IEEE, 2018.
- [117] Selim Ozel, Nehir A Keskin, Darien Khea, and Cagdas D Onal. A precise embedded curvature sensor module for soft-bodied robots. *Sensors and Actuators A: Physical*, 236:349–356, 2015.

-
- [118] Tess Hellebrekers, Nadine Chang, Keene Chin, Michael Ford, Oliver Kroemer, and Carmel Majidi. Soft magnetic tactile skin for continuous force and location estimation using neural networks. *IEEE Robotics and Automation Letters*, 2020.
- [119] Benjamin Ward-Cherrier, Nicholas Pestell, Luke Cramphorn, Benjamin Winstone, Maria Elena Giannaccini, Jonathan Rossiter, and Nathan F Lepora. The tactip family: Soft optical tactile sensors with 3d-printed biomimetic morphologies. *Soft robotics*, 5(2):216–227, 2018.
- [120] Wenzhen Yuan, Siyuan Dong, and Edward H Adelson. Gelsight: High-resolution robot tactile sensors for estimating geometry and force. *Sensors*, 17(12):2762, 2017.
- [121] Hui Yang, Yang Chen, Yao Sun, and Lina Hao. A novel pneumatic soft sensor for measuring contact force and curvature of a soft gripper. *Sensors and Actuators A: Physical*, 266:318–327, 2017.
- [122] Charbel Tawk, Marc in het Panhuis, Geoffrey M Spinks, and Gursel Alici. Soft pneumatic sensing chambers for generic and interactive human–machine interfaces. *Advanced Intelligent Systems*, 1(1):1900002, 2019.
- [123] John Morrow, Hee-Sup Shin, Calder Phillips-Grafflin, Sung-Hwan Jang, Jacob Torrey, Riley Larkins, Steven Dang, Yong-Lae Park, and Dmitry Berenson. Improving soft pneumatic actuator fingers through integration of soft sensors, position and force control, and rigid fingernails. In *ICRA*, pages 5024–5031, 2016.
- [124] Takashi Takizawa, Takahiro Kanno, Ryoken Miyazaki, Kotaro Tadano, and Kenji Kawashima. Grasping force estimation in robotic forceps using a soft pneumatic actuator with a built-in sensor. *Sensors and Actuators A: Physical*, 271:124–130, 2018.
- [125] Jianshu Zhou, Yonghua Chen, Xiaojiao Chen, Zheng Wang, Yunquan Li, and Yunhui Liu. A proprioceptive bellows (pb) actuator with position feedback and force estimation. *IEEE Robotics and Automation Letters*, 5(2):1867–1874, 2020.
- [126] Thomas George Thuruthel, Benjamin Shih, Cecilia Laschi, and Michael Thomas Tolley. Soft robot perception using embedded soft sensors and recurrent neural networks. *Science Robotics*, 4(26):eaav1488, 2019.
- [127] Paul P Acarnley and John F Watson. Review of position-sensorless operation of brushless permanent-magnet machines. *IEEE Transactions on Industrial Electronics*, 53(2):352–362, 2006.
- [128] H Gurung and A Banerjee. Self-sensing shape memory alloy wire actuator based on unscented kalman filter. *Sensors and Actuators A: Physical*, 251:258–265, 2016.
- [129] Filomena Simone, Gianluca Rizzello, and Stefan Seelecke. Metal muscles and nerves—a self-sensing sma-actuated hand concept. *Smart Materials and Structures*, 26(9):095007, 2017.

Bibliography

- [130] Hideyuki Ikeda and Takeshi Morita. High-precision positioning using a self-sensing piezoelectric actuator control with a differential detection method. *Sensors and Actuators A: Physical*, 170(1-2):147–155, 2011.
- [131] Katsuhiro Saigusa and Takeshi Morita. Self-sensing control of piezoelectric positioning stage by detecting permittivity. *Sensors and Actuators A: Physical*, 226:76–80, 2015.
- [132] Kwangmok Jung, Kwang J Kim, and Hyouk Ryeol Choi. A self-sensing dielectric elastomer actuator. *Sensors and Actuators A: Physical*, 143(2):343–351, 2008.
- [133] Gianluca Rizzello, David Naso, Alexander York, and Stefan Seelecke. A self-sensing approach for dielectric elastomer actuators based on online estimation algorithms. *IEEE/ASME Transactions on Mechatronics*, 22(2):728–738, 2016.
- [134] Gianluca Rizzello, Federica Fugaro, David Naso, and Stefan Seelecke. Simultaneous self-sensing of displacement and force for soft dielectric elastomer actuators. *IEEE Robotics and Automation Letters*, 3(2):1230–1236, 2018.
- [135] Joost van der Weijde, Bram Smit, Michael Fritschi, Cornelis van de Kamp, and Heike Vallery. Self-sensing of deflection, force, and temperature for joule-heated twisted and coiled polymer muscles via electrical impedance. *IEEE/ASME Transactions on Mechatronics*, 22(3):1268–1275, 2016.
- [136] Manuel Schimmack, Benedikt Haus, and Paolo Mercorelli. An extended kalman filter as an observer in a control structure for health monitoring of a metal–polymer hybrid soft actuator. *IEEE/ASME Transactions on Mechatronics*, 23(3):1477–1487, 2018.
- [137] Anuj Karpatne, William Watkins, Jordan Read, and Vipin Kumar. Physics-guided neural networks (pgnn): An application in lake temperature modeling. *arXiv preprint arXiv:1710.11431*, 2017.
- [138] Rik Op De Beeck and Veerle Hermans. work-related low back disorders. *Bilbao, Spain*, 2000.
- [139] A Parent-Thirion, G Vermeylen, G Van Houten, M LYLY-YRJÄNÄINEN, I BILETTA, and J CABRITA. Fifth european working conditions survey luxembourg: Eurofound. *Publications Office of the European Union*, 10:34660, 2012.
- [140] European Agency for Safety and Zinta Podniece Health at Work. Work-related musculoskeletal disorders: Back to work report. 2007.
- [141] Tim Bosch, Jennifer van Eck, Karlijn Knitel, and Michiel de Looze. The effects of a passive exoskeleton on muscle activity, discomfort and endurance time in forward bending work. *Applied ergonomics*, 54:212–217, 2016.
- [142] Axel S Koopman, Idsart Kingma, Gert S Faber, Michiel P de Looze, and Jaap H van Dieën. Effects of a passive exoskeleton on the mechanical loading of the low back in static holding tasks. *Journal of biomechanics*, 83:97–103, 2019.

-
- [143] Axel S Koopman, Idsart Kingma, Michiel P de Looze, and Jaap H van Dieën. Effects of a passive back exoskeleton on the mechanical loading of the low-back during symmetric lifting. *Journal of biomechanics*, 102:109486, 2020.
- [144] SJ Baltrusch, JH Van Dieën, SM Bruijn, AS Koopman, CAM Van Bennekom, and Han Houdijk. The effect of a passive trunk exoskeleton on metabolic costs during lifting and walking. *Ergonomics*, 2019.
- [145] Brent L Ulrey and Fadi A Fathallah. Effect of a personal weight transfer device on muscle activities and joint flexions in the stooped posture. *Journal of Electromyography and Kinesiology*, 23(1):195–205, 2013.
- [146] Brent L Ulrey and Fadi A Fathallah. Subject-specific, whole-body models of the stooped posture with a personal weight transfer device. *Journal of Electromyography and Kinesiology*, 23(1):206–215, 2013.
- [147] Jan Babič, Katja Mombaur, Dirk Lefebvre, Jaap van Dieën, Bernhard Graimann, Michael Russold, Nejc Šarabon, and Han Houdijk. Spexor: Spinal exoskeletal robot for low back pain prevention and vocational reintegration. In *Wearable Robotics: Challenges and Trends*, pages 311–315. Springer, 2017.
- [148] Monika Harant, Manish Sreenivasa, Matthew Millard, Nejc Šarabon, and Katja Mombaur. Parameter optimization for passive spinal exoskeletons based on experimental data and optimal control. In *2017 IEEE-RAS 17th International Conference on Humanoid Robotics (Humanoids)*, pages 535–540. IEEE, 2017.
- [149] SJ Baltrusch, JH Van Dieën, AS Koopman, MB Näf, C Rodriguez-Guerrero, J Babič, and H Houdijk. Spexor passive spinal exoskeleton decreases metabolic cost during symmetric repetitive lifting. *European journal of applied physiology*, 120(2):401–412, 2020.
- [150] Axel S Koopman, Matthias Näf, Saskia J Baltrusch, Idsart Kingma, Carlos Rodriguez-Guerrero, Jan Babič, Michiel P de Looze, and Jaap H van Dieën. Biomechanical evaluation of a new passive back support exoskeleton. *Journal of Biomechanics*, 105:109795, 2020.
- [151] KS Stadler, Wilfried J Elspass, and Hans Wernher van de Venn. Robo-mate: Exoskeleton to enhance industrial production: Special session: Exoskeletons for emerging applications. In *Mobile Service Robotics*, pages 53–60. World Scientific, 2014.
- [152] Kirsten Huysamen, Michiel de Looze, Tim Bosch, Jesus Ortiz, Stefano Toxiri, and Leonard W O’Sullivan. Assessment of an active industrial exoskeleton to aid dynamic lifting and lowering manual handling tasks. *Applied ergonomics*, 68:125–131, 2018.
- [153] Kousei Miura, Hideki Kadone, Tetsuya Abe, Masao Koda, Toru Funayama, Hiroshi Noguchi, Hiroshi Kumagai, Katsuya Nagashima, Kentaro Mataka, Yosuke Shibao, et al.

- Successful use of the hybrid assistive limb for care support to reduce lumbar load in a simulated patient transfer. *Asian spine journal*, 15(1):40, 2021.
- [154] Wei Wei, Shijia Zha, Yuxuan Xia, Jihua Gu, and Xichuan Lin. A hip active assisted exoskeleton that assists the semi-squat lifting. *Applied Sciences*, 10(7):2424, 2020.
- [155] Hun Keon Ko, Seok Won Lee, Dong Han Koo, Inju Lee, and Dong Jin Hyun. Waist-assistive exoskeleton powered by a singular actuation mechanism for prevention of back-injury. *Robotics and Autonomous Systems*, 107:1–9, 2018.
- [156] Yuichi Muramatsu, Hideyuki Umehara, and Hideo Kobayashi. Improvement and quantitative performance estimation of the back support muscle suit. In *Engineering in Medicine and Biology Society (EMBC), 2013 35th Annual International Conference of the IEEE*, pages 2844–2849. IEEE, 2013.
- [157] Mohammad Abdoli-e, Michael J Agnew, and Joan M Stevenson. An on-body personal lift augmentation device (plad) reduces emg amplitude of erector spinae during lifting tasks. *Clinical Biomechanics*, 21(5):456–465, 2006.
- [158] David M Frost, Mohammad Abdoli-E, and Joan M Stevenson. Plad (personal lift assistive device) stiffness affects the lumbar flexion/extension moment and the posterior chain emg during symmetrical lifting tasks. *Journal of Electromyography and Kinesiology*, 19(6):e403–e412, 2009.
- [159] Ryan B Graham, Michael J Agnew, and Joan M Stevenson. Effectiveness of an on-body lifting aid at reducing low back physical demands during an automotive assembly task: Assessment of emg response and user acceptability. *Applied Ergonomics*, 40(5):936–942, 2009.
- [160] Erin M Sadler, Ryan B Graham, and Joan M Stevenson. The personal lift-assist device and lifting technique: a principal component analysis. *Ergonomics*, 54(4):392–402, 2011.
- [161] Erik P Lamers, Aaron J Yang, and Karl E Zelik. Feasibility of a biomechanically-assistive garment to reduce low back loading during leaning and lifting. *IEEE Transactions on Biomedical Engineering*, 65(8):1674–1680, 2017.
- [162] Erik P Lamers, Juliana C Soltys, Keaton L Scherpereel, Aaron J Yang, and Karl E Zelik. Low-profile elastic exosuit reduces back muscle fatigue. *Scientific Reports*, 10(1):1–16, 2020.
- [163] Erik P Lamers and Karl E Zelik. Design, modeling, and demonstration of a new dual-mode back-assist exosuit with extension mechanism. *Wearable Technologies*, 2, 2021.
- [164] Zhejun Yao, Christine Linnenberg, Robert Weidner, and Jens Wulfsberg. Development of a soft power suit for lower back assistance. In *2019 International Conference on Robotics and Automation (ICRA)*, pages 5103–5109. IEEE, 2019.

-
- [165] Michele Xiloyannis, Ryan Alicea, Anna-Maria Georgarakis, Florian L Haufe, Peter Wolf, Lorenzo Masia, and Robert Riener. Soft robotic suits: State of the art, core technologies, and open challenges. *IEEE Transactions on Robotics*, 2021.
- [166] Alexander G Bruno, Mary L Bouxsein, and Dennis E Anderson. Development and validation of a musculoskeletal model of the fully articulated thoracolumbar spine and rib cage. *Journal of biomechanical engineering*, 137(8), 2015.
- [167] Darryl G Thelen. Adjustment of muscle mechanics model parameters to simulate dynamic contractions in older adults. *J. Biomech. Eng.*, 125(1):70–77, 2003.
- [168] Scott L Delp, Frank C Anderson, Allison S Arnold, Peter Loan, Ayman Habib, Chand T John, Eran Guendelman, and Darryl G Thelen. Opensim: open-source software to create and analyze dynamic simulations of movement. *IEEE transactions on biomedical engineering*, 54(11):1940–1950, 2007.
- [169] Patrick Kofod Mogensen, Kristoffer Carlsson, Sébastien Villemot, Spencer Lyon, Matthieu Gomez, Christopher Rackauckas, Tim Holy, David Widmann, Tony Kelman, Daniel Karrasch, Antoine Levitt, Asbjørn Nilsen Riseth, Carlo Lucibello, Changhyun Kwon, David Barton, Julia TagBot, Mateusz Baran, Miles Lubin, Sarthak Choudhury, Simon Byrne, Simon Christ, Takafumi Arakaki, Troels Arnfred Bojesen, benneti, and Miguel Raz Guzmán Macedo. Julianlsolvers/nlsolve.jl: v4.5.1, December 2020.
- [170] Frederic H Giraud, Zhenishbek Zhakypov, and Jamie Paik. Design of low-profile compliant transmission mechanisms. In *2019 IEEE/RSJ International Conference on Intelligent Robots and Systems (IROS)*, pages 2700–2707. IEEE, 2019.
- [171] Maple is a trademark of Waterloo Maple Inc. Maple, 2018.
- [172] FE Sanville. Two-level compressed air systems for energy saving. In *The 7th International Fluid Control Symposium, Bath, England, September*, pages 375–383, 1986.
- [173] Mohammad Mehdi Alemi, Jack Geissinger, Athulya A Simon, S Emily Chang, Alan T and Asbeck. A passive exoskeleton reduces peak and mean EMG during symmetric and asymmetric lifting. In *Journal of Electromyography and Kinesiology, Volume 7*, pages 25–34. Elsevier, 2019.
- [174] A Hofste, R. Soer, E. Salomons, J. Peuscher, A. Wolff, H. van der Hoeven, and H. Hermens. Intramuscular EMG Versus Surface EMG of Lumbar Multifidus and Erector Spinae in Healthy Participants In *Spine*, 45, pages E1319-E1325. IEEE, 2020.
- [175] S. Song, S. Joshi, and J. Paik. CMOS-Inspired Complementary Fluidic Circuits for Soft Robots In *Advanced Science*, pages 2100924. Wiley Online Library, 2021.

Contact Information

MED 1 1513 (Bâtiment MED),
Station 9,
CH-1015 Lausanne

(+41) 78 648 24 30
sagajosh@gmail.com

Education

Ph.D., Robotics and Intelligent Systems

Nov. 2016 - to Oct. 2021

École Polytechnique Fédérale de Lausanne, Switzerland

Master of Technology, Mechanical Engineering (9.72/10)

Jul. 2013 - Jun. 2016

Indian Institute of Technology Bombay, India

Bachelor of Engineering, Mechanical Engineering (74.1%)

Aug. 2009 - May 2013

Sardar Patel College of Engineering (SPCE), Mumbai, India

Research Experience

PhD. Thesis - Design and dynamic analysis of soft robotic systems for wearable robots

École Polytechnique Fédérale de Lausanne, Switzerland

Nov. 2016 to Oct. 2021

- Investigated methods for accurately characterizing the force and displacement of soft actuators. Proposed novel experimental protocol and setup for physically recreating true loading conditions during characterization.
- Studied soft pneumatic actuator dynamic response, and developed comprehensive model for its pressure dynamics. Studied the effect of twelve critical parameters via simulation and experimental testing. Developed multi-objective design optimization for pneumatic supply systems to meet dynamic performance, portability, and user-defined constraints such as mass and size.
- Introduced and investigated a previously unknown self-sensing property of soft pneumatic actuators. Developed data-driven models to estimate force and displacement of soft pneumatic actuators without dedicated sensors.
- Investigated the impact of soft wearable devices on the wearer via design, modelling, testing and biomechanical evaluation of a reconfigurable soft exosuit for assisting human torso.

Master's Thesis - Design and testing of a novel biarticular actuation scheme in lower limb assistive devices

Indian Institute of Technology Bombay, India

Jul. 2014 - Jun. 2016

- Proposed a novel biarticular ankle prosthesis design and conducted biomechanics simulations in OpenSim, that showed reduced muscle and joint forces in healthy leg
- Fabricated and studied three unpowered ankle exoskeletons with a healthy subject in a gait lab to test the biarticular actuation strategy
- Designed a biarticular ankle prosthesis, based on preliminary results from the exoskeleton study

Research Assistant

Indian Institute of Technology Bombay, India

Jul. 2013 - Jun. 2016

Kinematics & Dynamics of Machines Lab: Design and maintenance of experiments for undergraduate students, managing 120 students and 10 TAs, developing a remote lab setup for demonstrating dynamics of machines

Suman Mashruwala Advanced Microengineering Lab: Development of equipment and improving algorithms for micro 3D printer, conducting demonstrations for undergraduate students

Journal Publications

- [J5] Song S., **Joshi S.**, Paik J. "*CMOS-like Analog Fluidics for Soft Robots*" Advanced Science (2021), doi: 10.1002/advs.202100924
- [J4] Giraud F., **Joshi S.**, Paik J. "*Haptigami: a fingertip haptic interface with vibrotactile and 3-DoF kinesthetic force feedback*" IEEE Transactions on Haptics (2021), doi: 10.1109/TOH.2021.3104216
- [J3] **Joshi S.** Sonar H., Paik J. "*Flow path optimization for soft pneumatic actuators: towards optimal performance and portability*" IEEE Robotics and Automation Letters (2021), doi:10.1109/LRA.2021.3100626
- [J2] **Joshi S.**, Paik J. "*Pneumatic Supply System Parameter Optimization for Soft Actuators*" Soft Robotics Journal (2020), doi: 10.1089/soro.2019.0134
- [J1] **Joshi, S.** and Paik, J. "*Multi-DoF Force Characterization of Soft Actuators*" IEEE Robotics and Automation Letters 4.4 (2019), 3679-3686. doi: 10.1109/LRA.2019.2927936
- Joshi S.**, Paik J. "*Sensorless estimation of force and displacement for soft pneumatic actuators*" IEEE Transactions in Mechatronics (2021), (Under review)

Peer-reviewed Conference Publications

- [C1] **Joshi, S.** and Gupta, A. "*Conceptual Design Of An Active Transtibial Prosthesis Based On Expected Joint And Muscle Forces In A Unilateral Transtibial Amputee: A Modelling Study*" ASME 2015 International Mechanical Engineering Congress & Exposition, Houston, TX, USA. doi:10.1115/IMECE2015-51576

Peer-reviewed Abstracts and Posters

- Joshi, S.**, Giraud, F. and Paik, J., Force Characterization Of Meso-Scale Haptic Devices, IEEE/RSJ International Conference on Intelligent Robots and Systems (IROS) 2019, Macao
- Joshi, S.** and Paik, J., Parametric study of Pneumatic Circuit Model for Powering and Controlling Soft Pneumatic Actuators, IEEE International Conference on Soft Robotics (RoboSoft), 2018, Livorno, Italy
- Sonar, H., **Joshi, S.**, Robertson, M., and Paik, J., Interactive soft pneumatic actuator skin, IEEE/RSJ International Conference on Intelligent Robots and Systems, Vancouver, BC, Canada, September 24-28, 2017 (**Best student poster**)
- Sonar, H., **Joshi, S.**, Robertson, M., and Paik, J., Interactive soft pneumatic actuator skin, WorldHaptics/EuroHaptics 2017, Munich, Germany

Research Interests and Keywords

Robotics, mechatronics, embedded systems, soft robotics, biomechanics, dynamics and controls, wearable devices, bio-inspired design, machine learning, applied neural networks

Skills

Engineering: Mechanical fabrication; PCB design and fabrication; mechatronics and embedded systems; soft actuator and sensors; wearable robots

Programming: MATLAB, C/C++, Python, Julia (beginner), Labview (beginner)

Design: SolidWorks, AutoCad, Catia, Inkscape, EagleCad

Simulation software: Simulink, OpenSim, Robot Operating System (beginner)

Other: Microsoft Office, LaTeX, Adobe Lightroom and PremierPro, OpenShot video editor

Extracurricular Activities

Music: Professionally trained in Hindustani Classical Music for vocals and sitar for over ten years; played and performed as part of bands for several events

Positions of responsibility: President of Institute Robotics Association (SPCE, 2011-13); Institute Music secretary (SPCE, 2011-12); Department Cultural Secretary (IIT Bombay, 2014-15); Institute Music convener (IIT Bombay, 2014-15); Cultural representative for Indian association (EPFL, 2018-20)

Volunteering: Participated in a two-day hackathon known as Hackahealth, and designed and fabricated a robotic arm and grasping assist device for a physically impaired subject.

Languages

English: Fluent

Marathi: Native

French: B1

Hindi: Bilingual